Hybrid plasmonic-photonic platform for quantum photonics

Xiao Yu

THESE DE DOCTORAT DE L'ETABLISSEMENT UNIVERSITE BOURGOGNE FRANCHE-COMTE PREPAREE AU LABORATOIRE INTERDISCIPLINAIRE CARNOT DE BOURGOGNE

Ecole doctorale n° 533 Carnot-Pasteur

Doctorat de Physique

Par
M. Xiao YU

Hybrid plasmonic-photonic platform for quantum photonics

Thèse présentée et soutenue à Dijon, le 22 mai 2023

Composition du Jury :

Agnès MAITRE	Professeur Sorbonne Université Laboratoire INSP, Paris	*Rapportrice*
Christophe COUTEAU	Maitre de conférence Université de technologie de Troyes, Laboratoire L2N, Troyes	*Rapporteur*
Stéphanie BUIL	Maitre de conférence Université de Versailles-Saint Quentin Paris	*Examinatrice*
Fadi BAIDA	Professeur Université de Franche-Comté, Laboratoire FEMTO-ST, Besançon	*Président*
Gérard COLAS des FRANCS	Professeur Université de Bourgogne Laboratoire ICB, Dijon	*Directeur de thèse*

Abstract

Keywords: optical antenna, photonic waveguide, quantum dots

Integrated quantum photonic circuits requires an efficient coupling of photon source to photonic waveguide. In this work, we established directional QD coupling to planar waveguide assisted by Yagi-Uda antenna. We build a theoretical model of single dipole coupled to TiO_2 waveguide to analyze different coupling modes and obtain the decay rate and coupling efficiency as a function of waveguide thickness. We start from the coupling of QD emission to Yagi-Uda antenna on glass substrate (without waveguide). We use numerical simulation to optimize the resonance and directivity of antenna design. We fabricate the antenna and develop a method to accurately deposit a few QDs close to the Yagi-Uda antenna. The optical characterization shows clear signal of directional scattering originating from antenna effect. We also investigate the lifetime and photon antibunching effect of the QD emission.

Finally we fully integrate QDs and antenna to TiO_2 planar waveguide. In the optical characterization, we observe QD emission coupled to a propagating TE mode of the planar waveguide and also leakage emission into the substrate via TM mode. The light scattering at the edge of the waveguide reveals directional coupling in the polarization parallel to the antenna axis, but we also observe parasitic emission in the perpendicular direction. We attribute the perpendicular emission to the misplacement of QD. In order to obtain better coupling, we need to improve the deposition method which will be done in our future work.

Resumé

Mots de clé: antenne optique, guide d'onde photonique, boîte quantiques

Les circuits photoniques quantiques intégrés requièrent un couplage efficace d'une source de photons au guide d'onde photonique. Dans ce travail, nous avons établi un couplage QD directionnel à un guide d'onde planaire assisté par une antenne Yagi-Uda. Nous partons du couplage de l'émission QD à l'antenne Yagi-Uda sur substrat de verre (sans guide). Nous réalisons des simulations numériques pour optimiser la résonance et la directivité de l'antenne. Nous fabriquons l'antenne et développons une méthode pour déposer avec précision quelques QDs à proximité de l'antenne Yagi-Uda. La caractérisation optique montre un signal clair de diffusion directionnelle provenant de l'effet d'antenne. Nous étudions également la durée de vie et l'effet anti-groupement de photons des QDs.

Enfin, nous intégrons les QDs et l'antenne au guide d'onde planaire TiO_2. Dans la caractérisation optique, nous observons principalement que l'émission des QDs se couple à un mode guidé TE mais aussi une émission dans le substrat via un mode à fuite TM. La diffusion de la lumière au bord du guide d'onde montre un couplage directionnel dans la polarisation parallèle à l'axe d'antenne, mais on observe également un couplage parasite dans la direction perpendiculaire. La raison la plus probable de ce modèle est le mauvais placement de QD. Afin d'obtenir un meilleur couplage, nous devons améliorer la méthode de dépôt qui sera effectuée dans nos travaux futurs.

Acknowledgment

My journey through my PhD work and manuscript writing was a combination of difficulties and assistance, moments of depression and inspiration, pain and encouragement. In light of this, I am truly grateful to all the individuals who supported me both in my research and personal life.

First and foremost, I would like to express my deepest appreciation to my supervisor, Prof. Gérard Colas des Francs, who provided unwavering guidance throughout my entire PhD thesis. His continuous mentorship has shaped me into a capable physics researcher. I am particularly grateful for his professionalism, patience, and meticulousness, which have greatly influenced my approach to scientific research.

I would also like to extend my gratitude to the members of my thesis committee. Their valuable time and efforts in reading my thesis and providing invaluable suggestions are highly appreciated. Their expertise and constructive comments have allowed me to recognize and address the shortcomings in my work.

A special mention goes to my collaborators Alexandre Bouhelier, Laurent Markey, and Jean-Claude Weeber, who helped me in nanofabrication and optical experiments. Their guidance and advice regarding the research and manuscript have been immensely valuable. I would also like to thank Juan, Francoise, and Aurora for their assistance in material preparation and laboratory work.

My journey would not have been possible without the companionship of my friends Konstantin, Florian, Astghik, Kaipeng, Junyang, Meiyun, Xiaohan, Alpha, Reinaldo, Xavier, and Deepak. Their unwavering support in both my work and personal life has been invaluable. I cherish the days we spent working, sharing joyous moments, and facing challenges together.

I am deeply indebted to my gratitude to my parents, who not only gave me life but also nurtured and guided me throughout. Their all-encompassing care and life advice transformed my character and give me confidence.

I would like to acknowledge the LIMQUET project for not only providing financial support for my research but also for creating a comprehensive platform for early-stage researchers like myself. This project has been instrumental in my academic journey.

Overview

The convergence of nanophotonics and quantum technology is based on efficient coupling between photon source and photonic circuits. In this thesis, we investigated the unidirectional coupling of QD emission to TiO_2 waveguide assisted by Yagi-Uda antenna. We built analytical formalism and numerical model to optimize the resonance of the Yagi-Uda antenna and the directivity of the coupling.

In Chapter I, we review advances in integrated quantum technologies, especially the development of integrated photonic circuits and integrated single photon emitters. Then we introduce the coupling between the integrated photon source and the integrated photonic/plasmonic waveguide and the development of optical Yagi-Uda antenna. All of these works above inspire our idea of combining integrated photon source and the unidirectional scattering of the Yagi-Uda antenna.

In Chapter II, we discuss the optical photon sources integrated on the photonic chip. We present dipolar emission coupling to a planar waveguide. This simple configuration permits a simple understanding of the coupling process and key parameters. This also constitutes a benchmark before considering antenna-mediated coupling configuration.

In Chapter III, we investigate nano-optical Yagi-Uda antenna excited by QD. We first present simple recipes to optimize the Yagi-Uda antenna in free space, taking benefit of the recent literature. We adapt this rule to glass supported Yagi-Uda antenna. Finally, we experimentally investigate QD coupling to the antenna.

The Yagi-Uda antenna and QD are deposited by E-beam lithography on the glass substrate. We developed a method to locally deposit QDs in a 100 nm hole. The unidirectional scattering of the Yagi-Uda antenna is observed by back focal plane microscopy. We also estimate Purcell factor of the Yagi-Uda antenna based on the lifetime measurement.

In Chapter IV, we integrate QD and Yagi-Uda antenna on TiO_2 waveguide. The numerical simulation shows the unidirectional coupling of QD emission. Optical characterization shows antenna mediated QD emission to TE guided mode in the planar waveguide. We observed the expected directional emission for TE polarized emission but also parasitic TM scattering in the orthogonal direction.

A summary and some perspective are addressed in final chapter.

Contents

Chapter 1

State-of-the-art

In the past decades, strong efforts have been put towards convergence of integrated photonics and quantum technologies[1, 2]. In recent years, quantum computing, quantum communication, quantum sensing, have been demonstrated in optical and atomic platforms. With the development in nano optics, photonics and plasmonics, researchers proceed to integrate quantum technologies to photonic platform[3, 1, 4]. Numerous demonstrations spans from on-chip indistinguishable photon source[5], microwave trapped on-chip qubit[6], integrated quantum key distribution(QKD)[7], CNOT gate[8], etc. Fig.1.1 shows a scheme of integrated photonic circuits with different components. From an experimental point of view, the development of integrated quantum photonics generally contains three parts, photon source, photonic and plasmonics circuits, detector.

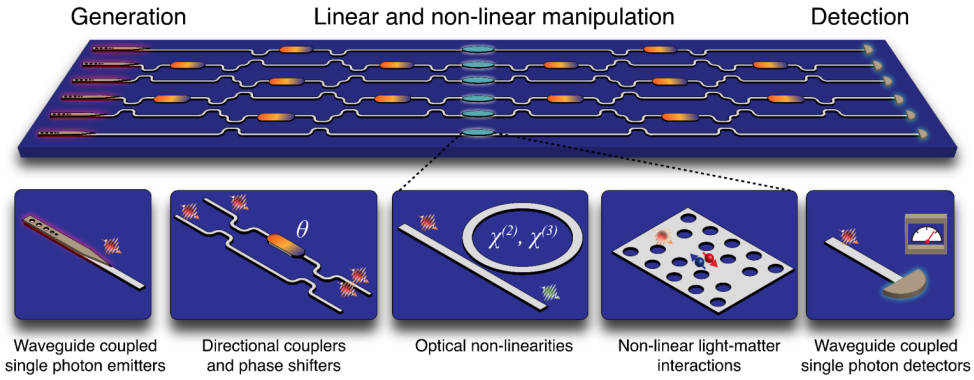

Figure 1.1: A sample scheme of complete integrated photonic circuits with different components. From[4] with permissions.

Light source is the primary requirement. Integrated photonics requires optical sources with high quantum efficiency, high brightness and high coupling effi-

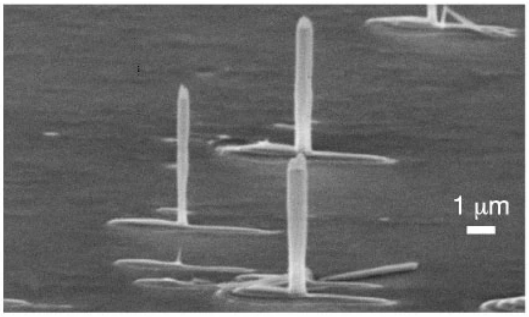

Figure 1.2: Integrated indistinguishable single photon source using QD embedded in Bragg mirror cavity[9].

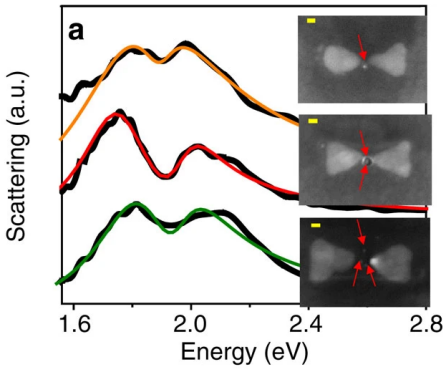

Figure 1.3: QD deposited in the gap of Bow-tie antenna. The strong local field in the gap induces Rabi splitting of QD emission[10].

ciency to the photonic circuit. For quantum photonic circuits, the requirements are stricter: the photon source need to have high indistinguishably and long coherence time. As far as applications are concerned, efficiency and brightness are technological breakthrough. The connection between integrated photonics and quantum technology emerges at the interface between photon source and photonic circuits with better photon source control and on-chip coupling.

The emission of a single photon emitter can be modified and engineered by nearby photonic and plasmonic structures, optical cavities, and external fields (see Fig. 1.2 and 1.3). It is widely known that the photon emitter decay rate can be enhanced by Purcell effect[11] so that the dephasing rate becomes negligible[12]. The Purcell factor F_P is proportional to Q/V where Q is the quality factor of the cavity, and V is the mode volume[13]. An ideal enhancement device should have high quality factor and/or small mode volume.

The high quality factor is achievable with optical microcavities whereas plasmonic antenna permits low mode volume of interest for integrated applications[14, 15, 10, 16, 17].

Furthermore, the photon emission can be spatially modified by photonic and plasmonic structures to squeeze light in desired direction. Optical antennas are promising candidates which provide enhanced decay rate and emission directivity at the same time[20, 21]. The decay rate can be enhanced by two orders of magnitude with an out-of-plane unidirectional light emission for molecule coupled to a nanoaperture[22, 23]. QD coupled to Yagi-Uda antenna presents enhanced decay rate and directional scattering[24].

Improving the coupling between local photon source and the nanooptical circuit can be achieved thanks to dielectric grating[25], photonic crystal waveguide[26],

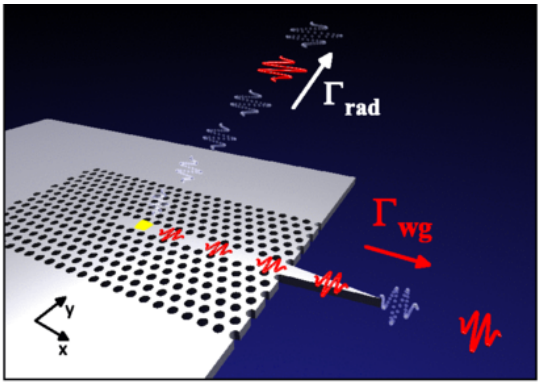

Figure 1.4: QD coupled to photonic crystal. The coupling efficiency is close to unity[18].

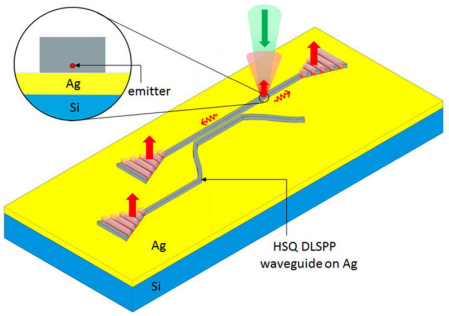

Figure 1.5: Nanodiamond single photon source integrated to plasmonic circuits. The quantum dot is fixed by PMMA[19].

nanoantenna[27, 28] or plasmonic waveguide[29, 30] (see Fig. 1.4 and 1.5). The coupling efficiency is remarkable especially on plasmonic nanowire gap waveguide. The unidirectional scattering on substrate has been studied on different types of antenna like Yagi-Uda[31, 24, 32], nano particle array[33]. The Yagi-Uda antenna draw most attentions since its high directivity and local enhancement property. The Yagi-Uda antenna is firstly introduced into nano optics as a unidirectional scatter in 2008[34]. The Yagi-Uda optical antenna excited by single dipole is firstly proposed theoretically by Taminiau et al.[31]. They investigated the unidirectional scattering of Yagi-Uda nano antenna supported on a glass substrate. Array of Yagi-Uda antennas fabricated on a photonic chip as a unidirectional photonic metamaterial[35] was also realized in the same year. Following the Yagi-Uda antenna design, the experimental implementation[24] is done in 2010 (see Fig. 1.6). The experiment shows the unidirectional scattering of QD coupled to Yagi-Uda antenna and the dependency between directivity and antenna dimensions. Different local photon source such as LH2 complex[36] and semiconductor nanowire[37] coupled to Yagi-Uda antenna were studied afterwards. These works prove the unidirectional scattering and plasmonic local enhancement by Yagi-Uda antenna.

The further step to apply Yagi-Uda antenna to photonic chip is experimentally implemented in 2012[32]. A Yagi-Uda antenna is fabricated on top of a Si_3N_4 strip waveguide (see Fig. 1.7). The laser light is coupled into waveguide through tapered optical fiber. The authors demonstrate unidirectional out coupling thanks to nano antenna. However, when considering the reciprocal situation, antenna mediated waveguide excitation, they did not observe unidirectional in-coupling. The reason is that Yagi-Uda antenna is designed for local excitation. When all antenna elements are excited, the interference conditions are broken. The Yagi-Uda optical antenna is a subwavelength device. The period of antenna elements

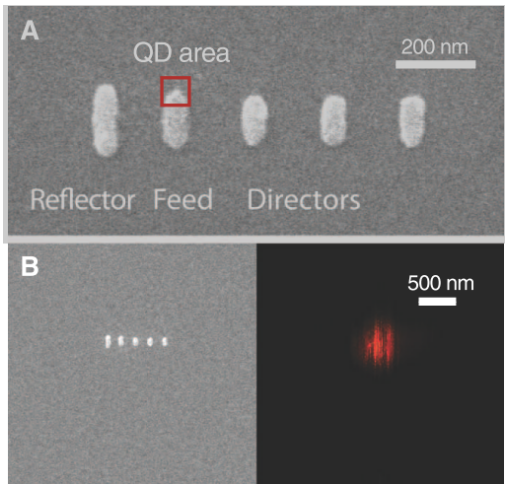

Figure 1.6: single QD coupled to Yagi-Uda antenna showing unidirectional scattering. a) QD deposited close to Yagi-Uda nanoantenna. [24].

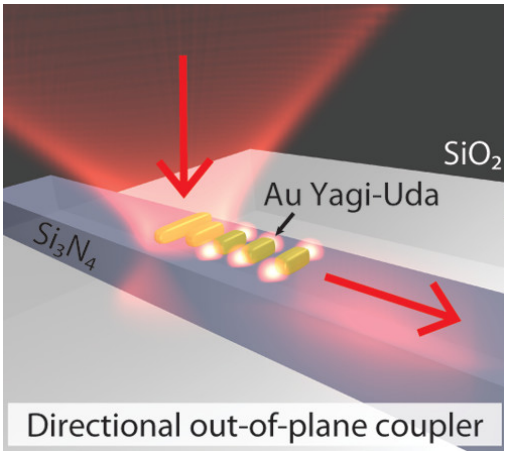

Figure 1.7: Laser light coupling of Si_3N_4 waveguide using plasmonic Yagi-Uda optical antenna[32]. The unidirectional out coupling is observed in the Fourier plane image.

is smaller than the diffraction limit. It is not possible to selectively excite one element by focused laser light.

While the single photon emitter coupling to Yagi-Uda antenna on glass is proved functional and efficient and antenna-photonic chip waveguide efficient coupling was demonstrated, we plan to explore the design and experimental realization of QD emission coupling to waveguide assisted by Yagi-Uda antenna. Our design is shown in Fig. 1.8. The circular planar waveguide is deposited on the glass substrate. The Yagi-Uda nano antenna are fabricated on the TiO_2 waveguide and a few colloidal QDs are deposited close to the feed element of the nano antenna. When QDs are excited by laser beam, the QD fluorescence emission is directionally coupled to TiO_2 waveguide through Yagi-Uda nano antenna. The circular TiO_2 waveguide can display the scattering pattern of Yagi-Uda antenna at the edge.

We plan to implement the device step by step and improve the coupling quality until it can be used in the functional photonic device.

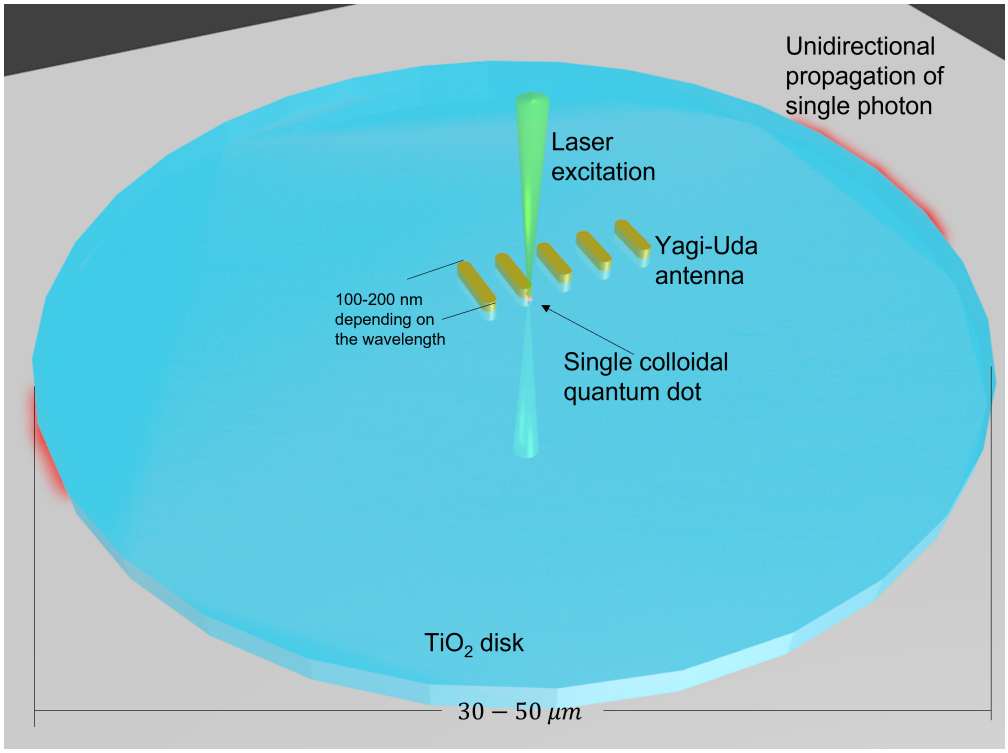

Figure 1.8: Experimental design of QD coupling to TiO_2 planar waveguide assisted by Yagi-Uda optical antenna. The Yagi-Uda antenna is set in the center of TiO_2 waveguide. QD is deposited close to the feed element of Yagi-Uda optical antenna.

Chapter 2

Optical nanosources integrated on photonic chip

Introduction

We present the main features of dielectric waveguides and key parameters governing the coupling between a quantum emitter and a guided mode. We notably introduce the concept of density of guided modes that reveals physical origins of the different relaxation channels for coupled emission into the waveguide.

2.1 Guided modes in planar TiO_2 waveguides

Without going into details, we recall some important properties of planar dielectric waveguides, insisting on some important concepts useful for describing the dipolar emission into a guided mode. In an ideal cavity, the electromagnetic fields have to cancel at the wall mirror (perfect conductors). This leads to a minimal size for guiding light. In order to overcome this limitation, one can consider total internal reflection on dielectric instead of perfect conductor. Light can be guided thanks to reflection (above the critical angle) and the electromagnetic fields no more need to cancel at the interfaces. Then one could expect to realize a waveguide with a thickness smaller than $\lambda/2$. We will see that the mode extension is however still limited by the diffraction limit.

As an example, let us consider a dielectric slab (optical index $n_2 > n_1, n_3$) sandwiched in between 2 dielectric media (superstrate of optical index n_1 and substrate n_3), such as TiO_2 planar waveguide deposited on a glass substrate that we will investigate in the following chapters. The 2D model setup is shown in Fig. 2.1.

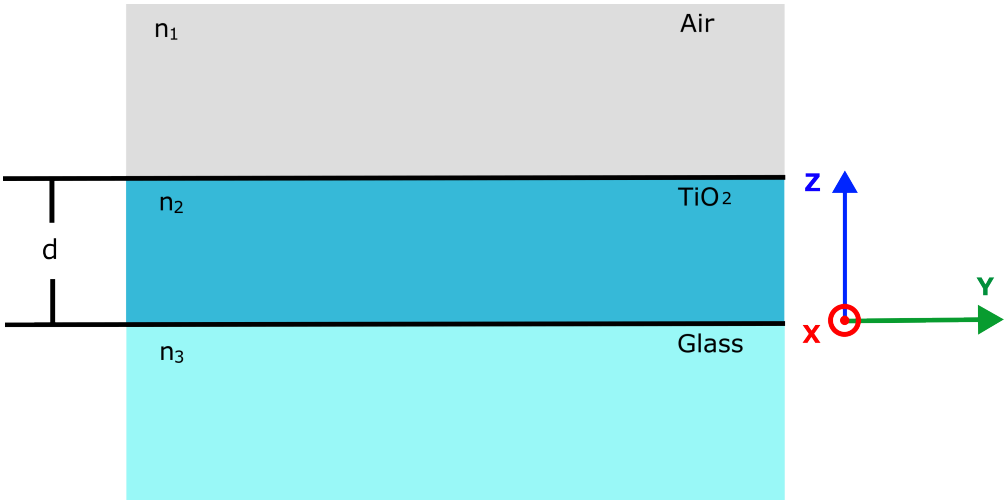

Figure 2.1: 2D model scheme of guided mode analysis. The electric field propagates along y axis and is polarized along x axis.

2.1.1 Dispersion relation

We want to establish the conditions to support a guided mode (the so-called dispersion relation), as well as the profile of these guided modes. The general method consists in writing the expression of the electromagnetic field in each medium and determining their conditions of existence using the boundary conditions.

Field expression

We consider a wave TE-polarised (polarisation TM is analogously considered working on the magnetic field instead of the electric field). Assuming a polarization along the x-axis and propagation along y, the electric field expresses

$$\mathbf{E}(\mathbf{r}) \quad = \quad E(z)e^{i(\beta y-\omega t)}\mathbf{e}_x \tag{2.1}$$

The wave equation writes

$$\Delta\mathbf{E}_i - \frac{\epsilon_i}{c^2}\frac{\partial^2\mathbf{E}_i}{\partial t^2} = \mathbf{0} \text{ (i=1,2,3)} \tag{2.2}$$

So that

$$\frac{\partial^2 E(z)}{\partial z^2} = [\beta^2 - \epsilon_i\frac{\omega^2}{c^2}]E(z) \tag{2.3}$$

Before going further, it is useful to bound the range of the propagation constant β to ensure total internal reflection in the dielectric slab ($n_3k_0 \leq \beta$) and to support

a guided wave ($\beta \leq n_2 k_0$), hence $n_3 k_0 \leq \beta \leq n_2 k_0$. Then $\beta^2 - \epsilon_{1,3}\omega^2/c^2 \geq 0$ and $\beta^2 - \epsilon_2\omega^2/c^2 \leq 0$. We deduce the solutions of the previous differential equation

$$\begin{aligned} E(z) &= Ae^{-\gamma_1 z} \text{ with } \gamma_1 = \sqrt{\beta^2 - \epsilon_1 \frac{\omega^2}{c^2}}\ , z > 0 \\ E(z) &= C\cos(k_z z) + D\sin(k_z z)\ , k_z = \sqrt{\epsilon_2 \frac{\omega^2}{c^2} - \beta^2}\ , -d \leq z \leq 0 \\ E(z) &= Be^{\gamma_3 z} \text{ with } \gamma_3 = \sqrt{\beta^2 - \epsilon_3 \frac{\omega^2}{c^2}}\ , z < -d \end{aligned} \tag{2.4}$$

Boundary conditions

The tangential component of the electric field is continuous across the interface

$$\begin{aligned} A &= C \text{ (at z=0)} \\ Be^{-\gamma_3 d} &= C\cos(k_z d) - D\sin(k_z d) \text{ (at z=-d)} \end{aligned} \tag{2.5}$$

Another boundary conditions involves the magnetic field. The magnetic field expresses from the electric field thanks to Maxwell's equation

$$\begin{aligned} \nabla \wedge \mathbf{E} = -\frac{\partial \mathbf{B}}{\partial t} \quad \text{hence} \\ -\frac{\partial E(z)}{\partial z} e^{i(\beta y - \omega t)} &= i\omega B_x \\ 0 &= i\omega B_y \\ i\beta E(z) e^{i(\beta y - \omega t)} &= i\omega B_z \end{aligned} \tag{2.6}$$

In case of non magnetic medium, the tangential and normal component of $\mathbf{B}$ are continues. In particular, the continuity of B_x leads to the continuity of $\partial E(z)/\partial z$. It comes therefore

$$\begin{aligned} -\gamma_1 A &= k_z D \text{ (at z=0)} \\ \gamma_3 B e^{-\gamma_3 d} &= k_z C\sin(k_z d) + k_z D\cos(k_z d) \text{ (at z=-d)} \end{aligned} \tag{2.7}$$

One finally gathers the conditions (2.5) and (2.7) to achieve [38]

$$\boxed{\tan(k_z d) = \frac{k_z(\gamma_1 + \gamma_3)}{k_z^2 - \gamma_1\gamma_3}}$$

In addition with $\gamma_{1,3} = \sqrt{\beta^2 - \epsilon_{1,3}\frac{\omega^2}{c^2}}$ and $k_z = \sqrt{\epsilon_2 \frac{\omega^2}{c^2} - \beta^2}$, this relation implicitly defines the dispersion relation $\beta = f(\omega)$ that is numerically solved. We

define the effective index of a guided mode as $n_{eff} = \beta/k_0$. A guided mode in an dielectric slab obeys $n_1 < n_{eff} < n_3$. Effective index is therefore a usefull parameter to characterize the guided mode. It is shown at $\lambda = 670$ nm for a TiO_2 in Fig. 2.2a). We observe a cut-off for each guided mode, corresponding to $n_{eff} \to n_3$. Note that the dispersion relation also admits (complex) solutions for lower thickness but this corresponds to mode leaking into the substrate ($n_{eff} < n_3$) limiting the propagation length so that it is defined as the cut-off condition.

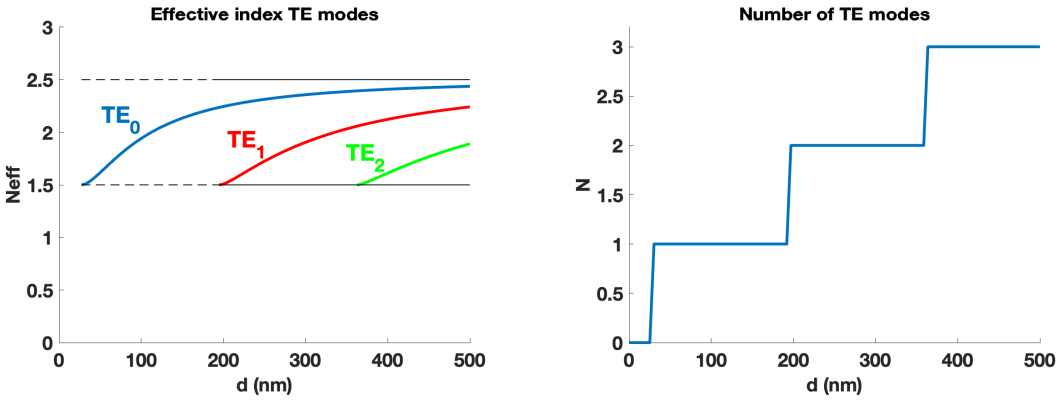

Figure 2.2: a) Dispersion relation of the guided modes TE_m in a TiO_2 planar waveguide as a function of the thickness. b) Number of modes as a function of thickness. $n_1 = 1$ (air), $n_2 = 2.56$ (TiO_2) and $n_3 = 1.50$ (glass). $\lambda = 670$ nm.

Dispersion relation is oftently written with reduced parameters for generality purpose [39]. It comes (m=0,1..., is the mode number)

$$\begin{aligned}
&\sqrt{1-b}V = m\pi + \tan^{-1}\left(\sqrt{\frac{b}{1-b}}\right) + \tan^{-1}\left(\sqrt{\frac{b+a}{1-b}}\right) \\
&V = k_0 d(n_2^2 - n_3^2)^{1/2} \text{ (normalized frequency)} \\
&a = \frac{n_3^2 - n_1^2}{n_2^2 - n_3^2} \text{ (asymmetry measure)} \\
&b = \frac{n_{eff}^2 - n_3^2}{n_2^2 - n_3^2} \text{ (normalized guide index)}
\end{aligned} \tag{2.8}$$

the cutt-off condition ($n_{eff} = n_3$) corresponds to $b = 0$ so that the cutt-off occurs for $V_m = \tan^{-1}\sqrt{a} + m\pi$. This leads to the thickness cut-off $d_0 = 27$ nm, $d_1 = 195$ nm and $d_2 = 362$ nm, for TE mode as observed in Fig. 2.2. Similarly, TM mode cut-off is around 100 nm. We observe that the planar waveguide supports a single mode for thickness 27 $nm < d_\lambda <$100 nm.

The number N of TE modes supported for a given normalized frequency V (or thickness d such that $V = k_0 d(n_2^2 - n_3^2)^{1/2}$) is such that $V < V_N = \tan^{-1}\sqrt{a} + N\pi$ so

that we can determine the number of modes $N = [(1/\pi)(V - \tan^{-1}\sqrt{a}]_{int}$ where $[...]_{int}$ refers to the integer just above the number in brackets. The number of modes is presented in Fig. 2.2b). We will discuss in Sec.2.1.3 the density of guided mode that is a key parameter to describe the coupling with a nearby emitter.

2.1.2 Mode profile and confinement

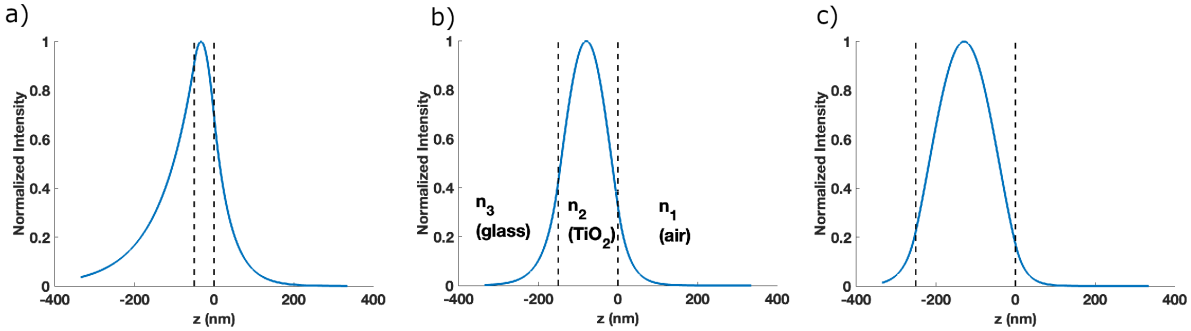

Figure 2.3: Mode profile for 3 slab thicknesses. a) $d = 50$ nm (left), b) $d = 150$, c) $d = 250$ nm. The vertical dashed lines indicate the TiO_2 slab.

Fig. 2.3 presents the fundamental mode profile modal (TE_0), deduced from Eq. 2.4. For thick slab, the field is mainly confined into the slab. However, the thinner the slab is, the more the field extends into the substrate and superstrate.

A simple criterium to characterize the mode extension consists in the mode width. It is the distance onto which the electric field amplitude decays of $1/e$. It is presented in Fig. 2.4. For thick waveguide, the mode extension is roughly one wavelength. Differently, for thin slab, the mode largely spreads out of the waveguide. To understand this behavior, let us consider the effective index for thin slab (Fig. 2.4). It is comprised between the optical indices of the external media and the slab core. For thin slab, the effective index tends towards the optical index of the substrate. The mode extension in the substrate is given by $\delta = 1/\gamma_3 = 1/\sqrt{\beta^2 - \epsilon_3\frac{\omega^2}{c^2}} \underset{d\to d_0}{\to} \infty$ since $\beta \underset{d\to d_0}{\to} \epsilon_3\frac{\omega^2}{c^2}$ recalling that $(n_{eff} \underset{d\to d_0}{\to} n_3)$ and mode extension diverges as well. Finally, we observe that the minimal mode extension is roughly λ/n_2, for a slab thickness of about $\lambda/2n_2$. Therefore high index material will be preferred to achieve high mode confinement. However, the control of the light propagation will be possible only for sizes above the diffraction limit.

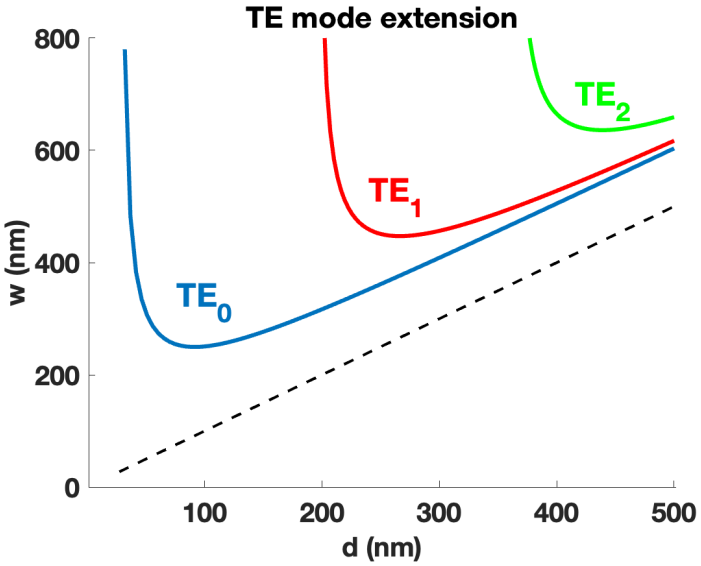

Figure 2.4: TE modes extension as a function of the slab thickness. The oblique line refers to a mode confinement equal to the thickness of the film.

2.1.3 Density of guided modes (system 1D)

Let us consider a guided mode propagating in the (x,y) plane with a propagation constant β. We look for the number of modes in the range $[k_{\|}; k_{\|} + dk_{\|}]$ in the reciprocal space (k_x, k_y). We follow a derivation similar to the Planck's derivation of the energy density of blackbody radiation. Let us consider a square of length L (arbitrary length, intermediate of calculus) in the direct plane.

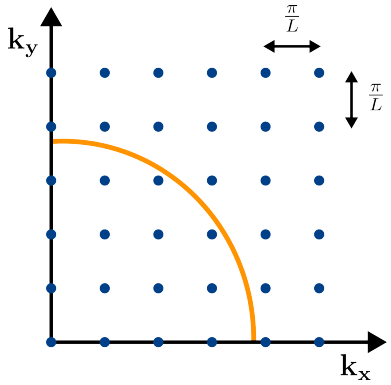

Figure 2.5: The supported modes constricted by the boundary conditions.

The boundaries conditions lead to

$$k_x = n_x \frac{\pi}{L} \, , k_y = n_y \frac{\pi}{L} \quad (n_x, n_y = 1, 2, 3, ...). \tag{2.9}$$

Hence

$$\Delta k_x = \Delta k_y = \frac{\pi}{L}. \tag{2.10}$$

In the $k_\parallel$-space, a mode occupies the surface $S_k = (\pi/L)^2$. The number of modes in the range $[k_\parallel; k_\parallel + dk_\parallel]$ (i.e. in 1/4 disk area $dS_k = 2\pi k_\parallel dk_\parallel$)

$$dN = \frac{dS_k/4}{S_k} = \frac{L^2}{2\pi} k_\parallel dk_\parallel. \tag{2.11}$$

The number of modes per unit area (in reciprocal space) is therefore

$$N(k_\parallel)dk_\parallel = \frac{dN}{L^2} = \frac{k_\parallel}{2\pi} dk_\parallel. \tag{2.12}$$

Finally, we use the dispersion relation that characterizes the guided modes

$$k_\parallel = n_{eff}\frac{\omega}{c}, \tag{2.13}$$

$$N(k_\parallel) = \frac{\omega}{2\pi v_\varphi}, \tag{2.14}$$

where $v_\varphi = c/n_{eff}$ is the phase velocity of the guided mode. Then

$$N(\omega) = N(k_\parallel)\frac{dk_\parallel}{d\omega} \tag{2.15}$$

$$= \frac{\omega}{2\pi}\frac{1}{v_\varphi v_g}, \tag{2.16}$$

where $v_g = \frac{d\omega}{dk_\parallel}$ is the group velocity of the guided mode.

The density of states obeys $N(\omega) \propto 1/\partial\omega/\partial k$ so that it diverges close to the cut-off(photonic analog of electronic van Hove singularities).

2.2 Dipolar emitter and relaxation channels

2.2.1 Fermi's golden rule and local density of states

The spontaneous emission at the angular frequency ω_0 from the excited state $|e\rangle$ to the ground state $|g\rangle$ of an excited atom presents a decay rate that follows Fermi's golden rule

$$\Gamma(\mathbf{r}) = \frac{2\pi}{\hbar^2}|\langle g|\hat{\mathbf{p}}\cdot\hat{\mathbf{E}}(\mathbf{r})|e\rangle|^2\delta(\omega-\omega_0). \tag{2.17}$$

The operators $\hat{\mathbf{p}}$ and $\hat{\mathbf{E}}$ refer to the atomic transition dipole moment and the electric field, respectively. In the following, we are interested in the effect of the

cavity on the spontaneous emission rate. In the case of a lossy system, the Dirac distribution in (2.17) is replaced by the density of modes per unit angular frequency $\delta(\omega - \omega_0) \rightarrow N(\omega)$. Moreover, the interaction Hamiltonian $-\hat{\mathbf{p}} \cdot \hat{\mathbf{E}}(\mathbf{r})$ reveals that the coupling between the excited atom and its environment depends on the position. In particular, efficient coupling occurs at the anti node of a mode. In particular a quantum emitter couples to a guided mode if it is located at the maximum of the electric field profile (center of the waveguide for the TE_0 guided mode, see Fig. 2.3). This leads to introduce the local density of states (LDOS) that includes the mode profile and the density of modes. The electric-field operator associated to mode writes [40]

$$\hat{\mathbf{E}}(\mathbf{r}) = i\sqrt{\frac{\hbar\omega}{2\varepsilon_0\varepsilon_1 V}}\mathbf{f}(\mathbf{r})\hat{a} + h.c. \tag{2.18}$$

where V is the quantization volume, $\epsilon_1 = n_1^2$ is the dielectric constant $\hat{a}$ is the boson operator and $\mathbf{f}(\mathbf{r})$ describes the spatial variations of the mode into the cavity [$|\mathbf{f}(\mathbf{r})| = 0$ at a node and $|\mathbf{f}(\mathbf{r})| = 1$ at an antinode]. To achieve this expression, the classical electric field is expressed

$$\mathbf{E}(\mathbf{r}, t) = i\sqrt{\frac{\hbar\omega}{2\varepsilon_0\varepsilon_1 V}}\mathbf{f}(\mathbf{r})e^{-i\omega t} + c.c \tag{2.19}$$

and is normalized with respect to the energy($\langle ... \rangle$ refers to time-average quantities)

$$\begin{aligned} \hbar\omega &= \frac{1}{2}\int [\varepsilon_0\varepsilon(\mathbf{r}) \langle \mathbf{E}^2(\mathbf{r}, t)\rangle + \mu_0 \langle \mathbf{H}^2(\mathbf{r}, t)\rangle] d\mathbf{r} & (2.20) \\ &= \frac{\hbar\omega}{\varepsilon_1 V}\int \varepsilon(\mathbf{r})|\mathbf{f}(\mathbf{r})|^2 d\mathbf{r} & (2.21) \end{aligned}$$

where we assumed a non dispersive medium (with equipartition of electric and magnetic energy). Finally, the mode volume obeys

$$V = \frac{1}{\varepsilon_1}\int \varepsilon(\mathbf{r})|\mathbf{f}(\mathbf{r})|^2 d\mathbf{r}\,. \tag{2.22}$$

In presence of a lossy and dispersive medium, the modification of the decay rate can be described either within classical Lorentz model of an oscillating dipole [41] or within the full quantum description [42]. In both cases, this leads to the following expression for the rate modification

$$\frac{\Gamma_u(\mathbf{r})}{n_1\Gamma_0} = \frac{6\pi}{n_1 k_0} Im[G_{uu}(\mathbf{r}, \mathbf{r}, \omega_{em})], \tag{2.23}$$

where $\mathbf{G}$ is the Green's tensor associated to the emitter surroundings and G_{uu} refers to its diagonal components along the dipolar direction $\mathbf{u}$. This expression

quantifies the modification of the decay rate in a complex surroundings and will be our starting point to determine the effect of planar waveguide on the fluorescence decay rate. The expression (2.23) is a generalization of the Fermi's golden rule to dispersive and lossy surroundings. It is well-known from scattering formalism that the partial local density of states (P-LDOS) is related to the Green's dyad [43]

$$\rho_u(\mathbf{r}, \omega_{em}) = \frac{k_0^2}{\pi\omega} Im[G_{uu}(\mathbf{r}, \mathbf{r}, \omega_{em})] \tag{2.24}$$

so that Eq. (2.23) and (2.17) are fully equivalent in a non-absorbing medium. The P-LDOS also writes from cQED considerations

$$\rho_u(\mathbf{r}, \omega) = \frac{f_u(\mathbf{r})}{2\epsilon_1 V} N(\omega). \tag{2.25}$$

Therefore, the P-LDOS grasps the spatial dependency of the coupling to the cavity mode by $f_u(\mathbf{r})$ and the density of available modes for light emission $\rho(\omega) = N(\omega)/V$, per unit angular frequency and unit volume. The decay rate of a dipole emitter in the vicinity of a waveguide is governed by the density of guided modes. In particular, it is strongly enhanced close to the cut-off (See Eq.2.16).

2.2.2 Decay rate near a planar waveguide

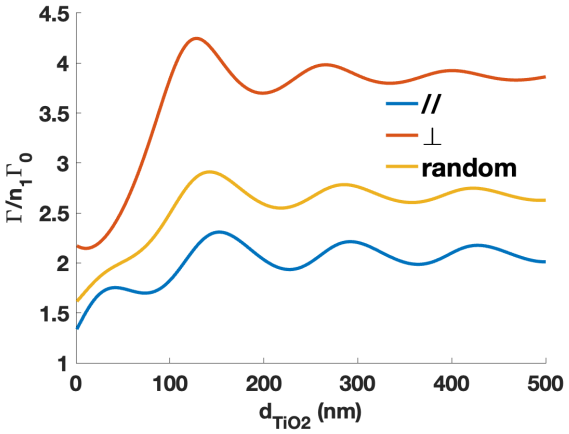

Figure 2.6: Decay rate as a function of the waveguide thickness. The dipolar emitter is in-plane(∥, along x), out-of plane(⊥, along z) or randomly oriented. The dipolar emitter is 7.5 nm above the waveguide (corresponding to the center of *e.g.* a 15 nm QD or NV nanodiamond).

Fig. 2.6 presents the dipolar total decay rate as a function of the slab thickness [44]. For a in-plane dipole, we observe an increase of the decay rate near the TE mode cut-off since it opens new relaxation channels. Similar features is observed for out-of plane dipole that preferentially couples to TM modes. Random orientation is obtained as the average $(2G_{\parallel} + G_{\perp})/3$ and follows similar behavior.

Relaxation channels

The various contributions to the total decay rate are determined from the Sommerfeld expansion of the dipolar emission [45, 44]. Indeed, it is possible to expand the Green's dyad over the wavenumber $k_{\parallel}$ so that the total decay rate (Eq. 2.23) obeys

$$\frac{\Gamma_u(d)}{n_1\Gamma_0} = \int_0^{\infty} \mathcal{P}(k_{\parallel})dk_{\parallel} \text{ , with} \tag{2.26}$$

$$\mathcal{P}(k_{\parallel}) = \frac{P(k_{\parallel})}{n_1 P_0}. \tag{2.27}$$

$P_0 = \omega_0^4|p|^2/12\pi\epsilon_0 c^3$ is the power radiated by the oscillating dipole in vacuum. $P(k_{\parallel})$ is the dipolar emission power spectrum (in the $k_{\parallel}$-space). The different

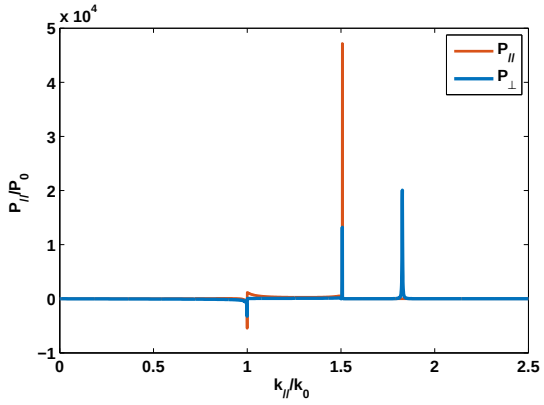

Figure 2.7: Dipolar emission as a function of the wavector parallel to the surface. The thickness is $d = 80$ nm. Losses have been added to avoid singularities at the guided mode effectives indices ($\epsilon_2 = n^2 = 2.375^2 + i1.100^{-2}$). Free-space contribution is not included so that negative values corresponds to emission lower than in free-space.

relaxations channels can be inferred from the dipolar emission power spectrum represented on Fig. 2.7. For in-plane dipole, we observe strong emission peaks at $k_{//}/k_0 = 1.51$ and 1.83 correspondings to TM_0 and TE_0 modes, respectively (see also Fig. 2.2). Out-of plane dipole couples to TM mode only.

2.2.3 Coupling efficiency

The Sommerfeld expression (see Fig. 2.7) also reveals the mode contribution to the total decay rate. We can therefore estimate the coupling efficiency, so called β factor, to a guided mode:

$$\beta_{TE} = \frac{\int_{TE} P(k_\parallel) k_\parallel}{\int_0^\infty P(k_\parallel) k_\parallel}, \tag{2.28}$$

and similar expression for TM mode channel.

Fig. 2.8 represents the coupling efficiency on out of plane dipole as a function of the distance to the planar TiO_2 waveguide. We observe up to 55% coupling efficiency in TE mode for a in-plane dipole. Half of the coupled power (so 27.5% of the emission) will propagate to the right and half the the left of the waveguide. It drops to 25% (12% left and right) in case of random orientation(not shown).

2.2.4 Conclusion

We have numerically investigated direct coupling efficiency of QD to a TiO_2 planar waveguide. We obtain 55% coupling efficiency but not directional. We will explore Yagi-Uda mediated and increase the directional propagation for on chip applications.

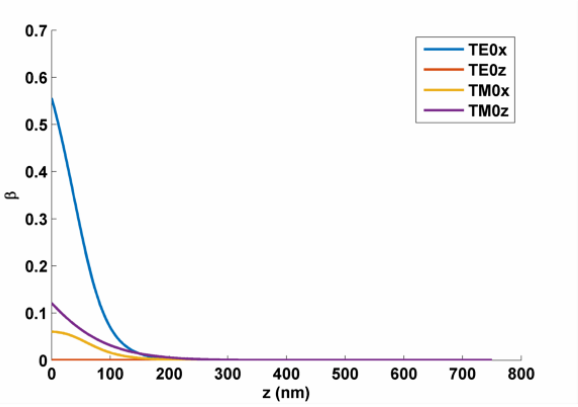

Figure 2.8: Coupling efficiency of different modes as a function of the thickness of TiO_2 waveguide.

Chapter 3

Integrated Yagi-Uda nano-antenna

3.1 Introduction

In this chapter, we present rules for designing Yagi-Uda nano optical antenna load by quantum dots emitters. Both analytical and full numerical simulation approaches are considered. Finally Yagi-Uda nano antenna supported on glass are fabricated and experimentally characterized.

Yagi-Uda antenna is the core component of our design. Looking into the plasmonic Yagi-Uda nano antenna(see Fig. 3.1), 5 gold nanorods are aligned. The antenna has 3 functional parts: reflector, feed and directors. Feed element is resonant to the excitation light of a nearby QD. The resonant wavelength of reflector and directors are red and blue shifted so that their interaction with resonant light results in a phase difference. The resulting interferences enhance light scattering along one direction of the antenna and suppress light in the opposite direction.

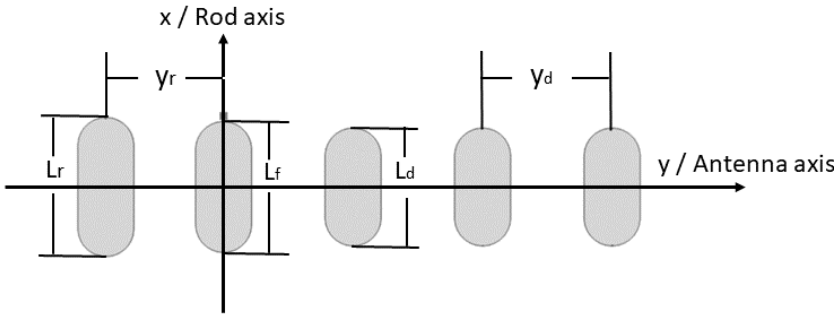

Figure 3.1: Scheme of Yagi-Uda antenna.

3.2 Design of Yagi-Uda antenna

3.2.1 Design rules

The design rule of Yagi-Uda antenna have been extensively studied in the radio frequency range[46, 47] and scale law approach have been proposed for down-scaling to nano-optics[34, 48, 49]. The dimensions (length) of the antenna elements (feed, directors and reflector) govern the antenna resonance whereas their spacing govern the antenna directivity. Rough dimensions of Yagi-Uda antenna are firstly estimated by semi-analytical method, which can save simulation time. The design is then simulated and optimized by finite element method (FEM).

Antenna resonance

The antenna resonance should be close to the QD emission wavelength, $\lambda_0 = 670$ nm.

The feed is the main element interacting with QD emitters. The feed length L is such that it is resonant at the working wavelength. According to antenna theory, the feed length should be half effective wavelength to support a dipole resonance.

The rod resonance can be determined as following. The effective wavelength λ_{spp} of the SPP supported by an infinite Au rod is first determined. Then Fabry-Perot like resonances for finite rod length L corresponds to

$$L + 2\delta = m\lambda_{spp} = m\frac{\lambda_0}{2n_{spp}} \quad m \in \mathbb{N}^+, \tag{3.1}$$

where δ refers to the field penetration depth into air[50].

Finally[34],

$$L = m\frac{\lambda_0}{2n_{spp}} - 2\delta,$$
$$\text{for } m = 1 \;\; L \approx \frac{\lambda_0}{2n_{spp}} - 2R. \tag{3.2}$$

where n_{spp} is the effective index of the surface plasmon polariton (SPP) supported by the nanorod. R is the radius of the nanorod. In Eq. 3.2, the substraction 2R is an approximation considering the reactance of the end of nano-rod.

The nanowire has a radius $R = 20$ nm. Gold dielectric constant is taken from experimental tabulated data[51]. We obtain $n_{spp} = 1.98$ at $\lambda = 670$ nm (see Fig. 3.2). The theoretical resonant length of nano-rod is $L = 129$ nm. This analysis gives a rough estimation of the resonant feed length that can be refined thanks to full numerical simulations (see Sec. 3.2.2).

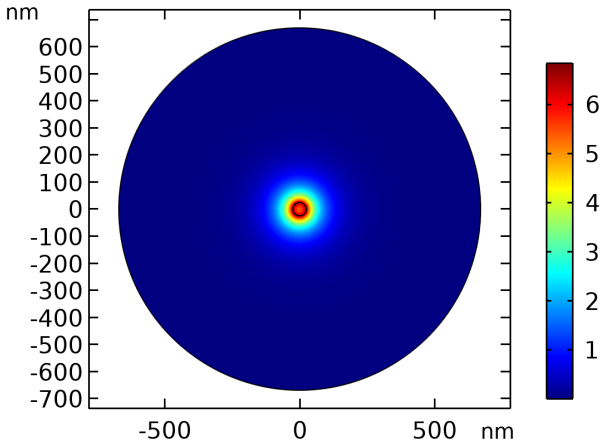

Figure 3.2: Electric field mode profile $|E|^2$ of the SPP supported by a gold nanowire. $R = 20$ nm, $\lambda = 670$ nm.

The length of reflector (L_r) and director (L_d) are determined as[31, 49]

$$L_r = 1.25L_f = 161nm, \tag{3.3}$$
$$L_d = 0.9L_f = 116nm. \tag{3.4}$$

Antenna Directivity

For a directivity along the antenna axis (diffracted wavevector $\vec{k} = k_0\vec{u_y}$), spacings of feed to reflector and feed to directors are:

$$y_r = \lambda_0/4.4 = 152nm, \tag{3.5}$$
$$y_d = \lambda_0/4 = 168nm, \tag{3.6}$$

where $\lambda_0 = 670$ nm is the QD emission wavelength in vacuum. y_d is the distance between feed and directors as well as the period between directors, y_r is the distance between feed and reflector.

3.2.2 Optimization of the antenna design

The design of the Yagi-Uda antenna with dipole source contains two optimization targets. First of all, the antenna needs to be resonant at the emission wavelength. Then the scattering of the antenna needs to be unidirectional. We define some parameters of interest for the optimization.

Absorption Power

The absorption of the nanorod $\langle P_{absorption}(\omega)\rangle$ is the time averaged power absorbed by the Yagi-Uda antenna[41].

$$\langle \boldsymbol{P}_{absorption}(\omega)\rangle = -\frac{1}{2}\int_V Re\{\boldsymbol{j}^*(\boldsymbol{r})\cdot\boldsymbol{E}(\boldsymbol{r})\}d\boldsymbol{r}, \tag{3.7}$$

where $\boldsymbol{j}$ is the current density, $\boldsymbol{E}$ is the electric field.

The absorption power reflects the resonance strength of the antenna excited by the QD dipolar emitter.

Gain and directivity

Yagi-Uda antenna modifies the dipole emission to unidirectional scattering. In order to measure the ability of unidirectional scattering, we introduce gain in antenna theory. For conventional antenna, gain is defined as[52]

$$G = \frac{P_{max}4\pi}{P_{rad}}, \tag{3.8}$$

$$P_{max} = max\{p(\theta,\phi)\}, \tag{3.9}$$

where P_{rad} is the radiation power in full space, P_{max} is the maximum power density. $p(\theta,\phi)$ is the angular power density of the radiated power. For dipolar emitter in free space, G=1.6.

Power front-to-back ratio

A simple directional measurement giving the power scattered in one direction is F/B power ratio to determine whether the scattering is unidirectional or bidirectional. $F/B = P_{front}/P_{back}$, where P_{front} and P_{back} refer to scattering along directors and reflector direction respectively (see Fig. 3.3).

In practice, the front and back power are substituted by far field power.

$$F/B = \frac{\int_{S_{front}} P(\theta,\phi)ds}{\int_{S_{back}} P(\theta,\phi)ds} = \frac{P_{front}}{P_{back}}, \tag{3.10}$$

According to the definition of Poynting's vector $\mathbf{\Pi}$. The power of far field can be calculated by

$$\mathbf{P}(\theta,\phi) = \mathbf{r}_0\cdot\mathbf{\Pi}(\theta,\phi) = \mathbf{r}_0\cdot Re(\mathbf{E}_{far}\times\mathbf{H}^*_{far}) \propto |\mathbf{E}_{far}|^2, \tag{3.11}$$

where r_0 is a unitary vector along the direction (θ,ϕ), E_{far} is the amplitude of the far-field asymptotic approximation for the electric field defined such that $E(\vec{r}) \sim \frac{E_{far}}{r}$ when $r \gg \lambda$.

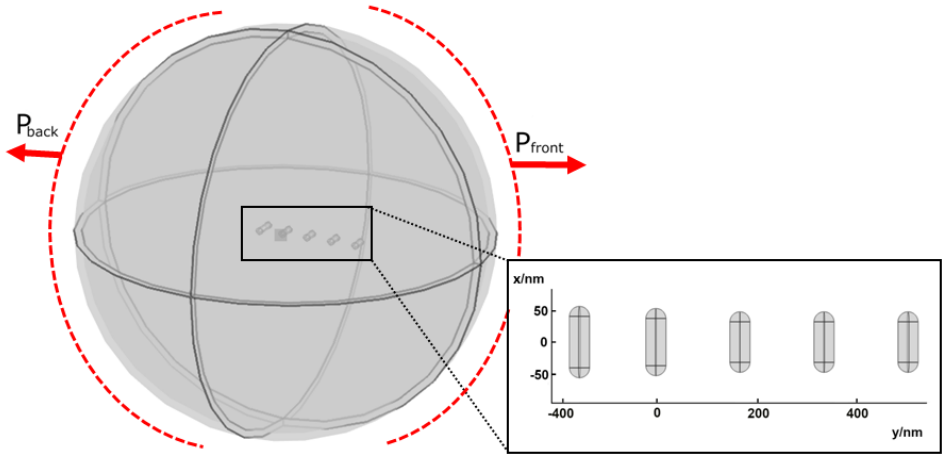

Figure 3.3: Model of simulation domain in free space. Red arrows represent integration surface of far-field power.

3.2.3 Finite element method

In practical work, it is difficult to obtain analytical solutions of light propagation in asymmetric model and inhomogeneous medium. The finite element method is a well-developed technique to solve complex boundary value problems[53]. We introduce the method and main technical details in this section.

Model

The simulation is based on 3D finite element method using COMSOL Multiphysics®[54]. The initial model is built according to analytic design rule described in Sec.3.2.1. Antenna elements are modeled by cylinders with two half spheres merged at both ends. Quantum dot is modeled as a single oscillatory dipole fixed at 5 nm from the end of the feed rod. The dipole moment is parallel to the long axis of the feed rod.

Discretization

In order to make the wave equation numerically solved, the model is discretized into small elements. Normally the surface and volume of model are divided into triangle elements (on surface) and tetrahedron (in volume). The discretization is performed by mesh function in COMSOL.

In the simulation, the calculation time is sensitive to the model design and mesh. In our model, the size of antenna is 300 nm, the smallest structure is

40 nm. In order to obtain precise simulation result, the finest mesh size need to be 5−10 times smaller than the finest feature ($\frac{w}{10} \sim 5$ nm). The coarsest size is also limited by the wavelength 670 nm ($\frac{\lambda_0}{10} \sim 70$ nm). If we put the 50 μm waveguide and antenna in the same model, the mesh of waveguide will significantly increases the scale of matrix. Besides, the dipole emission coupling, scattering and interference occur in the domain around the antenna. The long-range propagation can be estimated from the far field asymptotic approximation at the edge of boundary. Therefore our model is wrapped by a spherical shell (see Fig. 3.3). The computation window diameter equals twice the fluorescence wavelength.

Boundary condition

The FEM is solving a boundary value problem. When we simulate field in infinite space by finite domain, we need to add proper boundary condition to avoid the reflection on the boundary.

In COMSOL Multiphysics®, there are two ways to establish the boundary of the computational window: Perfectly matched layer (PML) and scattering boundary condition. PML is a layer of finite thickness surrounding the region of interest that is non reflecting and absorbing. It is implemented by geometric transformation that leads to equivalent ϵ and μ (that are complex, anisotropic and inhomogeneous) and mimick an equivalent medium with the same impedance than the initial ambient medium.

The scattering boundary condition is based on the Sommerfeld radiation conditions which ensures the radiation scatters into infinity[55].

The efficiency of these boundaries reflection depends on the incident angle. The boundary has the largest absorption for normally incident light. At large incident angle, perfectly matched layer performs better than scattering boundary condition. On the other hand, the perfectly matched layer consumes more memories due to its complex structure. It will also introduce calculation complexity in our simulations. The utilization of perfectly matched layer takes longer calculation time and it is harder to reach the convergence. The Yagi-Uda antenna assisted dipole emitter is a subwavelength structure. When the boundary is far from the source, scattered light behave as spherical wave so that we use a spherical scattering boundary condition to wrap the domain.

3.2.4 Optimization of the design in free-space

We first establish single rod resonance. The curve in Fig. 3.4 shows scattering and absorption power of single nanorod with respect to its length. The resonant rod length is 128 nm, close to our theoretical estimate of 129 nm.

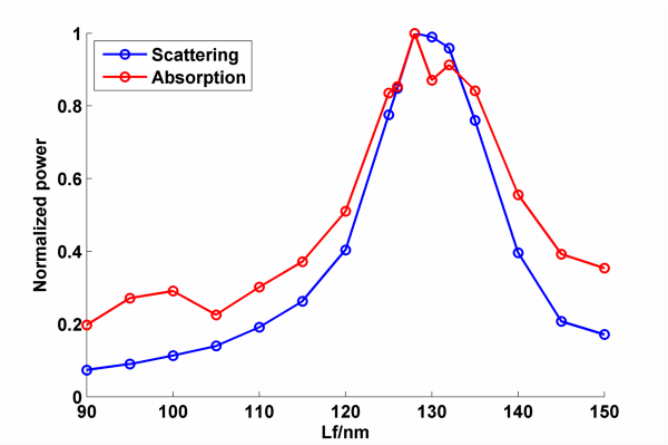

Figure 3.4: Absorption and scattering power of single nanorod in free space. The rod is excited by a dipole located 5 nm from its extremity. λ =670 nm.

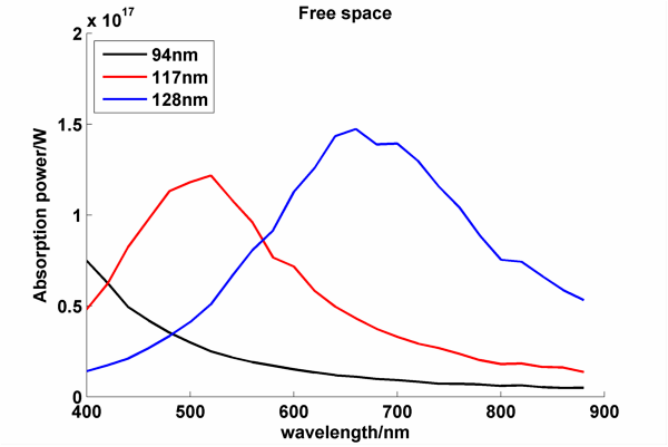

Figure 3.5: Absorption power spectrum of single nanorod excited by a dipole in free space. The rod length are $L = 94$ nm, 117 nm or 128 nm.

The spectra of 94 nm,117 nm,128 nm nanorods are shown in Fig. 3.5. We check that the 128 nm rod is resonant at $\lambda = 670$ nm. The power distribution and far-field polar diagram are shown in Fig. 3.6. We observe that the scattering pattern is perpendicular to the nanorod axis. The F/B ratio is 1, gain is 2.86.

Once we have obtained the optimal dimension of resonant nanorod, we consider a Yagi-Uda antenna. Lengths of reflector and directors are calculated according to Eq. 3.3, 3.4.

The scattering behavior of the Yagi-Uda antenna depends on the rod length and the spacing D between rods. The rod length governs the resonance of the antenna whereas spacing governs the directivity.

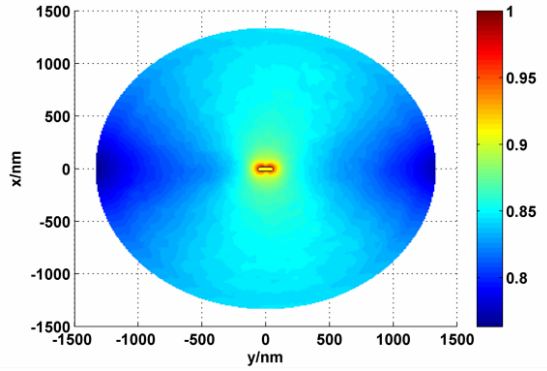

Figure 3.6: Normalized power distribution of single rod scattering in free space.

Table 3.1: Optimized dimensions of Yagi-Uda antenna ("Theory" refers to the scale law approach considering effective wavelength).

Size / Type	L_{feed}	$L_{director}$	$L_{reflector}$	D_{dir}	D_{ref}
Free space (Theory)	129 nm	116 nm	161 nm	168 nm	152 nm
Free space (Simulation)	128 nm	115 nm	136 nm	151 nm	137 nm

Based on the theory of optical antenna [41, 31], we initialized the correction factor and sweep the rod length to the estimated value before parametric study. After the rod length is optimized, we sweep the correction factor and cross-check the optimization of rod length.

The correction factor is defined as the factor between the actual spacing between antenna elements and the spacing. In simulation, the correction factor is compared to theoretical spacing:

$$D_{actual} = \frac{\lambda}{a} \times \delta \tag{3.12}$$

where D_{actual} is the actual spacing used in simulation. $\lambda = 670$ nm is the wavelength in free space. δ is correction factor. a is the theoretical factor of spacing. For reflector and directors, a is 4.4 and 4.0 (Eq. 3.6 and 3.5), respectively.

The influence of the correction factor is shown is Fig. 3.7. The forward scattered light power reaches its maximum when the correction factor is 0.9. The forward scattered power decreases from 81% to 50% when correction factor increases from 0.9 to 2.6. As an optimized result, a 3D far field distribution is shown in Fig. 3.8. The directivity along antenna +y axis is improved significantly after optimization. The optimized dimensions of Yagi-Uda antenna are shown in Tab. 3.1. The value of gain $G = 8.37$ and $F/B = 4.26$.

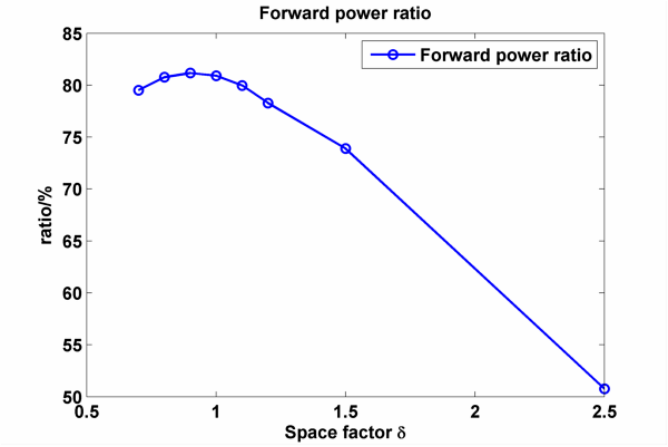

Figure 3.7: Forward power ratio as a function of correction factor δ of Yagi-Uda antenna in free space.

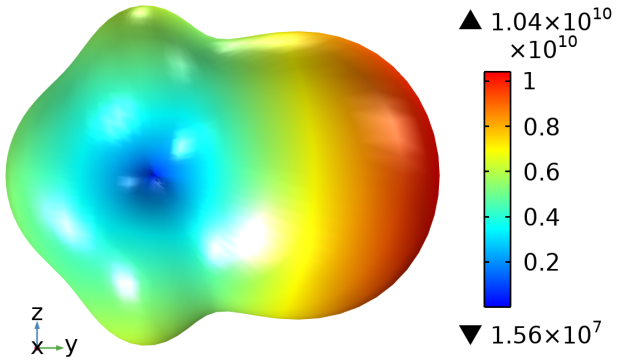

Figure 3.8: Simulated 3D far field distribution of Yagi-Uda antenna in free space. Dimensions are given in the first row of Tab. 3.1.

Robustness to fabrication error

The rod length variation can affect the antenna performance. As we know, the dimension of antenna approaches the lower limit of fabrication. The fabrication procedures will introduce errors. It is necessary to estimate the influence of fabrication error on resonance and the directivity. The resonance position with respect to feed length has been already studied in the previous section. We take the FWHM of the peak as the tolerance. When length error is within ±8 nm, the absorption power drops by half (see Fig. 3.4).

Here we focus on reflector and directors. Since the function of directors and

reflector are correlated, we make a combine parameter sweep on Lr and Ld.

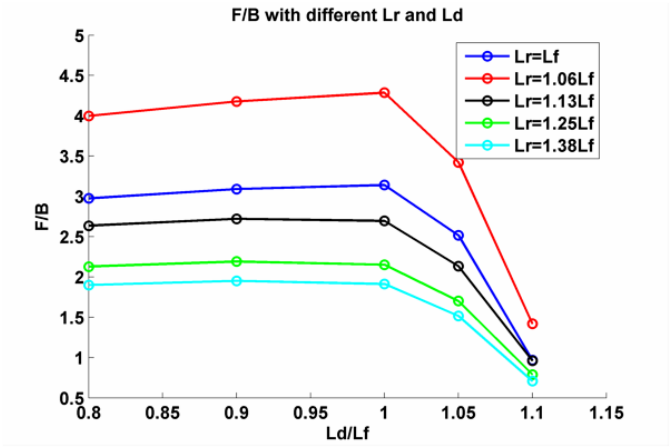

Figure 3.9: F/B ratio of far-field power with different Lr and Ld in free space. Lr sweep result is shown in lines with different colors.

As shown in Fig. 3.9, when Lr is fixed, the F/B ratio reaches its maximum at $L_d/L = 0.9$. The optimal director length is consistent with free space models. Moreover, the F/B ratio is worse for too long directors ($L_d > 0.9L$) than too short ones ($L_d < 0.9L$). In fabrication, the designed director length should be away the sensitive region. The situation of reflector is not the same as directors. We obtain the optimal F/B at $Lr = 1.06Lf$ (instead of $L_r = 1.25L_f$ in antenna theory), the optimal F/B ratio is 4.3. Similarly, when the reflector length gets shorter (close to the feed length), F/B ratio decreases faster than when the reflector length is too long.

3.3 Nanoantenna deposited on glass substrate

Considering the TiO_2 planar waveguide fabrication process is an additional step that is time consuming, we choose to investigate first QD coupled to a Yagi-Uda antenna on glass substrate to benchmark our results.

3.3.1 Simulation

Optimization of Yagi-Uda antenna

The simulation of Yagi-Uda antenna on glass is similar to the free-space case. But we add glass layer to it. The effective index n_{spp} of a plasmonic rod is modified to 2.28 leading to an effective feed length $= \lambda/2n_{spp} - 2R = 107$ nm. The simulations of absorption and scattering power as a function of wavelength shown

in Fig. 3.10. We observe a resonant feed length $L \sim 110$ nm close to the expected value.

The spectra of 90, 110, 130 nm nanorods are shown in Fig. 3.11. We notice 25 nm of rod length variation results in 250 nm of spectral shift. The optimized antenna dimensions are listed in Tab. 3.2.

Table 3.2: Optimized dimensions of Yagi-Uda antenna.

Size / Type	L_{feed}	$L_{director}$	$L_{reflector}$	D_{dir}	D_{ref}
Glass	110 nm	99 nm	117 nm	91 nm	83 nm

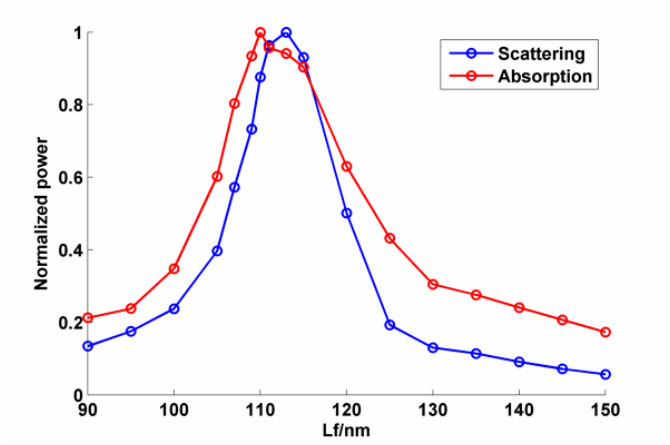

Figure 3.10: Absorption (red) and scattering power (blue) as a function of the feed length.

Simulated far field distribution is shown in Fig. 3.12. Comparing to the far field in free space (Fig. 3.8), we check that more far field is coupled to glass layer (-z direction) rather than vacuum (+z direction). The scattering keeps its unidirectional property in glass layer. Far field power to +y direction is higher than -y direction. This is in agreement with literature[24, 31]. We also make the correction factor sweep on the model with glass substrate.. Form. 3.12 is modified to

$$D_{actual} = \frac{\lambda_{glass}}{a} \times \delta, \tag{3.13}$$

where λ_{glass} is the effective wavelength in glass. $\lambda_{glass} = \lambda / n_{glass} = 670/1.5 = 447$ nm. The result shows the optimal correction factor is 0.9 (see Fig. 3.13). The simulated gain $G = 7.49$ and $F/B = 4.00$.

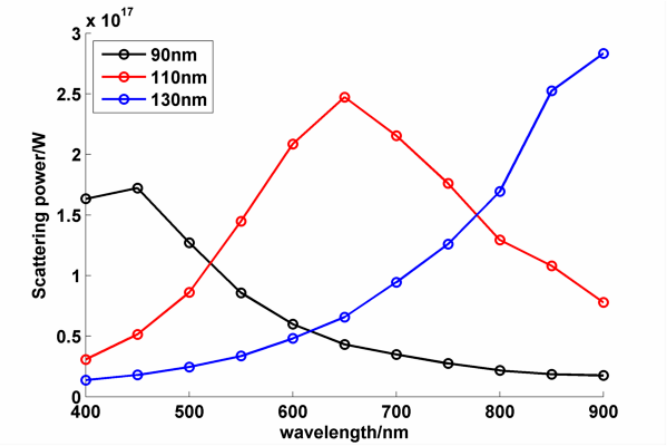

Figure 3.11: Spectrum of nanorod on glass substrate.

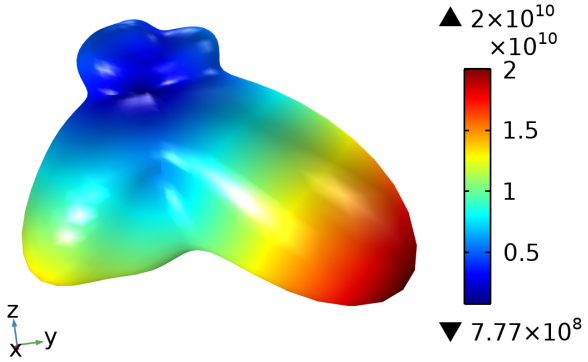

Figure 3.12: Simulated 3D far field distribution of Yagi-Uda antenna scattering on glass. The antenna is excited by a single dipole. Dimensions are given in 2nd row of Tab. 3.1.

QD alignment tolerance

During the fabrication process, quantum dots cannot be exactly deposited on the designed position. It is necessary to examine the coupling when quantum dots are deposited on different positions near the feed element. In our model, the distance between the single dipole and the feed element tip is swept from 1 nm to 32 nm. The simulation result in Fig. 3.14 shows the F/B ratio slightly decreases from 72% to 68%. The distance of single dipole does not significantly change the F/B ratio in 30 nm range, but the far-field power decreases by 97% when the single dipole moves from 1 nm to 30 nm (see Fig. 3.15). Since the interaction between

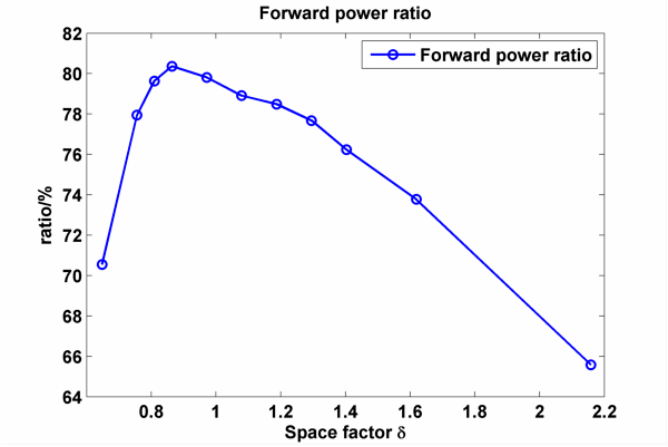

Figure 3.13: Forward power ratio as a function of correction factor δ of Yagi-Uda antenna on glass substrate.

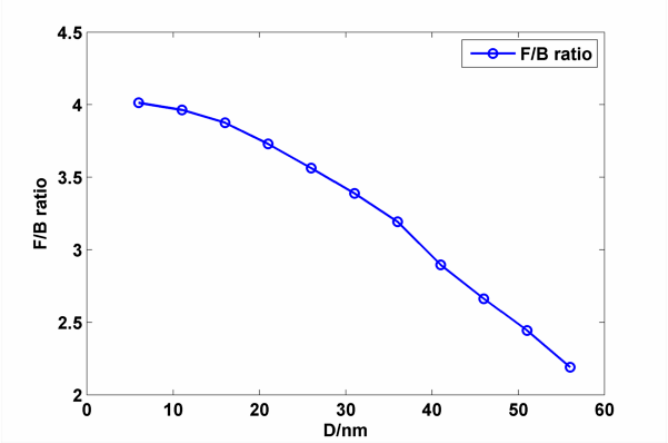

Figure 3.14: F/B ratio as a function of QD-rod distance.

dipole and antenna is in near field range $E \sim 1/D^3$, we fit the decrement by D^{-6} function.

3.3.2 Nanofabrication of the nanoantenna

Yagi-Uda antenna is fabricated by e-beam lithography, see Fig. 3.16. Polymethyl methacrylate(PMMA) photoresist is spin coated on glass substrate as a sacrificial layer. Then electron beam of SEM writes pattern on the sample. The exposure of e-beam induces polymeric chain scission in PMMA and make it soluble to developer. Then the sample is immersed in the developer, so that exposed parts are dissolved. Gold is deposited onto the sample surface and sample is immersed

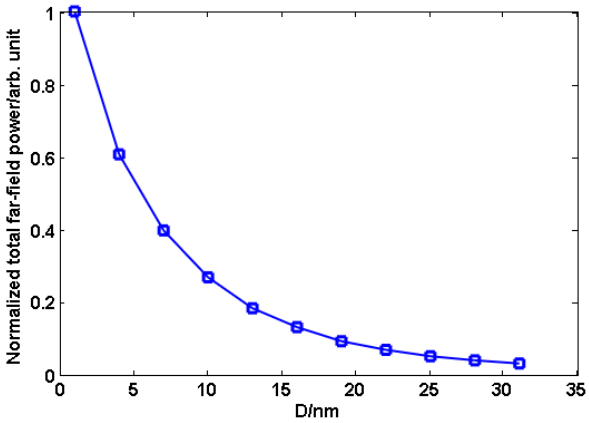

Figure 3.15: Normalized far-field power of QD as a function of distance between QD and rod. The line is a $1/D^6$ fit.

into the remover solution so that the PMMA and Au on it is lift-off. Only Au deposited in slots remains on the substrate. Finally the design is transferred to Au pattern.

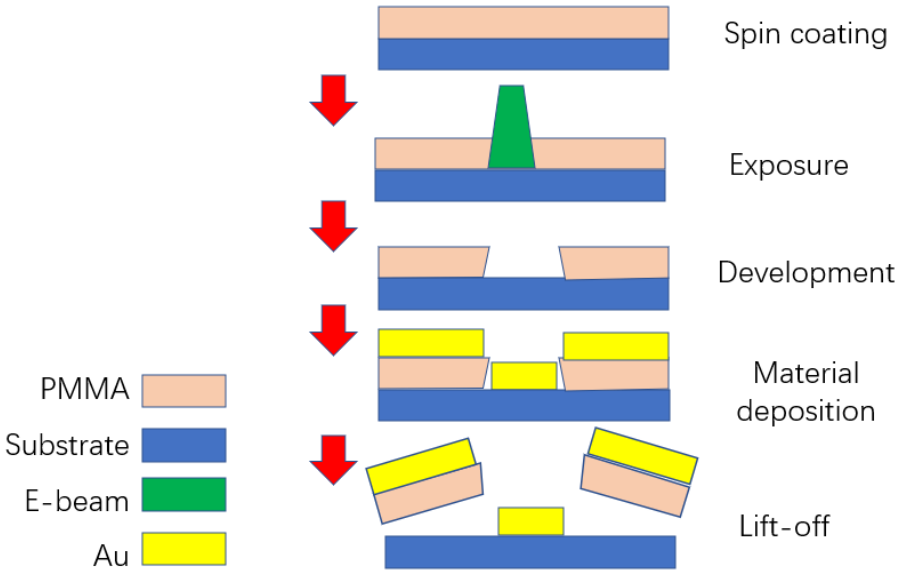

Figure 3.16: Procedures of e-beam lithography to deposit Au on glass substrate.

As we mentioned previously, Yagi-Uda antenna consists of five nanorods with $\sim$ 100 nm center to center spacing. Antenna directivity is very sensitive to the spacing (see Fig. 3.7) so that care has to be taken on the nanofabrication process.

The average size of each spot in e-beam lithography is 10∼20 nm. Error of 20 nm in rod length (90 nm spacing) can lead to a decrease from 65% to 50% for F/B ratio.

Antenna pattern can be formed by area or single pixel line. In conventional area pattern, each nanorod is represented by a rectangle. In e-beam lithography, e-beam control software divides area block or spot line into elemental spots. The electron gun exposes each spot in specific order (see Fig. 3.17). The dose of a spot is increased by its adjacent spots due to the proximity effect. The effect turns to be significant when there are only a few spots in the grid. A comparison between area pattern and line pattern can help us to understand the effect better.

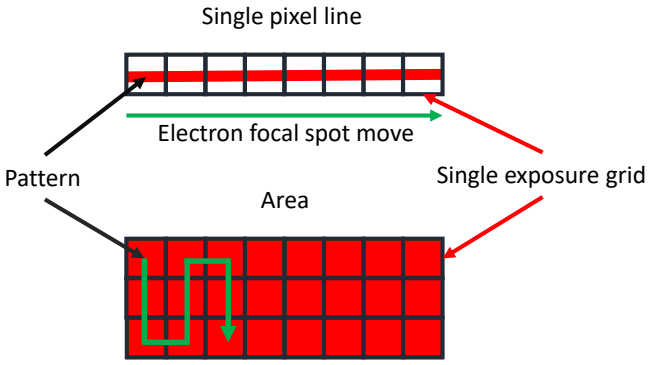

Figure 3.17: Comparison of e-beam spot of single pixel line and area pattern.

Figure 3.18: Test design of Area and single pixel line pattern. The color bar represents the dose factor of the exposure area.

The test design is shown in Fig. 3.18. According to our test, area pattern provides more accurate length control while single pixel line provides consistent width. In the matrix, we consider all combinations of dose factors and patterns.

After e-beam lithography, SEM image of Yagi-Uda antenna is shown in Fig. 3.19 and 3.20. Fig. 3.19 corresponds to area patterning and small exposure dose. Fig. 3.20 corresponds to single pixel line patterning and large exposure dose. We observe rounded nanorod only for single pixel line pattern. Average width of the rods lithographed by area patterning exceeds 50 nm (see Fig. 3.19). We privileged single pixel line since it leads to shapes permitting better coupling to a nearby QD. As the designed spacing between rods are around 40 nm, the spacing between rods will be very small or rods may be interconnected when the dose is increased. When the dose factor is small, we have observed that elements are missing due to underexposure. This suggests to use the single pixel line with high dose factor. The average width is 40∼50 nm which fits well the design.

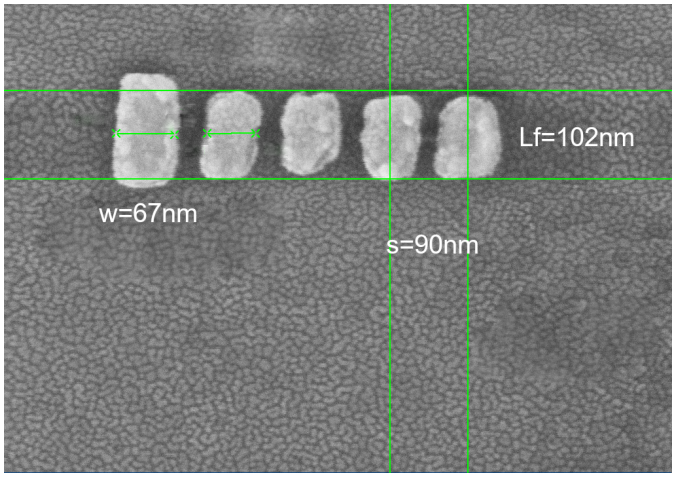

Figure 3.19: SEM image of lithographed Yagi-Uda antenna with the area e-beam exposure pattern. Measured feed length is 98 nm. Widths are 56∼67 nm. A conductive gold layer has been sputtered before SEM imaging(but after optical characterization).

The dose factor of single pixel line is slightly increased to adjust the rod width. In order to compensate the rod length, we measure average length of reflector, feed and directors for several samples (see Tab. 3.3).

We notice that nanorods are generally lengthened compared to the design. We reduce the corresponding lengths of the nanorods repeatedly to approach the target design. The average decrement of lengths are 27 nm. The comparison between the measured and designed dimensions are shown in Tab. 3.3.

The directivity of the antenna is sensitive to the length of the feed, director and reflector rod. As the experiments were progressing, we found it is harder to reduce short nanorods such as directors comparing to longer ones such as the reflector. There are two main restrictions: step size and proximity effect.

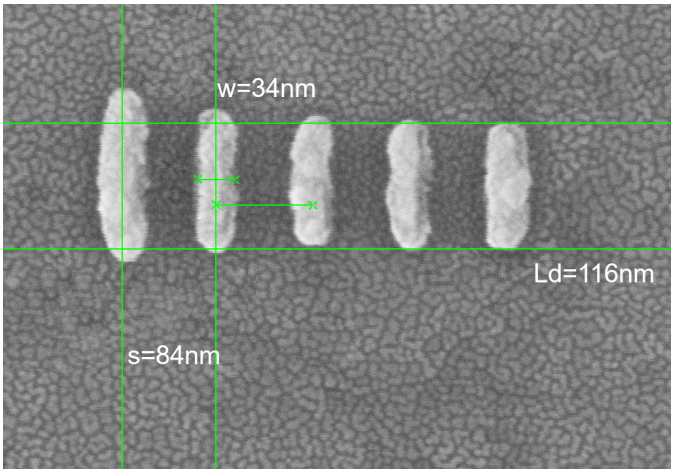

Figure 3.20: SEM image of single pixel line pattern result. Measured feed length is 116 nm. Width is 34∼38 nm.

Length/nm	Reflector	feed	directors
Measurement	131 nm	120 nm	116 nm
Design	112 nm	90 nm	84 nm

Table 3.3: Fabricated and designed rod lengths.

We first change the step size from 10 nm to 6 nm and 4 nm. Since the exposure size of a single spot is close to 10 nm, the overlap between spots is large. In the meantime, the dose factor need to be modified. Reduced step size improves the control of the rod length. Therefore spots at both ends can be precisely controlled.

Proximity effect correction

In parallel, we explore the possibility of using proximity effect correction (PEC). In e-beam lithography, each exposure spot affects its adjacent spots due to the backward scattering known as the proximity effect. The proximity effect is unavoidable in photoresist. Fortunately, we can predict or measure the influence of backward scattered electrons. One conventional method is to simulate the electrons scattering using Monte-Carlo method. The trajectory and energy of electrons simulated by Raith nanoPECS^{TM} is shown in Fig. 3.21. We can distinguish forward (blue trajectories) and backward (red trajectories) scattered electrons and estimate the energy distribution which is called point spread functions (PSF). The energy absorption of photoresist can be clearly mapped in PSF (see Fig. 3.22). There are normally 3 plateaus in PSF corresponding to forward scattering and backward scattering in the substrate. We can fit the PSF with three Gaussian

functions. The fitting parameters can be used in proximity effect correction software. The curve fitting is also shown in Fig. 3.22. In the fitting procedure, we use 3 Gaussian and a exponential function to fit the simulated energy distribution.

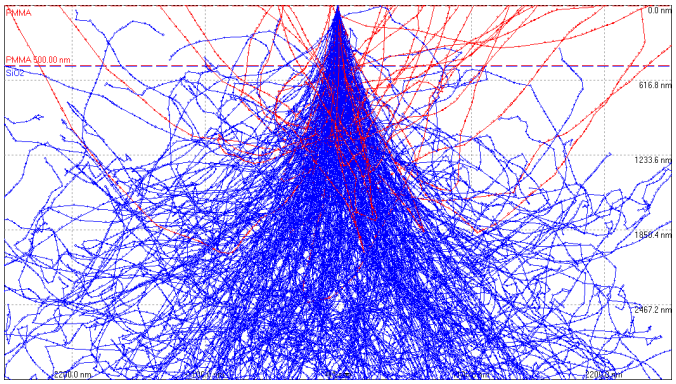

Figure 3.21: Monte-Carlo simulation of electrons scattering trajectory in the photoresist and substrate.

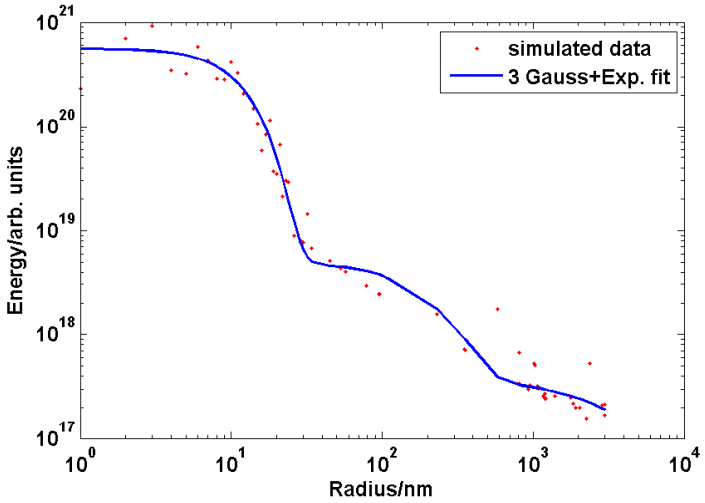

Figure 3.22: Point spread function of the electron beam scattering in PMMA and glass substrate as a function of the beam radius.

By applying PEC curve and the photoresist contrast function to the designed pattern, we can predict the photoresist profile after development. One simulation profile is shown in Fig. 3.24.

Then the correction algorithm is applied to a specific pattern. The correction algorithm divides blocks or lines to smaller elements and the dose of each element

Figure 3.23: GDSII design of antenna after proximity effect correction. The color bar represents the dose factor of the exposure area.

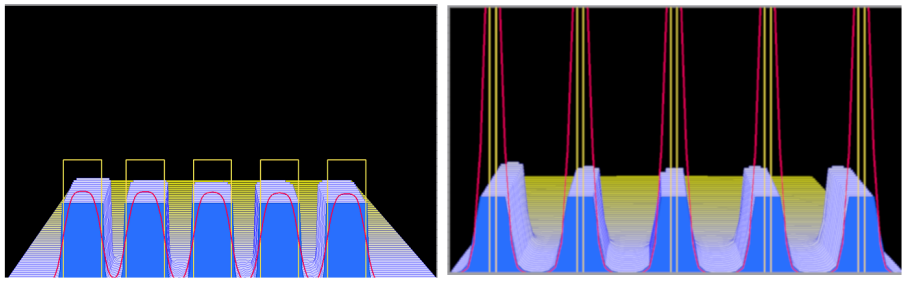

Figure 3.24: Simulated photoresist profile of a) area b) single pixel line design.

is adjusted to approach their designed shape. As an example, a design after PEC is shown in Fig. 3.23.

We achieved antenna with required dimensions. Elements close to the center of nanorods have smaller dose factor than elements at both ends. Fig. 3.25 shows the SEM image of Yagi-Uda antenna sample designed after PEC. Comparison of the fabrication results of SPL patterns with (Fig. 3.25) and without PEC correction (Fig. 3.20) reveals that the nanorod width is more stable in the PEC-corrected sample than in the sample without PEC correction.

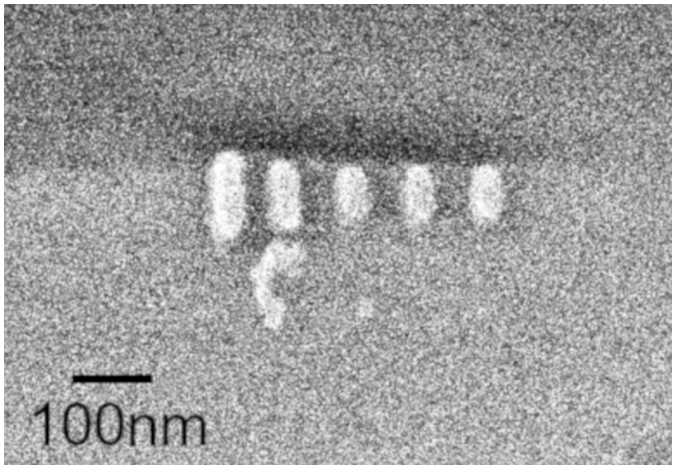

Figure 3.25: SEM image of PEC corrected Yagi-Uda antenna.

3.4 Deposition of QDs

The design requires a precise deposition of quantum dots close to the antenna feed. The precise deposition of colloidal quantum dot is a challenge. Several methods have been established in the literature:

- Surface functionalization is a method using organic ligands to bind quantum dots and surface. Small holes are fabricated on target positions by e-beam lithography, the metal layer or structure in the hole is functionalized by special ligands. Quantum dots is also modified by complementary ligands. After QD spin coating ,quantum dots is fixed to the functionalized area. The distance between QD and the antenna can be controlled within a few nanometers[56].

- Photopolymerzation of QD doped polymer close to plasmonic structures[57]. QD doped polymer is spread on the substrate with plasmonic nano structures. When the nano structures are excited by the resonant laser light, the plasmonic resonance of nano structure creates strong local field following the mode profile. High local field triggered polymerization of QD doped polymer within 10∼30 nm around the nano structure.

- Capillary force method: when quantum dots suspension shrink on sample surface, quantum dots in solvent can be driven by the capillary force and be pushed into 17∼30 nm gap in photoresist[58, 59].

- Direct deposition: Lithographed holes on photoresist are filled with quantum dots by using spin coating. Following the lift-off process of the photoresist,

the quantum dots are selectively deposited at the precise positions of the lithographed holes. The number of quantum dots and deposition quality is controlled by deposition time, hole size and suspension concentration. This is similar to the first method but without functionalization[60]. We develop this method at ICB.

- Active scanning focal probe: A fluorescent emitter is attached at the extremily of the near-field probe and approached close to the object[61, 62, 23].
- In situ lithography technique[63, 17]: After depositing QD onto the substrate, they are imaged by fluorescence microscopy. Excitation power is increase to expose the resist close to the QD before revealing the resist and evaporating gold. 50 nm positioning is achieved.
- AFM-nanoxerography: Recent study[64] introduces AFM-nanoxerography to nano diamonds (ND) deposition. The ND is positively charged. The substrate is selectively negatively charged by AFM tip. The method permits single emitter deposition below 50 nm precision.

Fabrication

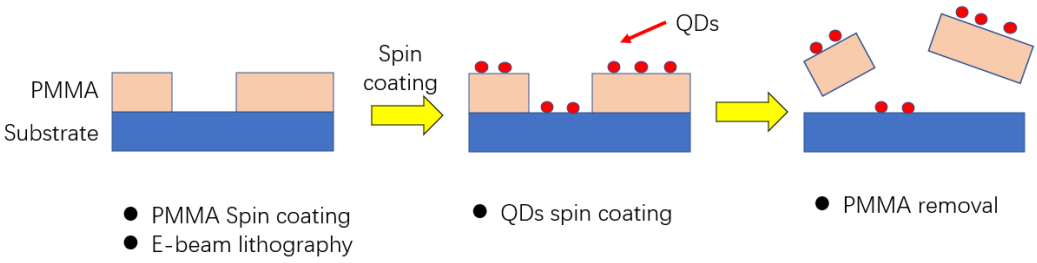

Figure 3.26: Procedures of depositing QD on the substrate.

Direct deposition is based on electron beam lithography. The procedure is shown in Fig. 3.26. The deposition of quantum dots relies on intermolecular force, for instance, Van der Waals' forces between QD and substrate. Therefore deposition and lift-off require special operations to avoid quantum dots being washed out or shifted. The original direct deposition recipe was successfully used for making 300 nm quantum dots aggregates in the lab[60]. The scale of 300 nm hole is relatively large compared to single quantum dot size (∼10 nm). Each 300 nm hole contains more than thousand quantum dots (see Fig. 3.27). In order to reduce the hole size, we pattern square hole of different dose factor and sizes in a matrix (see Fig. 3.28). Square hole sizes vary from 300 nm to 100 nm. For each hole size,

we divide the grid to 6 areas to test different dose factors from 1.5 to 4.5. The thickness of PMMA photoresist layer varies from 100 nm to 300 nm depending on the hole size. After e-beam lithography, the sample is cleaned by oxygen plasma cleaner. Plasma cleaner can remove tiny residue on sample surface and sidewalls. The surface charge produced by oxygen plasma can also improve the adhesion of quantum dots.

From the primary result, quantum dots in 300 nm to 150 nm holes are observed. QD in 100 nm hole are sometimes observed when the dose factors are above 3. The large dose factor leads probably to hole size above 100 nm. No QD was successfully deposited in 50 nm hole.

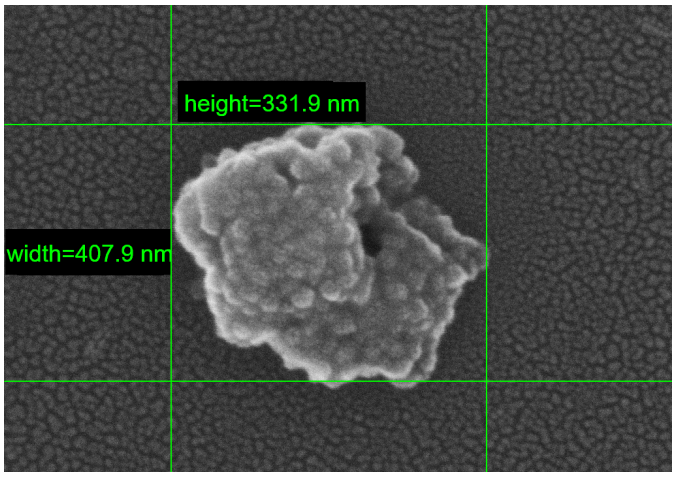

Figure 3.27: SEM image of deposited quantum dot aggregates with high quantum dots concentration. Hole size is 300 nm.

It is necessary to look into the deposition procedures. When quantum dots suspension is spin coated on photoresist surface, quantum dots accumulate at the bottom and side walls of the hole. During the lift-off process, most of quantum dots which were deposited to the photoresist layer are removed. Quantum dots on the substrate are preserved. Lift-off time needs to be controlled to guarantee that the photoresist is totally removed and quantum dots are not washed out. Therefore the number of quantum dots in single hole depends on the quantum dots concentration, the hole size and hole contrast (height/width ratio). The concentration determines the total number of quantum dots per unit area. We first gradually reduce the hole size. Then we increase the contrast of hole to reduce the probability of quantum dots deposition.

Besides, The PMMA layer can be slowly dissolved by the solvent of the QD suspension (hexane/heptane). We use 950k PMMA to delay the dissolution process. Then we control the thickness of the PMMA layer between $2 \sim 3$ times of

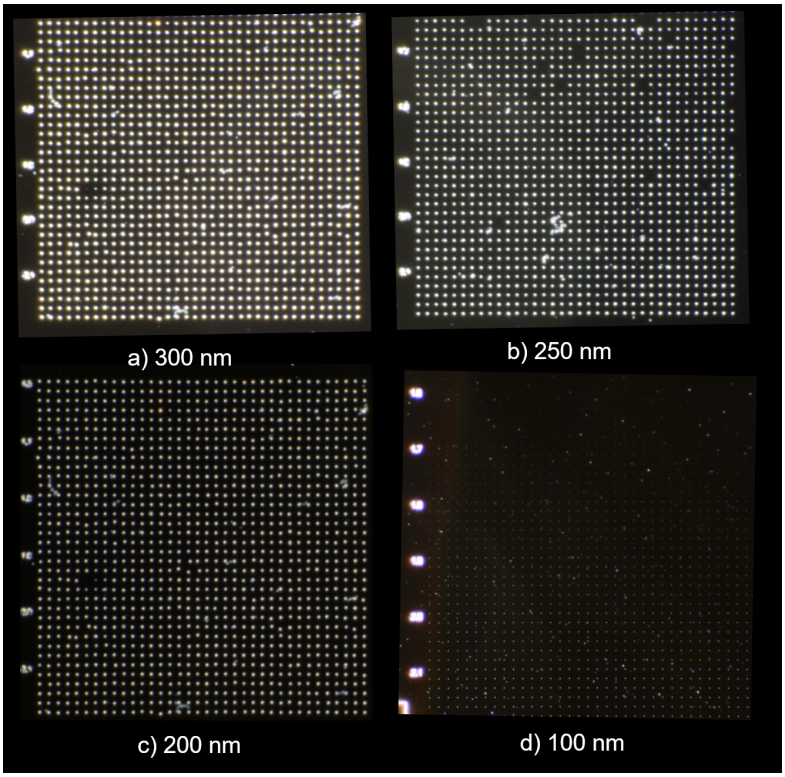

Figure 3.28: Dark field microscopy image of quantum dots deposition test pattern. The hole sizes are a)300nm, b)250nm, c) 200nm, d) 100nm. For each matrix, the dose increases from top to bottom.

the hole size (100 $\sim$ 300 nm).

By balancing between nano hole contrast and quantum dots concentration, we are able to deposit quantum dots into 60 nm nano hole. SEM image of deposited quantum dots is shown in Fig. 3.29. We notice that quantum dots are confined in 100 nm area. The size of the QDs aggregates is larger than the hole due to the disturbance in the lift-off process. By reducing the concentration of QD suspension, we can deposit 1 to 10 quantum dots in a single hole (2 QDs in case of Fig. 3.29).

3.4.1 Optical characterization of deposited quantum dots

We use confocal scanning microscopy to observe the fluorescence of QD samples. The scheme of confocal microscope is shown in Fig. 3.30. The sample is mounted on a 2 axis piezo translation stage. The laser light is focused by a high N.A. objective on the sample. The fluorescence of quantum dots is collected by the same objective. The dichroic mirror blocks the laser light. The fluorescence light is focused on an APD. The sample is scanned to acquire a confocal image. A

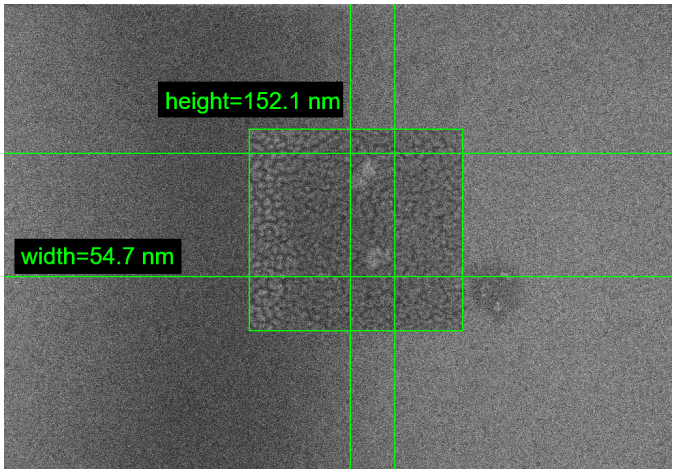

Figure 3.29: SEM image of deposited quantum dot aggregates with low quantum dots concentration. Only two quantum dots are observed. Hole size is 60 nm.

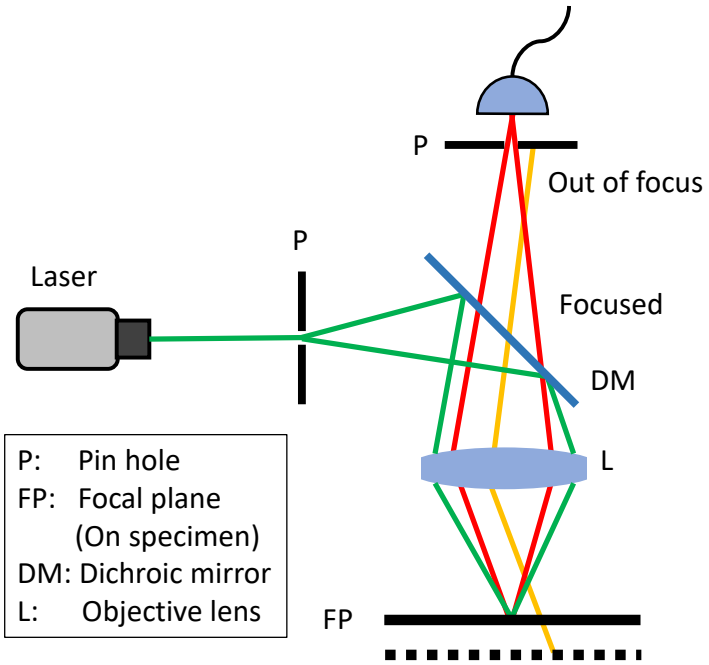

Figure 3.30: Scheme of confocal microscope. Blue light ray is reflected by dichroic mirror and focused on the sample. Fluorescence (ray in red) is collected by the same objective and pass through the pinhole. Out-of-focus light (ray in orange) is filtered by the pinhole.

confocal scanning image is shown in Fig. 3.31.

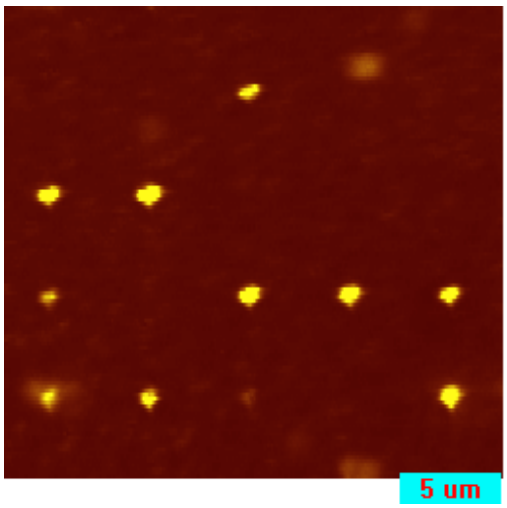

Figure 3.31: Confocal scanning image of QDs deposited on glass substrate.

By using confocal microscopy, we are able to selectively investigate the fluorescence signal of each quantum dots aggregates. We first navigate to metal grid marks around quantum dot aggregates. Each bright spot in the image corresponds to an aggregate of QDs. It is important to mention that the confocal scanning image is the spatial convolution of the laser beam shape and the quantum dots aggregate. When the piezo stage moves to a new place, the excitation and collection points are both changed.

Once the position of quantum dots is found, we can switch the output to a spectrometer. A spectrum of quantum dots fluorescence is shown in Fig. 3.32. The emission wavelength of QD is 674 nm, band width is 84 nm.

Back focal plane imaging

Back focal plane(BFP) imaging is a simple but efficient way to characterize antenna directivity[65, 56, 66]. The scheme of the optical setup is shown in Fig. 3.33. The optical path is designed to switch between back focal plane and image plane. Light output from port P is focused at plane F1. Lens L1 and L2 are the beam expander. L3 is the Fourier lens whose focus coincide with the focus of L2. The camera is put at the focus of L3 which is the back focal plane of lens L2.

L4 is a flipping lens which can switch the camera image between image and back focal planes. The focal length of L3 is half of focal length of L2, L4 is put in the middle between L2 and its focal plane. Therefore the focus of L2 and L4 are coinciding. When L4 is inserted, the plane F3 is the image plane.

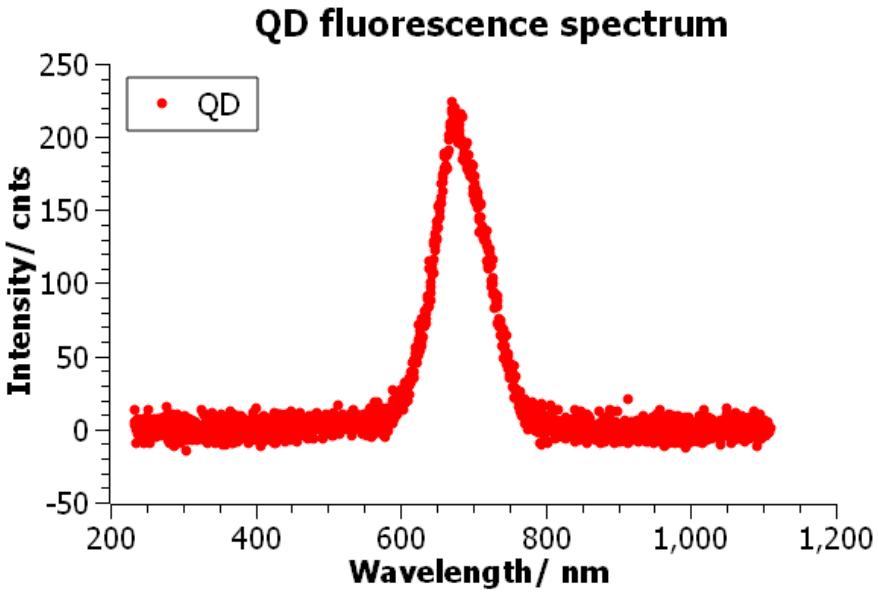

Figure 3.32: Fluorescence spectrum of quantum dots on glass.

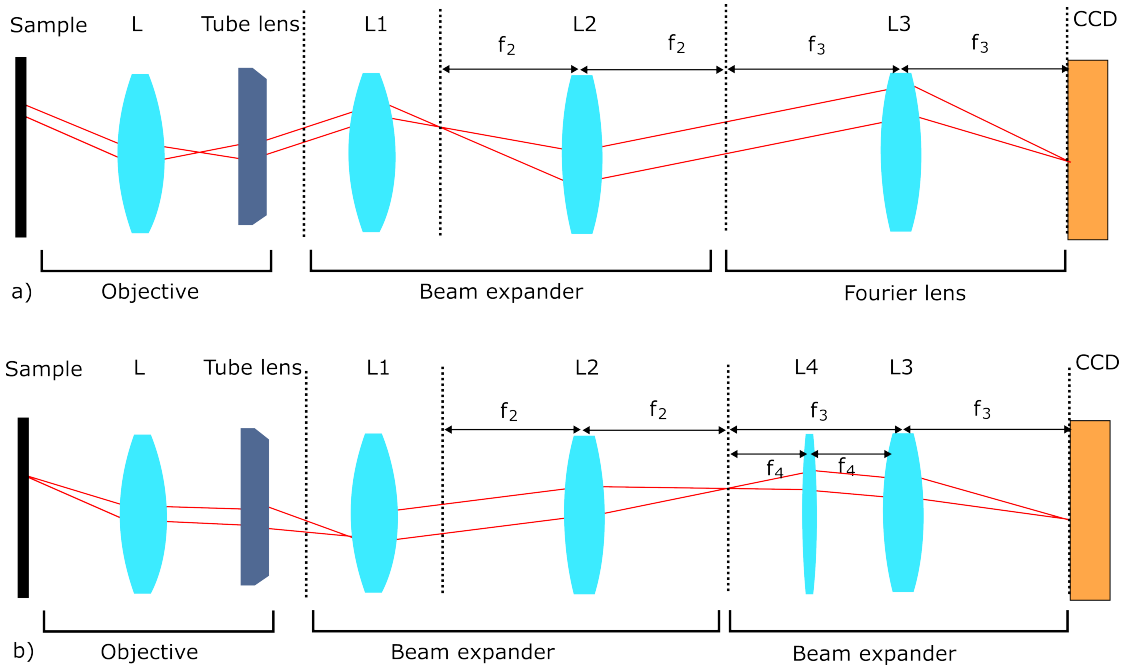

Figure 3.33: Optical setup for back focal plane imaging. a) CCD detect back focal plane image. b) CCD detect real plane image with the flipping mirror L4.

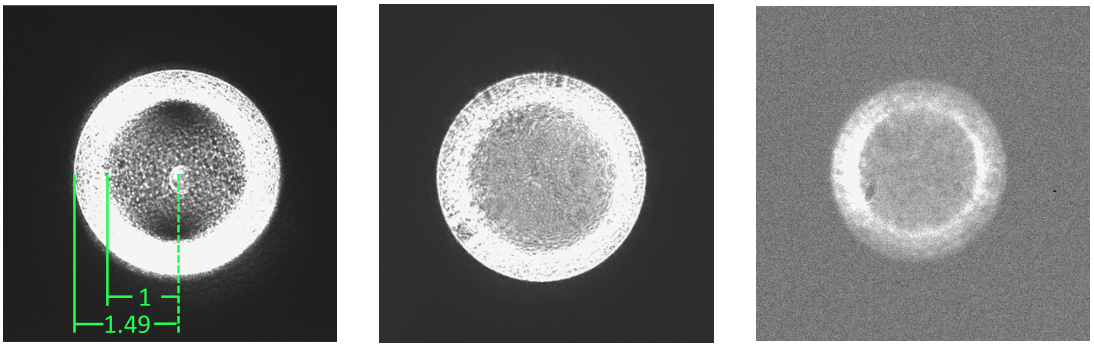

a) b) c)

Figure 3.34: Back focal plane images of a) laser spot, b)quantum dots aggregate, c) single quantum dot.

A Fourier plane image of the focused laser is shown in Fig. 3.34a. The image is a laser spot used for calibration. The bright ring correspond to total internal reflection so to incident angle θ_i in the range

$$1 \leq n \sin \theta_i \leq N.A. = 1.49. \tag{3.14}$$

The outer edge of the ring is limited by the numerical aperture of the objective (N.A.=1.49). The inner ring is limited by the total inner reflection on the substrate (refractive index $n = 1.51$). One can use the ring to align the lens. In wavevector space, the ratio between diameters of inner and outer rings follows

$$\frac{k_{\|outer}}{k_{\|inner}} = \frac{\sin \theta_{max}}{\sin \theta_c} = N.A., \tag{3.15}$$

where θ_{max} is the maximal collection angle of the objective, θ_c is the critical angle. If the ratio equals to $N.A.$, the focusing of back focal plane optics is properly aligned.

Fig. 3.34b is the BFP image of large number of quantum dots. Its distribution is isotropic. Fig. 3.34c is BFP image of a sample which contains 1 quantum dot (the number is estimated by antibunching measurement). We observe 2 main lobes corresponding to a dipole-like directional emission.

So far the quantum dots can be deposited in 60 nm area, its optical properties can be measured by confocal scanning and back focal plane imaging. Then we consider to integrate quantum dots and nano antenna.

3.4.2 QD as single photon emitter

As a single photon emitter, the fluorescence of quantum dot originates from the recombination of electron-hole in the confined band structure[67, 68, 69]. In

its band structure (a simplified model is shown in Fig. 3.35), electron in ground state $|G\rangle$ is excited to higher electron state. The electron transit to exciton state $|X\rangle$ with non-radiative decay. Then the electron transit to ground state and emit single photon.

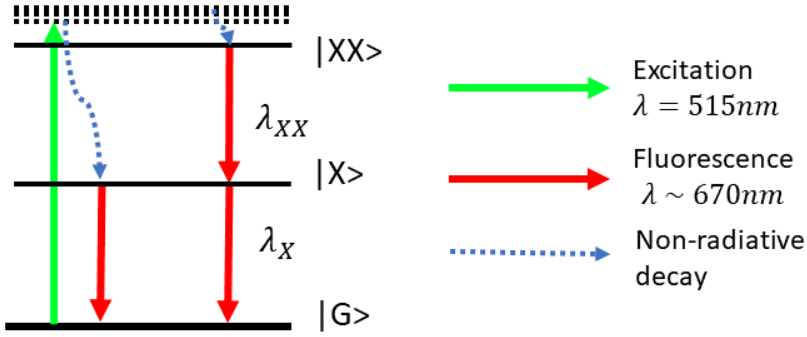

Figure 3.35: Simplified scheme of the band structure of QD fluorescence. QD absorbs a 515 nm photon (green arrow) and an electron at ground state is excited to exciton state $|X\rangle$. The excitation of biexciton state $|XX\rangle$ includes single or multiple photon process (which are not shown in the scheme for simplicity). The exciton or biexciton transition wavelength are both around $670nm$.

Lifetime measurement

The measurement of lifetime uses time correlated single photon correlation (TCSPC) and confocal microscope as we introduced in Fig. 3.36. The focus of confocal microscope is fixed at the position of quantum dot. In each cycle, picosecond laser pulse is is used to excite QD and fluorescence. APDs collect photon counts data. The pulsed laser send its synchronization signal to Picoquant TCSPC device. Each laser pulse triggers the start signal, as it is synchronized to the Picoquant TCSPC device. Time delay of fluorescene photon is recorded in the device, building a fluorescence histogram as schemed on Fig. 3.37.

TCSPC requires to prevent taking photons from previous cycles into account. Overlapping between subsequent fluorescence decay curves will cause overfitting during the calculation of lifetime. So that the repetition rate of laser pulse need to be small enough. The typical decay time of quantum dots is $10ns$. The repetition rate of laser pulse should not be larger than 100MHz. We use 40MHz or 20MHz pulsed laser.

The measured decay curve is the convolution of real time response signal and the IRF. The instrument response function (IRF) is measured by sending the laser

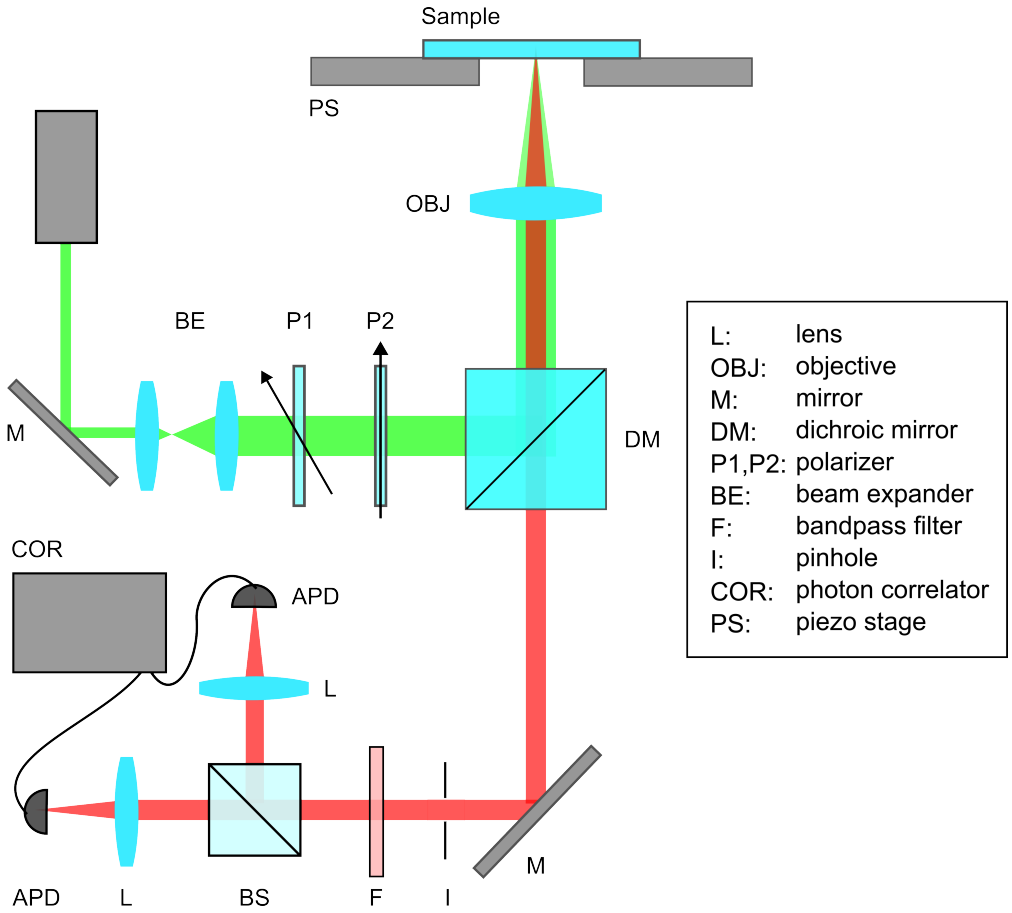

Figure 3.36: Optical setup for lifetime and photon antibunching measurement. Lifetime measurement: Synchronization signal from pulsed laser and one APD are used to make lifetime measurement. Photon antibunching measurement: Hanbury Brown and Twiss interferometry setup. Signals from bomth APDs are sent to correlator to make photon antibunching measurement.

pulse through the instrument. It is limited by the pulse duration, optical setup and APD rising time. IRF is represented in Fig. 3.38. It is of $350ps$ so that ns decay rate is measurable.

Fluorescence measurement and decay rate fit for QDs deposited in holes of 100 nm (aggregates size ranging from 100 to 150 nm) or 300 nm (aggregates sizes between 300 and 450 nm) are shown in Fig. 3.38. They corresponds to samples previously mentioned in Fig. 3.27 and 3.29. Biexponential fitting were necessary, with long and short lifetimes τ_X and τ_{XX} corresponds to exciton lifetime and biexciton lifetime, respectively. Typical value is given in Tab. 3.4.

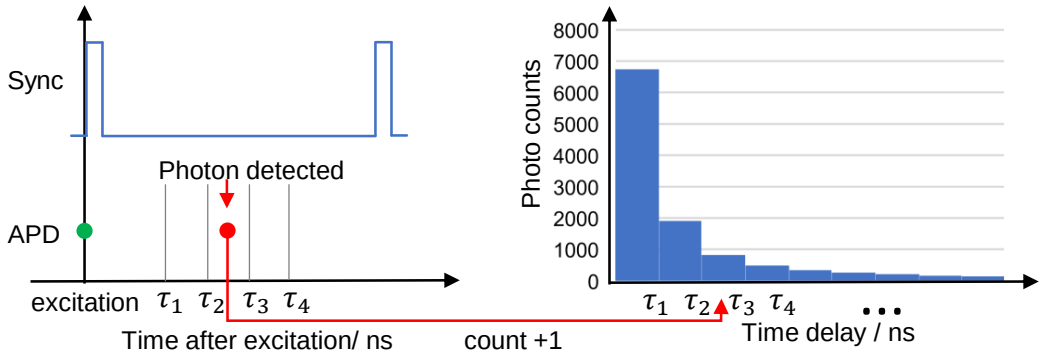

Figure 3.37: Signal diagram (left) and corresponding histogram of TCSPC process. Between two synchronization triggers, the time delay τ of the fluorescence photon is recorded. In each cycle, detected photon will add one count to the corresponding time bin in the histogram.

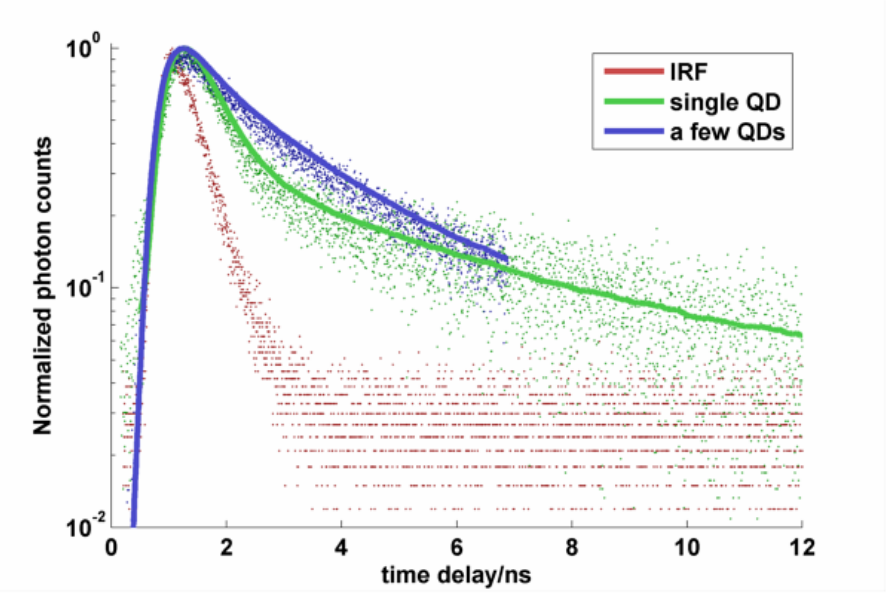

Figure 3.38: Lifetime measurement of single quantum dot (green) and a few quantum dots (blue) in 100 nm holes. Dots refers to experiment data and solid lines are biexponential fit. IRF=350ps (red). Fitting parameters for a few QDs: $\tau_X = 4.1$ ns, $\tau_{XX} = 0.27$ ns; Fitting parameters for single QD: $\tau_X = 2.2$ ns, $\tau_{XX} = 0.19$ ns.

3.4.3 Photon antibunching

Photon bunching and antibunching refer to the temporal statistics of photons. Photons can be emitted one by one (antibunching) or by group (bunching). The

Sample	τ_X/ns	τ_{XX}/ns
Single QD	2.2	0.19

Table 3.4: Measured Lifetime of single QD sample.

photon statistics reflect the property of photon source.

The photon bunching and antibunching can be distinguished by coincidence measurement using Hanbury Brown and Twiss (HBT) interferometer. The setup is shown in Fig. 3.36. Input light passes through a beam splitter and is detected on two APDs with the time delay recorded. If photons are antibunched, no coincidence is measured at zero time delay.

The result can be quantified by the second order correlation function $g^{(2)}(\tau)$:

$$g^{(2)}(\tau) = \frac{\langle N_1(t)N_2(t+\tau)\rangle}{\langle N_1(t)\rangle \langle N_2(t+\tau)\rangle}, \tag{3.16}$$

where $\langle N_{1,2}(t)\rangle$ refers to the time average of photon count events observed in detector 1 and 2.

The value of $g^{(2)}(\tau)$ at zero time delay reflects correlation of photons. If $g^{(2)}(0) > 1$, it corresponds to photon bunching, the photon bunching is observed from thermal light sources. $g^{(2)}(0) < 1$ corresponds to photon antibunching. Photon antibunching is associated to single photon emitter(single atom, quantum dot or color center). $g^{(2)}(0) = 1$ is the random case (Poissonian statistics) and is observed for laser light source.

In ideal case (ideal QD and no noise), single photon emitter have $g^{(2)}(0) = 0$. With the number of emitter increasing, $g^{(2)}(0)$ increases by[70]

$$g^{(2)}(0) = 1 - \frac{1}{N}, \tag{3.17}$$

where N is the number of photon emitter. We can determine the number of QD emitter through Eq. 3.17.

Fig. 3.39 shows the $g^{(2)}(\tau)$ curve of single QD. The red curve is a guide for the eyes. $g^{(2)}(0)$ at zero time delay is 0.386, which corresponds to a single photon emitter.

3.5 Depositing QD close to a nanoantenna

3.5.1 Fabrication

By depositing QD to Yagi-Uda antenna, we are able to make primarily test on the coupling between QD emission and nanoantenna. The fabrication can be

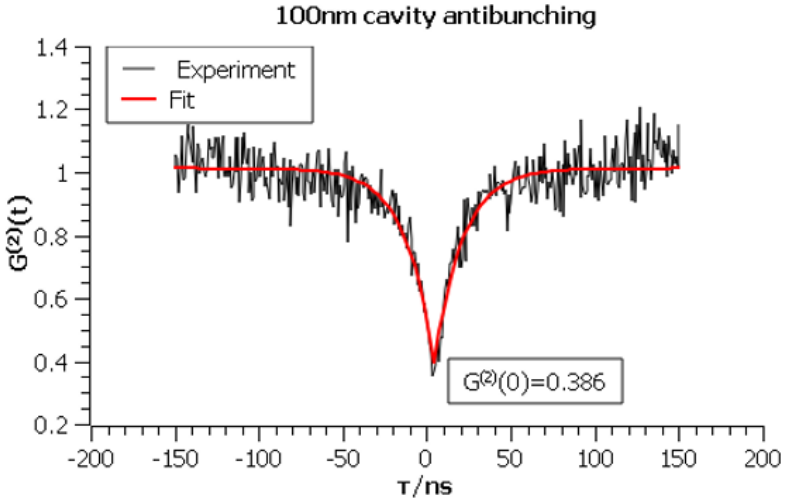

Figure 3.39: $g^{(2)}(\tau)$ curve calculated from coincidence measurement of single QD fluorescence.

implemented by two layer e-beam lithography. The first layer is gold antenna with alignment marks. The second layer is quantum dots deposited close to the feed of the antenna.

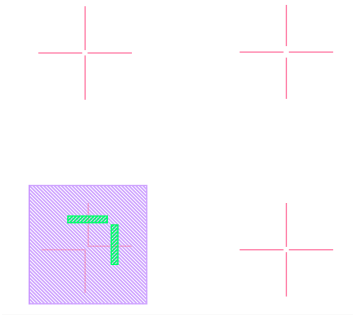

Figure 3.40: SEM align mark design for QD-antenna alignment.

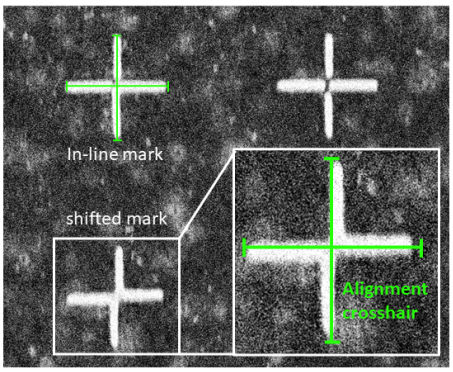

Figure 3.41: SEM image of fabricated gold mark. The zoomed image shows the alignment crosshair (green) aligned to the shifted mark.

The difficulty of integration is the alignment of quantum dots layer. As we mentioned in Chapter 2 and Sec. 3.3.1, the coupling is very sensitive to the position of quantum dots. Since the width of nanorod is 40 nm, maximal tolerable error is 20 nm (see also Fig. 3.15). The sample is first aligned by the three points alignment. Three points alignment is a software implemented function to calculate

the transformation between specimen and software coordinates system by using three points taken on both system at the same position. To achieve more accurate alignment, we program auto and manual writefield alignment in each grid. The writefield alignment directly corrects the coordinates of e-beam (writefield coordinates) before each exposure so that the correction is adapted to every exposure field. In order to meet the alignment resolution, the finest feature of writefield mark is adjusted to 100 nm. The mark is designed as in Fig. 3.40. They are constituted by single pixel line cross shape. The center of manual alignment region is set at the center of the cross. SEM image of fabricated mark is shown in Fig. 3.41. We use shifted mark (bottom left) instead of in-line mark (top left) to gain alignment accuracy. We shifted alignment upper and lower rods of the mark by half the rod width to right and left, respectively, to make the left edge of the upper rod and right edge of lower rod in-line (left and right rods are shifted in the same way). In the shifted mark, the fabrication error of rod width are compensated and we can align the crosshair to the edge of rods (see the zoomed image at the bottom right of Fig. 3.41) instead of estimating the middle point of rods (see the top left mark of Fig. 3.41).

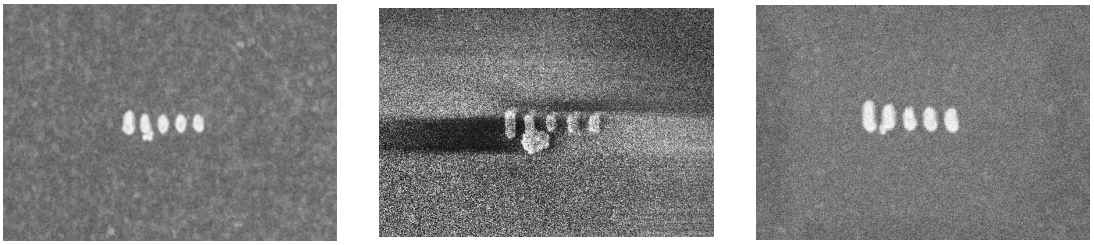

a) b) c)

Figure 3.42: SEM images of quantum dots deposited to Yagi-Uda antenna a) 60 nm hole, b) 100 nm hole before optimization, c) quantum dots slightly off-deposited.

The single pixel line mark significantly improves the deposition precision. Fig. 3.42b shows a 100 nm quantum dots aggregates deposited close to the Yagi-Uda antenna. The center of aggregates is exactly located on the end of feed element. We also found 100 nm hole is still too large to obtain a good coupling efficiency. In the meantime, we observed that quantum dots have better adhesion to gold nanorod than on glass substrate.

After gradual improvements, we finally obtain quantum dots confined in 60 nm hole, see Fig. 3.42a. Comparing to Fig. 3.42b, quantum dot aggregates are smaller and closer to gold nanorod which corresponds to better coupling. But there are still a few misaligned samples with quantum dots shifted with respect to the end of the nanorod (see Fig. 3.42c). Fabricated sample firstly need to be observed under

SEM. To protect quantum dots from bleaching, the acceleration voltage is set to 3kV and the observation time is limited to one second. Quantum dots are not bleached according to following optical characterization.

3.5.2 Optical characterization of quantum dots - Yagi-Uda antenna coupling

As a reference of quantum dots - antenna coupling, we first measure the coupling between quantum dots and single nanorod. The coupling to single nanorod can give information of polarization, enhancement and directivity. More importantly, we can check the rod length is resonant with the QD emission. We fabricate nanorods with lengths varying from 80 nm to 150 nm and characterize their resonance property.

Quantum dots coupled to single rod are characterized under confocal microscope. Resonant nanorod enhance dipole emission of quantum dot. The polarization of quantum dot emission is also modified[56, 71]. In order to analyze the polarization state, the output light is split using a polarization beam splitter. We measure the polarization along and perpendicular to the rod axis, on the two channels, respectively. The information can be combined in the same image by using color coding [56]. Color coding method normalize both channels and transform them into red and green channel in the same image. Perpendicular or parallel polarized emission spot will be in red or green. If both polarization components have similar intensity, the spot will be yellow.

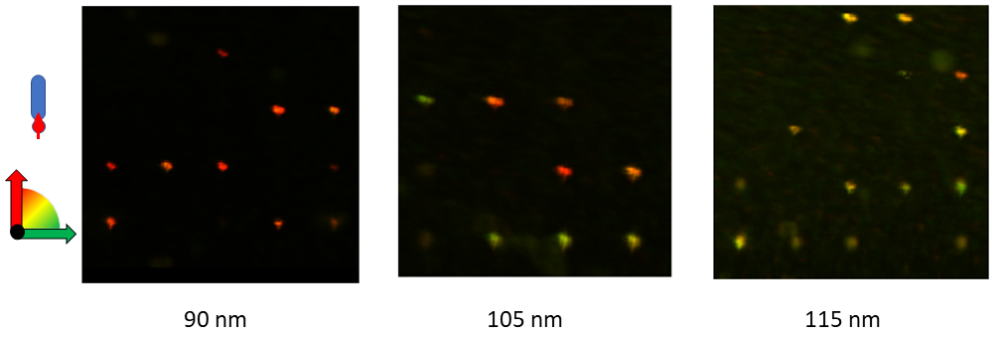

Figure 3.43: Color coded image for QD-nanorod coupled system calculated from confocal scanning image. Rod lengths of each rows are 90 nm, 105 nm and 115 nm.

Fig. 3.43 shows color coded images of confocal scan for different rod lengths. Emission of 90 nm nanorods presents polarization parallel to the nanorod orientation (red false color). If the rod length is increased from 90 nm to 115 nm, the spot

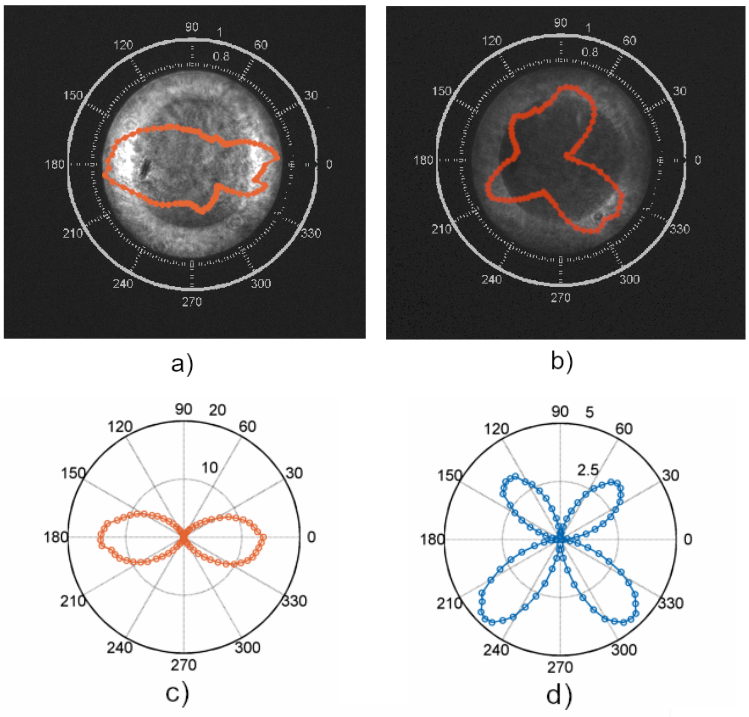

Figure 3.44: Back focal plane image of single quantum dot emission coupled to 90 nm nanorod. a) Parallel polarization, b) Perpendicular polarization, c) Numerical simulation of the far-field electric field polarized parallel to the nanorod, d) Numerical simulation of the far-field electric field polarized perpendicular to the nanorod. For the simulation, the dipole oscillates along rod axis and is 5 nm away the rod.

color gradually changes from red (parallel polarization) to yellow (unpolarized).

These color coded images confirm that resonant nanorod can modify the polarization of quantum dots along its orientation. The optimal rod length (90 nm) observed in the experiment is shorter than the simulated optimal value (110 nm). The difference can originate from the overall fabrication error, different permittivity of evaporated gold material or difference of shape between simulation and experiment.

The directivity is the investigated by back focal plane imaging. We add an analyzer before CCD camera in the setup described in Fig. 3.33. In Fig. 3.44a,b, the Fourier rings present different shape depending on the polarization. The parallel component has two lobes which are perpendicular to the orientation of the nanorod. It shows a typical dipole-like emission pattern. The perpendicular component has four lobes, but its intensity is five times less than the parallel po-

larization. The simulated far-field distribution (Fig. 3.44c,d) fits in qualitative agreement with the experiment.

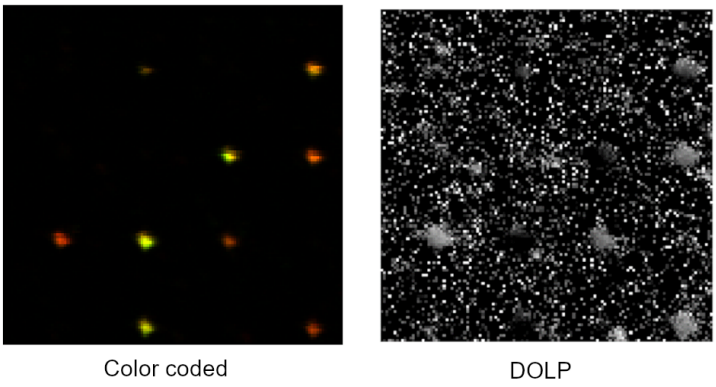

Figure 3.45: Color coded of Yagi-Uda antenna excited by QDs.

Once the polarized scattering of single nanorod is observed. The same procedure is repeated on Yagi-Uda antenna. Fig. 3.45 shows the color coded confocal scanning image. Approximately, 50% of QD-antenna system presents the expected polarization along the rod axis. Under SEM, we observed that some quantum dots drift after deposition. It could happen during the lift-off procedure. Antenna elements are very close to each other, small drift causes the adhesion to other antenna elements (mainly reflectors). Since reflectors and directors are not resonant, we cannot observe polarized light in these spots.

The back focal plane image of QDs coupled to nanorod is shown in Fig. 3.46. The overall intensity of the parallel(left image) polarized component is larger than the perpendicular(right image) polarized component. The ratio is 3.33/1. Therefore the parallel component is the main part of the scattering. The parallel component still has two lobes but light intensity on right side is larger than on the left. This is a clear sign of directional scattering, and is better seen on the polar plots (bottom figure of Fig. 3.46).

We also observe the spectrum of QD coupled to nanorod and Yagi-Uda antenna and compare them with the spectrum of QD. In Fig. 3.47, the spectrum of QD, QD with single rod and QD with Yagi-Uda antenna have similar central wavelength but the band width of QD with single rod and QD with Yagi-Uda antenna decreases from 84 nm (free space) to 53 nm and 58 nm, respectively. We also notice an increase of the emission in presence of rod or antenna but no direct comparison is possible since the number of QD into the aggregates can be different.

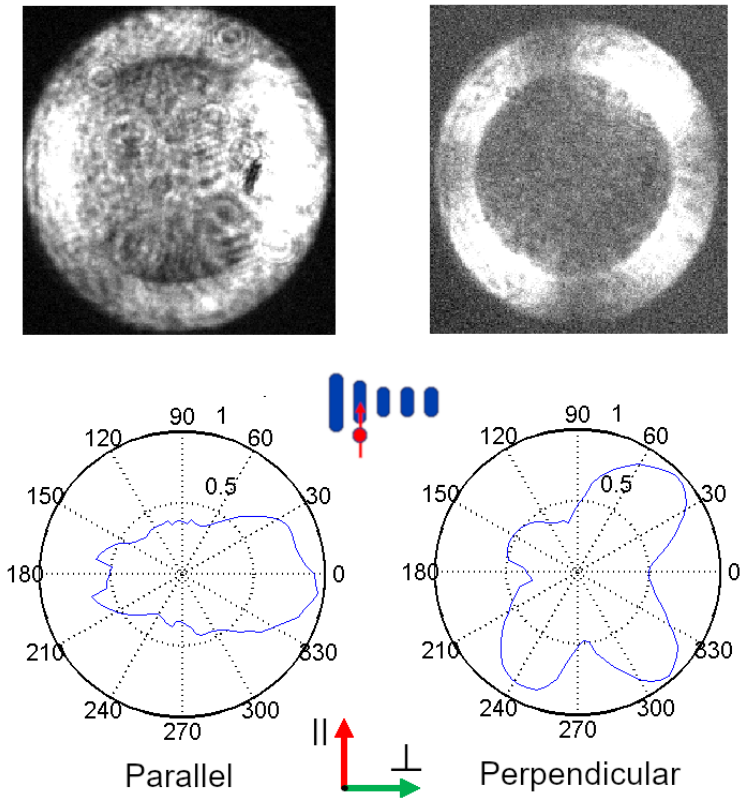

Figure 3.46: Back focal plane image of quantum dots emission coupled to resonant Yagi-Uda antenna. Polar plots are extracted from the integration of photon counts of Fourier ring. The ratio of total photon counts between parallel and perpendicular polarized component is 3.33/1.

3.5.3 Lifetime measurement

We observed the modification of QD emission directivity caused by the assistance of nanorod and Yagi-Uda antenna. As we know, there is also modification on lifetime for QD close to the resonant nanorod. In order to study the lifetime modification, we measured the lifetime of QD on glass substrate and QD close to Yagi-Uda antenna. The measurement and fitting are shown in Fig. 3.48. The data is fitted by convolution of IRF with bi-exponential decay curve. Corresponding lifetime is listed in Tab. 3.5. The exciton and biexciton lifetime τ_X and τ_{XX} of QD close to antenna decrease by factor of 0.75 and 0.32, which is a significant difference. Since biexciton lifetime can be affected by more process such as Auger recombination and charge to be checked, we only take exciton lifetime to estimate Purcell factor. The exciton lifetime of QD emission on glass and close to antenna

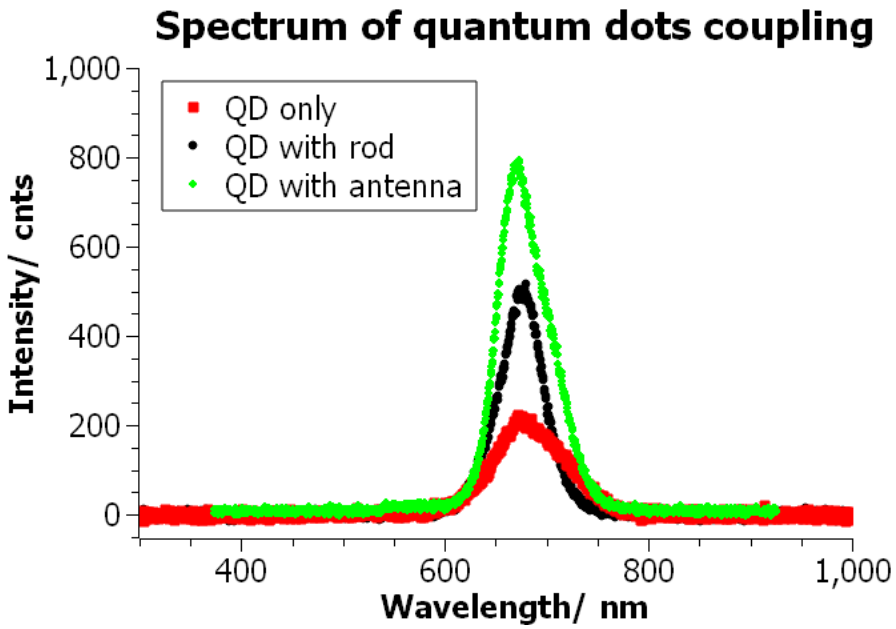

Figure 3.47: Fluorescence spectrum of quantum dots on glass (red), single nano rod (black) and antenna (green).

Table 3.5: Lifetime fitting result of QD on glass substrate and QD close to Yagi-Uda antenna

Fitting / Type	τ_X/ns	τ_{XX}/ns	A_X	A_{XX}
QD on glass	8.9	0.88	15	28
QD close to antenna	2.9	0.60	15	2333

are $\tau_{glass} = 8.9$, $\tau_{antenna} = 2.9$. The lifetime of QD emission close to antenna is three times smaller than its lifetime on glass. The Purcell factor of antenna can be estimated as $F_p \sim \langle\tau_{glass}\rangle / \langle\tau_{antenna}\rangle = 3$. In the experiment, the QD size varies from 10 nm to 30 nm. The lifetime of each sample has large dispersion. Therefore more accurate Purcell factor can be estimated by using QDs with smaller size dispersion.

3.5.4 Purcell factor of QD - antenna coupling

When a emitter is coupled to a nanorod, the resonant surface plasmon introduces new relaxation channels so that decay rate is modified.

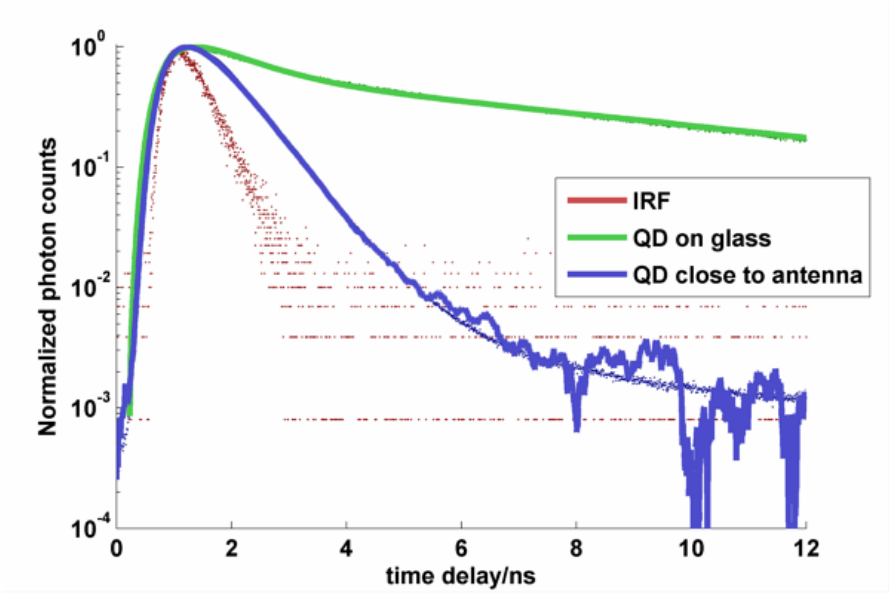

Figure 3.48: Lifetime measurement of QD on glass substrate (red) and QD close to Yagi-Uda antenna (green).

Purcell effect describe the decay rate modification[13]:

$$F_p = \frac{\Gamma_{antenna}}{n_{med}\Gamma_{QD}}, \tag{3.18}$$

In classical simulation, the decay rate can be calculated by

$$\Gamma = \frac{\omega}{2} Im\{\boldsymbol{\mu}^* \mathbf{E}\}, \tag{3.19}$$

where ω is the frequency, $\vec{\mu}$ is the dipole moment and $\vec{E}$ is the electric field at the dipole's origin.

By using Form.3.18, the decay rate can also be calculated by using the relation $\Gamma/\Gamma_0 = P/P_0$ where P is the far-field power in presence of the antenna.

We calculate Purcell factors of dipole coupled to Yagi-Uda antenna separation oscillating as a function of the distance, as presented in Fig. 3.49. The reference Γ_0 and P_0 are taken from the single dipole on glass. The curve is shown in Fig. 3.49. The Purcell factor of antenna from 5 nm to 50 nm decreases from 1000 to 1.5. Smaller QD separation leads to larger Purcell effect. Since the lifetime of QD samples disperse with QD size and the dipole orientation is not controlled, we are not able to estimate the QD distance according to the simulation.

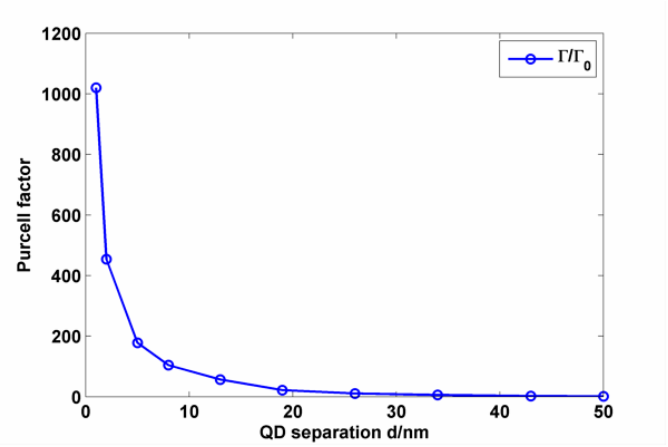

Figure 3.49: Purcell factor of QD coupled to Yagi-Uda antenna with QD separation from 5 nm to 50 nm. The Purcell factor calculated by Γ/Γ_0 is consistent.

3.6 Conclusion

In this chapter, we prepared QD deposition technique and the QD-antenna system on glass substrate for the final integration. We numerically optimize the Yagi-Uda antenna design and experimentally check by confocal imaging. Optical characterization of the QD-antenna system shows the F/B power ratio $F/B \sim 4$. Sixfold polarized polarization decay rate enhancement has been demonstrated on glass substrate.

We will investigate in the next chapter application to TiO_2 waveguide excitation.

Chapter 4

Antenna assisted QD emission into TiO2 waveguide

4.1 Introduction

In this chapter, we first design antenna for coupling QD emission into TiO_2 planar waveguide. Then we present the nano-fabrication of the full design. The dimensions of experimental sample is adjusted according to the optimization. The optical characterization presents unidirectional coupling direction parallel to the antenna axis but also parasitic coupling in the perpendicular direction. Numerical simulations suggest that the most probable reason for the perpendicular coupling is the misalignment of QD.

4.2 Design of Yagi-Uda antenna on TiO2 waveguide

Extending the design of Yagi-Uda antenna in free space and on a glass substrate, we optimize the antenna on TiO_2 waveguide. To save calculation time, we separate the simulation work into proximate scale simulation to design the antenna on planar waveguide and full scale simulation to characterize scattering at the edge of the waveguide (see Fig. 4.1). The simulation of QD-antenna-TiO_2 coupling is in 1 μm scale, and the guided mode scattering at the edge of TiO_2 is in 16 μm scale. Finally we combine the two simulations to estimate the coupling efficiency and compare to our experimental results.

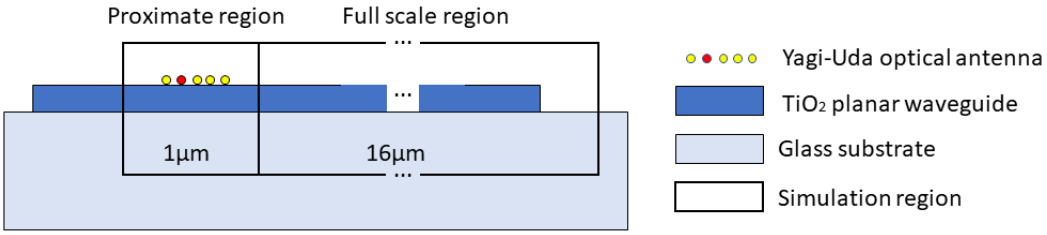

Figure 4.1: Diagram of separated simulation regions.

4.2.1 Proximate scale study: Optimization of the Yagi-Uda antenna on TiO_2 waveguide

The proximate scale study focus on the optimization of the Yagi-Uda optical antenna. The setup of model is shown in Fig. 4.2. After the optimization we can distinguish 1) QD emission in air (direct or scattering on the antenna, P_{air}), 2) fluorescence emission into the substrate (P_{sub}) and 3) fluorescence coupled to guided modes (P_{wg}). The light power in these three channels will be used to calculate coupling efficiency in the full scale simulation.

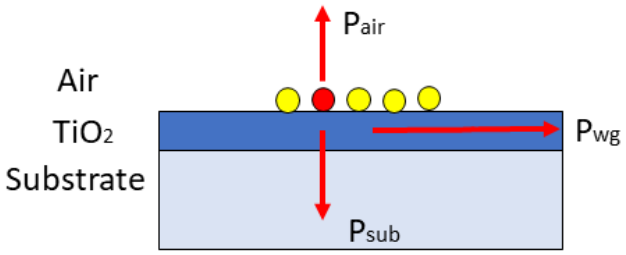

Figure 4.2: Three scattering channels of Yagi-Uda antenna on TiO_2 planar waveguide in the proximate region.

The simulation of Yagi-Uda antenna on TiO_2 is adapted from the simulation of Yagi-Uda on glass substrate. We add a TiO_2 layer ($n_{TiO_2} = 2.375$, thickness=80 nm) in the simulation region. The effective index n_{spp} is modified to 3.64. The effective wavelength is $\lambda_{spp} = \lambda_0/n_{spp} = 184$ nm. We expect resonance for $L = \frac{\lambda_{spp}}{2} = 92$ nm (we neglect the reactance term since it originates from penetration depth that is low for high effective index).

We repeat the robustness simulation again on the full integrated model (see Fig. 4.3). The optimal reflector and director lengths are found to follow the same rule as in the free space case $L_r = 1.06L = 98$ nm and $L_d = 0.9L = 82$ nm,

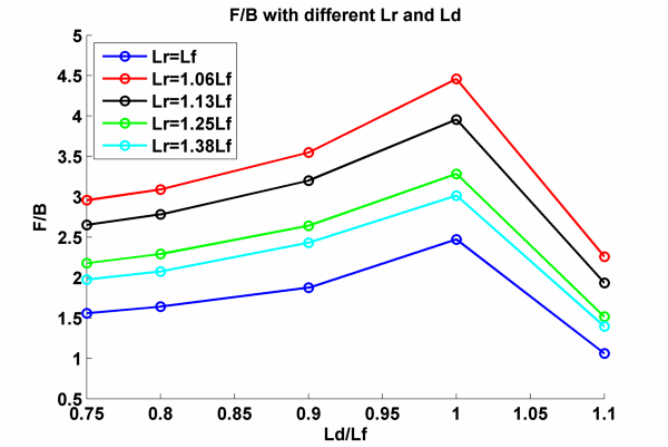

Figure 4.3: F/B ratio of far-field power with different Lr and Ld on full integrated model. Lr sweep result is shown in lines with different colors.

respectively. The directivity of the antenna is controlled by the spacing between the feed, the reflector and directors. To couple emission into TiO_2 guided mode, the spacing is modified to

$$y_d = \lambda_{wg}/4 = 97nm, \tag{4.1}$$
$$y_r = \lambda_{wg}/4.4 = 89nm, \tag{4.2}$$

where $\lambda_{wg} = \lambda_0/n_{wg}$ is the guided mode effective wavelength. We use effective index $n_{wg} = 1.72$ for a TE mode in the waveguide. By applying Form. 3.13 using the effective wavelength of $\lambda_{TiO_2} = 670/1.72 = 390$ nm and performing a correction factor sweep, we determined the optimal correction factor for the 80 nm TiO_2 waveguide model to be 0.8. (see Fig. 4.4). Therefore we have

$$y_d = \lambda_{wg}\delta/4 = 78nm, \tag{4.3}$$
$$y_r = \lambda_{wg}\delta/4.4 = 71nm. \tag{4.4}$$

We simulate the absorption power as a function of L in Fig. 4.5. The maximum absorption power is achieved for $L = 92$ nm as expected. This is valid for both single rod and full antenna. The spectrum of resonant nanorod ($L = 90$ nm, 92 nm, 94 nm) is shown in Fig. 4.6. We observe a strong sensitivity of the resonant position with the rod length (an error of 2 nm on the rod length leads to a resonant shift of about 50 nm). However, the resonant width is large so that it is not critical to couple QD fluorescence. A comparison of optimal antenna dimension in free space, on glass and TiO_2 waveguide is shown in Tab. 4.1.

The spectrum of single dipole coupled to Yagi-Uda antenna is shown in Fig. 4.7. The total far-field power is the integration of the far-field power over full space

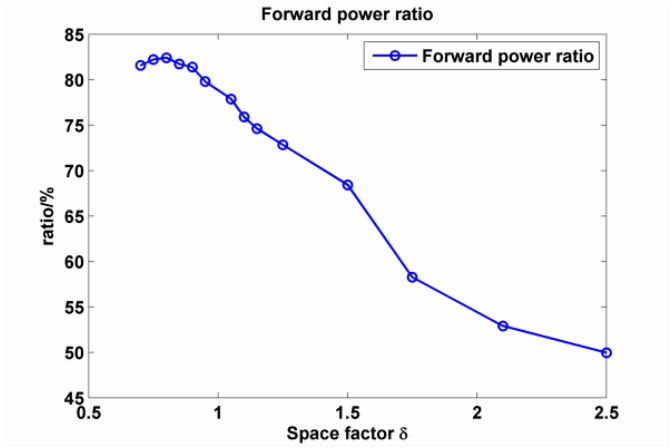

Figure 4.4: Forward power ratio (in slab) as a function of correction factor δ of Yagi-Uda antenna on TiO_2 waveguide.

Table 4.1: Optimized dimensions of Yagi-Uda antenna in free space, on glass and on TiO_2 waveguide.

Size / Type	L_{feed}	$L_{director}$	$L_{reflector}$	y_d	y_r	$Gain$	F/B
Free space	128 nm	115 nm	136 nm	151 nm	137 nm	8.4	4.3
Glass	110 nm	99 nm	117 nm	91 nm	83 nm	7.5	4.0
TiO_2	92 nm	82 nm	98 nm	78 nm	71 nm	6.3	4.7 (in slab)

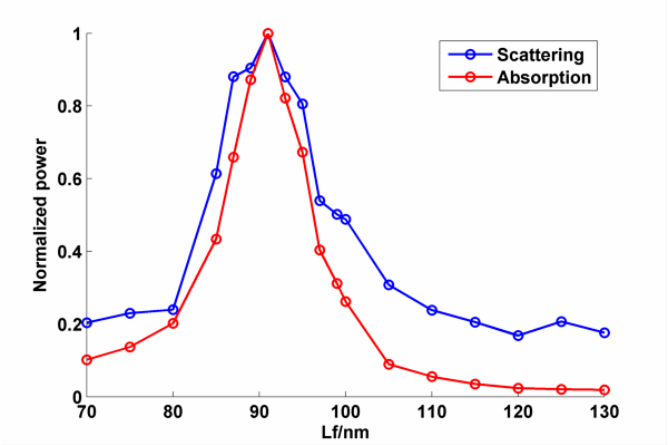

Figure 4.5: Normalized scattering power (blue) and absorption power (red) of different feed length varying from 70nm ∼130 nm of YagiUda antenna.

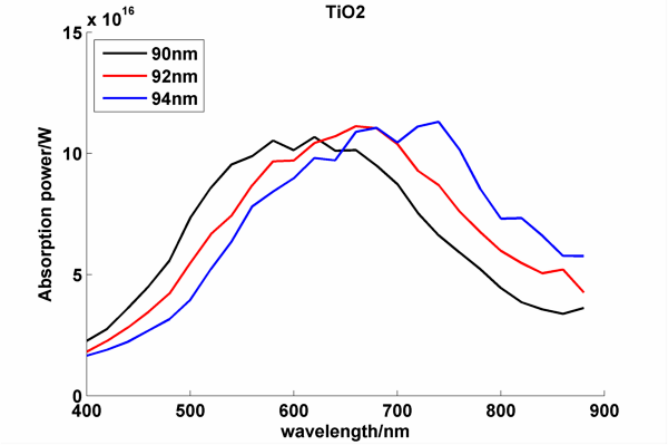

Figure 4.6: Spectrum of single nanorod excited by a dipole on TiO_2 planar waveguide.

(solid angle of $4\pi sr$). It represents the scattering spectrum. We check that the antenna is optimized for $\lambda = 670$ nm.

Fig. 4.8 presents a cross section of QD-TiO_2 waveguide coupled emission mediated by the optimized Yagi-Uda antenna. The light scattered into the waveguide, air and substrate can be clearly observed. The light is confined in TiO_2 waveguide and the light power propagates mainly towards the right side.

Simulated 3D far field distribution is shown in Fig. 4.9. Comparing to Fig. 3.12, the far field power is constrained in the waveguide film (+y direction).

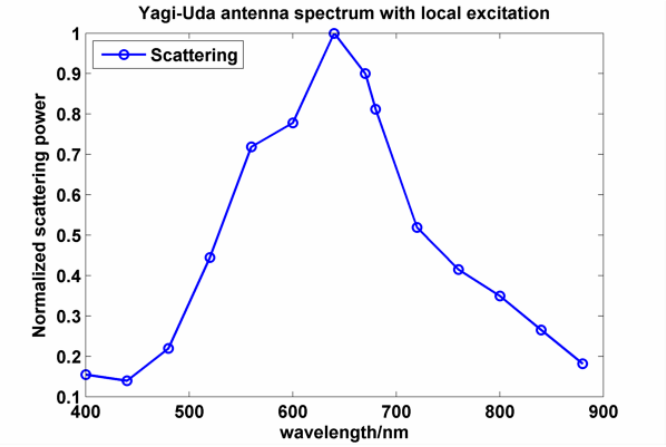

Figure 4.7: Normalized scattering power spectrum of optimized Yagi-Uda antenna on TiO_2 waveguide with local excitation.

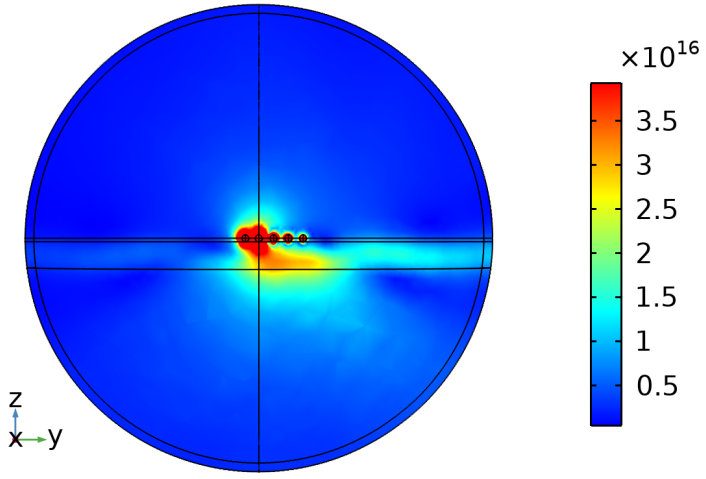

Figure 4.8: Electric field norm distribution for a single dipole $p = p\vec{x}$ coupled to Yagi-Uda antenna. The light scattered to the right side is larger than the power scattered to the left side.

Gain and directivity

The gain of Yagi-Uda antenna on TiO_2 waveguide is 6.3 (8.4 in free space, see 3.3.1). The maximal direction is along the antenna axis (toward +y direction).

In free space, we use right and left half sphere to define front and back powers (Form. 3.10). In waveguide coupling case, we only take into account the front and back light power in the TiO_2 waveguide layer. The maximal front-to-back ratio

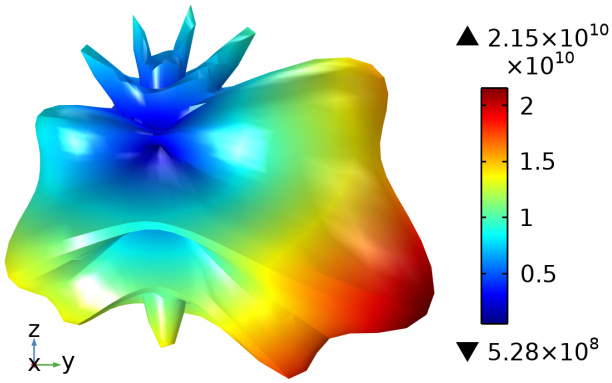

Figure 4.9: Simulated far field distribution of Yagi-Uda antenna on TiO_2 with a dipole excitation.

$(F/B) = 4.7$ (similar to the free space case), but confined in the 80 nm planar waveguide.

4.2.2 Full scale study: guided mode propagation and scattering in TiO_2 waveguide

In order to compare the simulated coupling efficiency with the experimental measurements, we make full scale (16 μm) 2D simulation to investigate the guided mode propagation and is scattered at the edge of TiO_2 waveguide. The antenna mediated power P_{wg} coupled to the waveguide is injected into the 2D simulation to estimate the light scattered at the end of the planar waveguide.

2D simulation

We consider a model with an active input port and guided mode propagation (see Fig. 4.10). The input port emulates the directional light coupled from the proximate scale simulation (P_{wg}). The guided mode propagation is regarded as lossless propagation.

The model is simulated by 2D COMSOL simulation (see Fig. 4.11). A 16 μm long, 80 nm thick TiO_2 waveguide is modeled on glass substrate. The waveguide is excited by a numerical port at the left edge of the simulation region. We observe light propagates along the TiO_2 waveguide and scattering at the right edge.

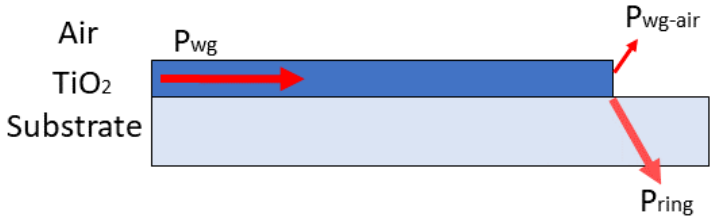

Figure 4.10: Three scattering channels of quantum dot fluorescence.

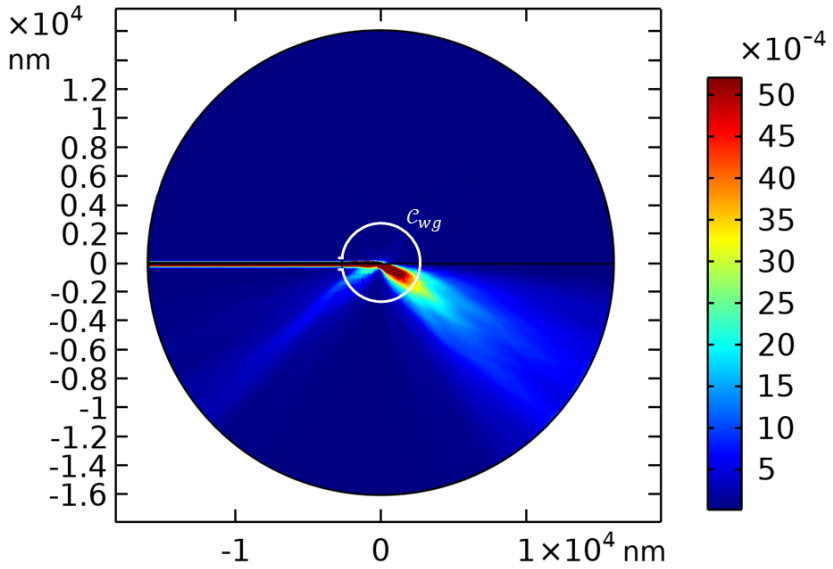

Figure 4.11: 2D simulation of light (TE mode) scattering at the edge of microdisk. The output power is integrated over the circle $\mathcal{C}_{wg}$ excluding the TiO_2 waveguide part.

Coupling efficiency

In the experiment, we can measured the light scattered at the output of the planar waveguide and compare it to emission measured at the QD position. This corresponds to

$$\eta_{out} = \frac{P_{ring}}{P_{center} + P_{ring}}, \tag{4.5}$$

where P_{ring} and P_{center} are light power collected by the objective from the end of the waveguide or directly from QD, respectively. The simulated coupling efficiency is calculated in the same way to be compared to the experimental value.

As we mentioned before, the QD radiative power is divided into three channels:

$$P_{rad} = P_{air} + P_{sub} + P_{wg}. \tag{4.6}$$

The coupling efficiency between the quantum dot fluorescence and the waveguide is

$$\eta_{wg} = \frac{P_{wg}}{P_{rad}}. \tag{4.7}$$

It measures the ratio of the radiated power coupled to the waveguide.

From the proximate scale model, we estimate the fluorescence light emitted directly from QD (P_{sub}) or at the edge of the waveguide (P_{wg}). The corresponding coupling efficiency are

$$\eta_{sub} = \frac{P_{sub}}{P_{rad}} = 0.37, \tag{4.8}$$

$$\eta_{wg} = \frac{P_{wg}}{P_{rad}} = 0.44. \tag{4.9}$$

In the optical characterization, the sample is installed on the confocal microscope. The excitation laser beam is focused from the substrate side by an immersion objective. the numerical aperture of the objective lens is $N.A. = 1.49$, the refractive index of immersion oil and lens system is $n_{imm} = 1.51$. So the collection angle is

$$\theta_{col} = arcsin(\frac{N.A.}{n_{imm}}) = 80^{\circ}. \tag{4.10}$$

In the full scale simulation, the collected power is defined by the far-field power integration over spherical crown with 160° opening angle.

$$P_{col} = \int_{-\theta_{col}}^{\theta_{col}} P(\theta) d\theta. \tag{4.11}$$

We calculate the collection efficiency of light scattered at the edge of the disk as

$$\eta_{ring} = \frac{\int_{-\theta_{col}}^{\theta_{col}} P_{out}(\theta) d\theta}{\int_{\mathcal{C}_{wg}} P_{out}(\theta) d\theta}, \tag{4.12}$$

where P_{out} is the light scattered at the output and $\mathcal{C}_{wg}$ is a circle excluding the waveguide (see Fig. 4.11). We obtain $\eta_{ring} = 0.74$. The collection efficiency of the light directly scattered into the substrate η_{sub} is calculated in the same method $\eta_{center} = 0.49$.

The final ratio between the scattering collected in the center and at the edge is

$$\eta_{simulation} = \frac{P_{wg}\eta_{ring}}{P_{rad}\eta_{sub}\eta_{center} + P_{wg}\eta_{ring}} = \frac{\eta_{ring}\eta_{wg}}{\eta_{ring}\eta_{wg} + \eta_{center}\eta_{sub}} = 64\%.$$

We can reasonably assume that P_{sub} originates mainly from the uncoupled QD emission Therefore $\eta_{simulation} = 64\%$ gives a rough estimation of the light coupled to the waveguide.

4.2.3 Robustness of Yagi-Uda antenna

During the transition from the design to fabrication, we also considered the effect of changes in the antenna design. High order modes antenna supported by longer rods could be easier to fabricate and characterize. We also examined the impact of missing antenna elements.

Higher order resonant modes

In the initial design, we only consider the first order mode of plasmon resonance in nanorod. It is also interesting to investigate high order resonance modes achieved for rod length $L = k\lambda_{spp}/2$ ($k = 1, 2, 3...$). The dimensions of higher order mode design is larger than the first order mode. It is easier to be fabricated and characterized.

Director and reflector position are fixed since they are governed by the guided mode propagation constant in TiO_2 (β_{wg}). Their length are modified according to $L_d = 0.9L$ and $L_r = 1.25L$. Absorption cross section is shown in Fig. 4.12 varying the rod length from $\lambda_{spp}/2$ to $4 \times \lambda_{spp}/2$.

The four peaks correspond to four resonance modes of antenna as already seen from the electric field map on Fig. 4.13. We found the resonance strength decreases with the order of the mode. Mode profiles for each high order mode show multiple nodes between two tips of nanorod. The number of nodes equals to the order of the mode. The F/B ratio, shown in Fig. 4.12b, presents clear directivity for dipolar mode only. This is attributed to the fact that reflector and directors length have been designed for a dipolar mode. Further investigation would be needed to estimate the phase shift needed for other modes (governed by length L_r and L_d).

Impact of missing antenna elements

The function of antenna elements can be checked by removing reflector, directors and feed element. The far-field scattering with one element removed is shown in Fig. 4.14. Comparing to no-feed case, the field strength is significantly

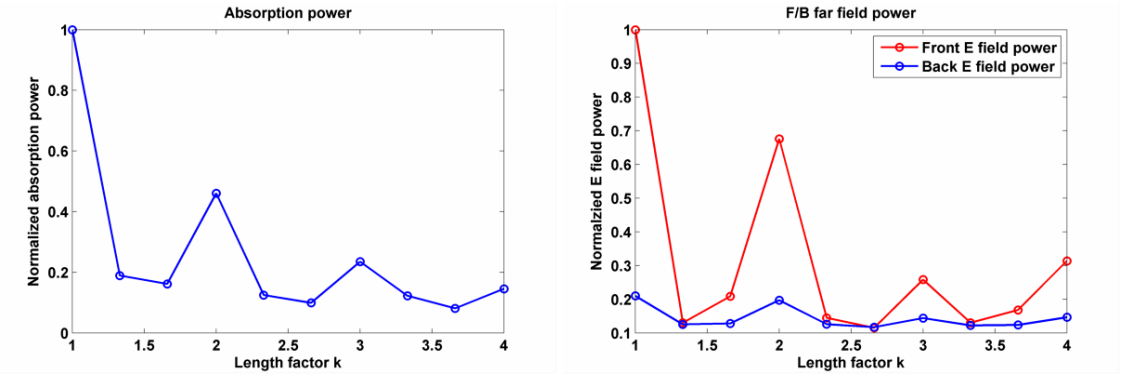

(a) (b)

Figure 4.12: Front and back scattered far-field power for different length factors of antenna elements. $L = k\lambda_{spp}/2$; director length $L_d = 0.9L$; reflector length $L_r = 1.25L \times 0.85$.

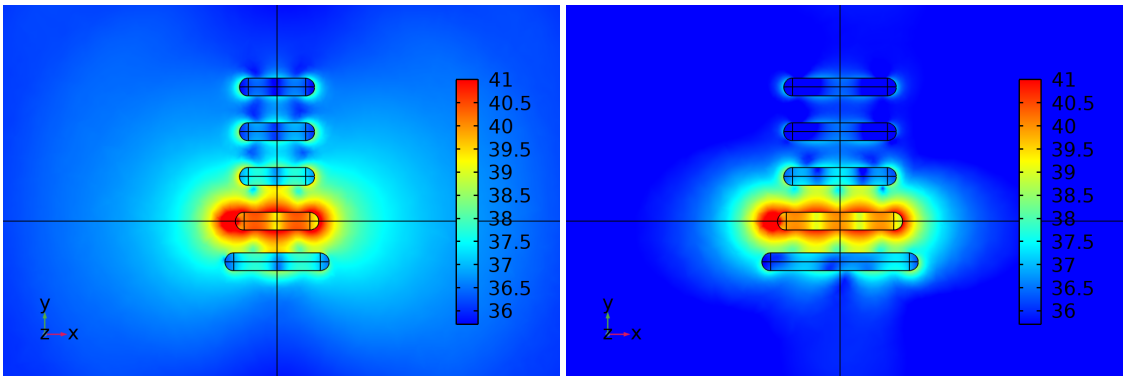

(a) (b)

Figure 4.13: Electric field of high order resonant mode. a)Second order and b) Third order.

enhanced when the feed element is added. When we remove reflector or directors, the F/B ratio are smaller than the complete antenna case. The quantitative data are shown in Tab. 4.2.

We also notice that $(F/B)_{antenna} > (F/B)_{no-ref} \times (F/B)_{no-dir}$. There is synergy effect between reflector and directors.

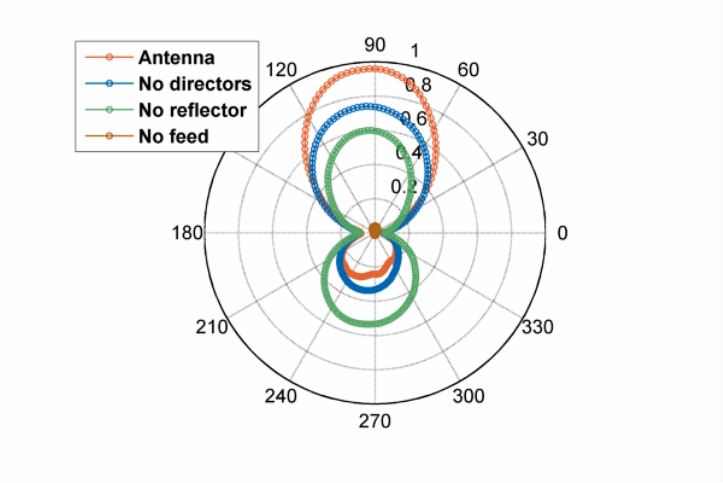

Figure 4.14: Polar diagram of antenna model with elements removed: no feed element (brown), no directors (blue), no reflector (green) and complete antenna (red).

Variation	Front power	Back power	F/B ratio
no reflector	247.00	263.95	0.94
no directors	389.97	127.59	3.05
no feed	1.03	0.36	2.86
antenna	540.17	115.28	4.70
single dipole	1	1	1

Table 4.2: Front and back power and F/B ratio in TiO_2 waveguide when differents antenna elements are removed. The power at the front and back in the TiO_2 waveguide is normalized with respect to the power at the front and back of a single dipole on TiO_2.

4.3 Yagi-Uda on TiO2 microdisk

4.3.1 Fabrication of TiO_2 planar waveguide

We use circular microdisk as the waveguide so that the optical paths from its center to every directions are the same. The light scattering at the edge can display the distribution into the waveguide. We can use it to measure the directivity and front-to-back ratio in all directions. The material of waveguide need high optical density and low absorption. TiO_2 is an easy to get and manipulate material in our lab. The refractive index of the TiO_2 film deposited in our lab is typically 2.38 or 2.5 depending on the deposition methods. We use TiO_2 with 2.38 optical index whose deposition method produces smoother surface. The feature of waveguide is

relatively large (diameter $\sim$ 50 μm). Therefore we fabricate it by UV lithography. The fabrication adheres to the procedures outlined in the literature[72]. The TiO_2 layer is firstly deposited on the substrate using PVD. Then we spin coat positive UV sensitive photoresist AZ MiR 701. The sample is then exposed through a prefabricated photomask which contains microdisk pattern. After baking and development, we use reactive ions etching (RIE) to selectively etch TiO_2 which are not covered by photoresist.

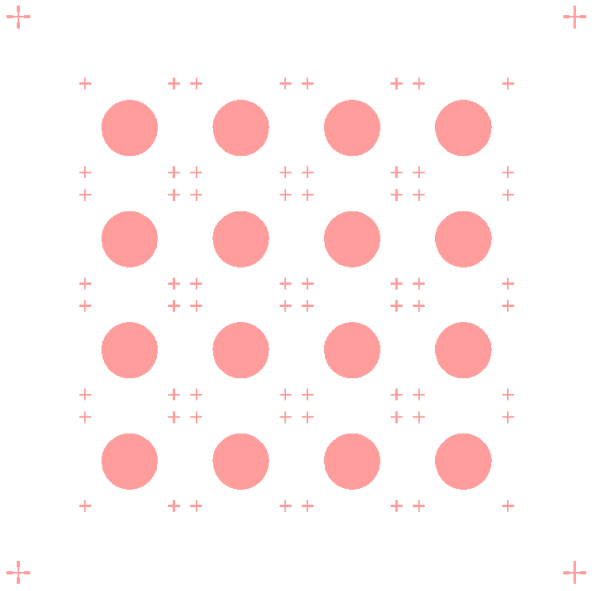

Figure 4.15: Design of TiO_2 planar waveguide and rectangular waveguide.

In optical lithography, all patterning information is written on the photomask. The photomask is prepared by commercial manufacture according to our design. The design is shown in Fig. 4.15. In the pattern, we use 100 μm grid. In each grid, there is a 50 μm circular planar waveguide. We have also fabricated strip waveguides but it is designed for future applications. We design cross marks at corners of each grid. The marks will be used to align the antenna on top of the TiO_2 disk in the following step.

It is worth mentioning several difficulties during the fabrication. The finest feature of MJB4 UV lithography is 1 μm. In our primary result, cross marks at corners were missing. We attribute this to overexposure. In the beginning, we followed recommended UV dose, but the projection system and the photomask varies from one to the other. The exposure time need to be adjusted accordingly. We add an additional factor in the calculation of exposure time:

$$\tau = \frac{D_{total}}{P} \times k, \tag{4.13}$$

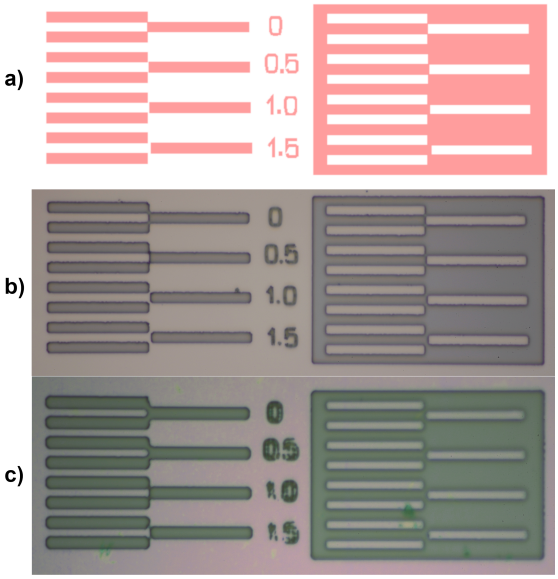

Figure 4.16: Exposure test pattern for UV lithography. a) Designed pattern, b) optimized sample and c) overexposed sample.

where D_{total} is the total dose suggested by manufacture, P is the measured UV light power, k is the time correction factor. By changing k and examining the pattern after development, we can obtain optimized k when the pattern is perfectly reproduced. In order to check the exposure result, we use special pattern shown in Fig. 4.16. When the spacing between staggered bars are 0, the optimized pattern should not have interconnection between their corners. The dose test image is shown in Fig. 4.16. The optimized k is 0.78.

In MJB4 UV lithography, we have both vacuum mode and hard contact mode. In the hard contact mode, the photomask is pressed on the sample at controlled pressure. In the vacuum mode, the air between photomask and sample surface can be removed to obtain better contact. We use hard contact mode which is sufficient to achieve 1 μm resolution.

The processed sample, following UV lithography and development, is inserted into an Oxford reactive ion etcher. The gas mixture atmosphere is excited into inductively coupled plasma (ICP) with precise control over the gas concentration and plasma excitation RF power. The TiO_2 are selectively etched by ICP. The thickness of TiO_2 is monitored using phase-shift interferometry, and the relative thickness change is calculated from the interference pattern until the desired thickness is achieved, at which point the RIE procedure is halted. The etch speed can be modified by adjusting the RF power.

Finally, the sample is immersed in N-Methylpyrrolidone(NMP) solvent to strip

the remaining photoresist layer. It has been observed that the difficulty of stripping the photoresist depends on the RF power during the RIE process. It is recommended to use a lower RF power to reduce the adhesion of the photoresist to the TiO_2 surface.

A fabrication result is shown in Fig. 4.17. The circular microdisks are TiO_2 planar waveguides. We can also observe the cross marks.

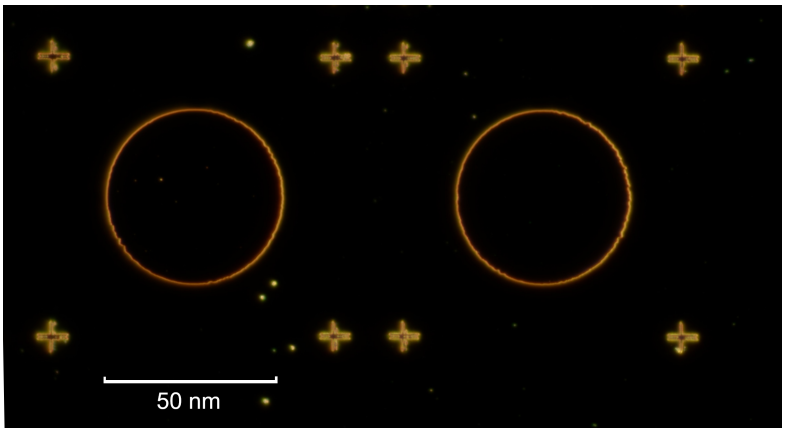

Figure 4.17: Dark field image of TiO_2 microdisks.

4.3.2 Yagi-Uda antenna on TiO_2 waveguide

The fabrication of Yagi-Uda antenna on TiO_2 waveguide need two modifications comparing to the antenna on glass. Cr wetting layer presents lower adhesion to TiO_2 than on glass substrate. The dose factor need to be adjusted accordingly. Then, the antenna layer need to be aligned exactly in the center of TiO_2 layer microdisk. In order to make connection between points on sample and points on the design scheme, we mark points under SEM as (X,Y) and points on the scheme as (U,V) respectively. The coordinates on the design is three groups of coordinates and have 6 degrees of freedom. The software can calculate transformation between the two coordinates. After the alignment, we are able to navigate to specific position on sample surface by clicking on control software.

Moreover, the imaging of TiO_2 layer is also a difficulty. The thickness of TiO_2 layer is in the range 80nm $\sim$ 150nm. With a 300nm $\sim$ 500nm PMMA layer on top of it, the contrast between TiO_2 and PMMA is low. Similarly, the contrast between TiO_2 layer and substrate is also low. Under low magnification, the pattern is noisy. One solution is to make a scratch from the edge of sample to a cross mark. The scratched part has distinct scattering property. We can follow it to find the cross mark. Once the first cross mark is found. We first make a rough alignment using global marks. Then we navigate to local marks to have a precise alignment.

After Au deposition and lift-off, the optical image of the sample is shown in Fig. 4.18.

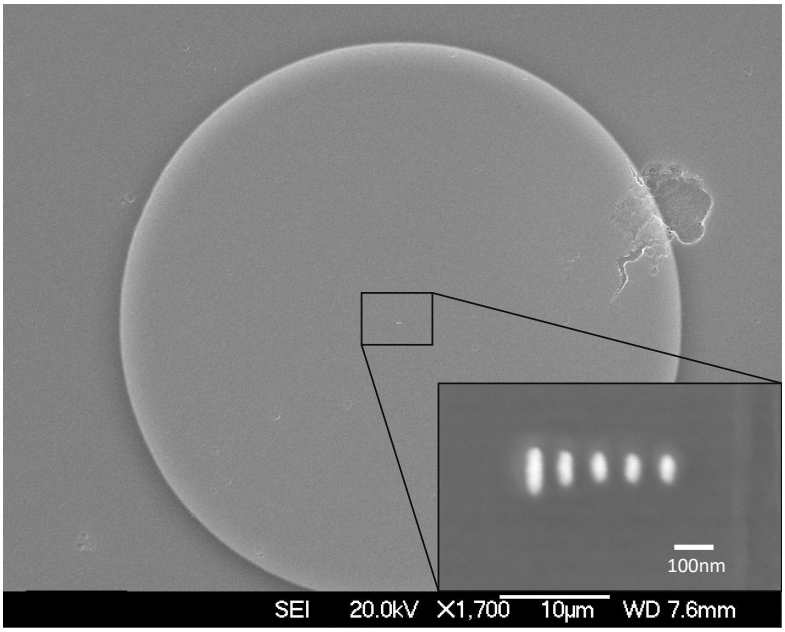

Figure 4.18: SEM image of Yagi-Uda antenna fabricated on microdisk. L_f=92 nm, L_d=83 nm, L_r=122 nm, y_r=83 nm and y_d=90 nm.

Optical characterization

In order to test the scattering property of the Yagi-Uda antenna, we observe it under dark field microscope.

Fig. 4.19 shows a dark field image of Yagi-Uda antenna on microdisk. We can measure the scattering spectrum of Yagi-Uda antenna. Scattered light is filtered by a pinhole and sent to the spectrometer. The background corrected spectrum is shown in Fig. 4.20. We observe a resonance around 650 nm $\sim$ 700 nm. The polarization dependence reflects the anisotropic scattering property of nanorods. The longitudinal resonance (polarization parallel to the feed) is slightly red-shifted compared to the transverse resonance.

We firstly examine the scattering of Yagi-Uda antenna without local emitter. The antenna is excited as a whole by using 670 nm laser to examine its scattering property. 670 nm is close to the central wavelength of CdSe quantum dot fluorescence. The focal size of laser spot is about 300 nm due to the diffraction limit so that all elements are excited simultaneously. Under dark field microscope, the antenna appear as a small dot. The sample is mounted on a software controlled

Figure 4.19: Dark field image of Yagi-Uda antenna on TiO_2 microdisk. We observe scattering at the edge of the TiO_2 microdisk and on Yagi-Uda at the center. Cross marks were used for rough alignment and square are PMMA residue after precise alignment. Dots in white squares are precise marks.

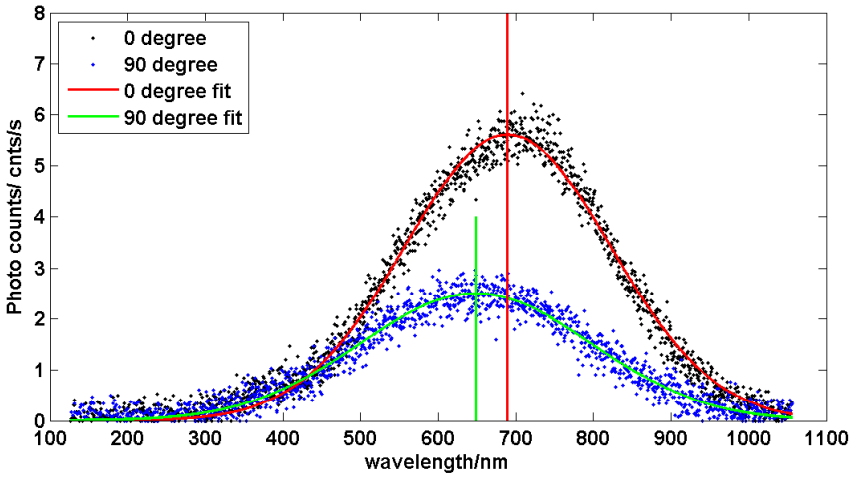

Figure 4.20: Scattering spectrum of Yagi-Uda antenna in dark field. Blue curve represents 0° polarization (parallel to the rod axis) and green curve represents 90° polarization (perpendicular to the rod axis). Spectra are fitted by Gaussian as fits are used to estimate the resonance peak.

piezo stage. Thanks to the feedback control, the piezo stage can achieve 10-100 nm precision. The laser spot can precisely cover the antenna. Once the antenna

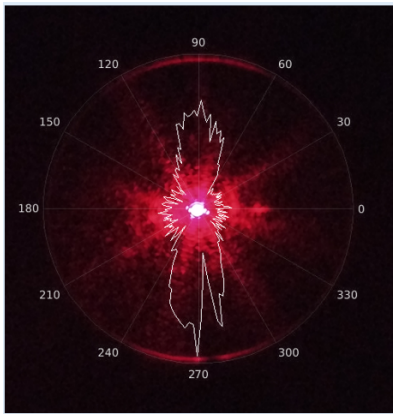

Figure 4.21: Directional light coupling in TiO_2 waveguide through Yagi-Uda antenna. Yagi-Uda antenna is excited as a whole. The incident light is polarized along the rod.

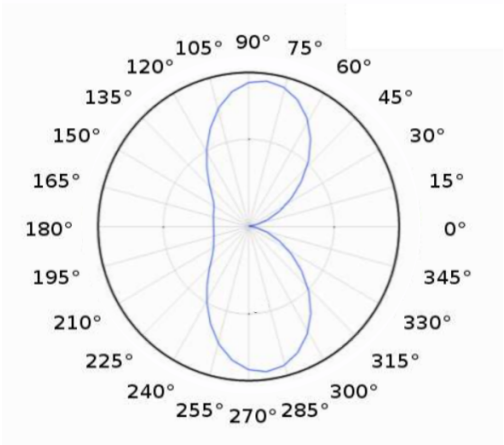

Figure 4.22: Simulated far field polar plot of antenna scattering in TiO_2 waveguide for a plane wave excitation.

overlaps the laser spot and the dark field illumination is off, a clear ring can be observed at the edge of the microdisk. The microscope image is shown in Fig. 4.21. The bright spot in the center is the laser spot deposited on the antenna. The outer ring is the light scattering at the edge of microdisk. The polar plot superimposed on the image refers to light intensity over the waveguide ring. The light is scattered perpendicularly to the antenna axis, so that no antenna effect is observed. For comparison, we also make a simulation with planar light excitation on antenna. The simulated far field in microdisk (see Fig. 4.22) fits the experiment well.

One interesting phenomenon is whether the antenna is locally excited and excited by plane wave, its far field scattering direction are orthogonal. In the local excitation case, reflector and directors are excited via the feed element. There are phase differences between antenna elements. In the plane wave excitation case, all elements are in-phase so that no antenna directivity is observed.

4.4 Directional QDs emission into planar waveguide

Finally, we have deposited QD aggregates close to the antenna feed, following the method presented in Chapter 3 (Sec. 3.5).

Antenna mediated QD emission coupled to TiO_2 waveguide is shown in Fig. 4.23. Scattered light is collected by a high NA objective (see Chapter 3, NA=1.49). Light coupled to microdisk propagates in planar waveguide and scat-

ters out at the edge. Since the light source is a local source in the center, its directional property can be estimated by the light scattered out at the edge of the waveguide. The image of scattering ring is shown in Fig. 4.23.a,b.

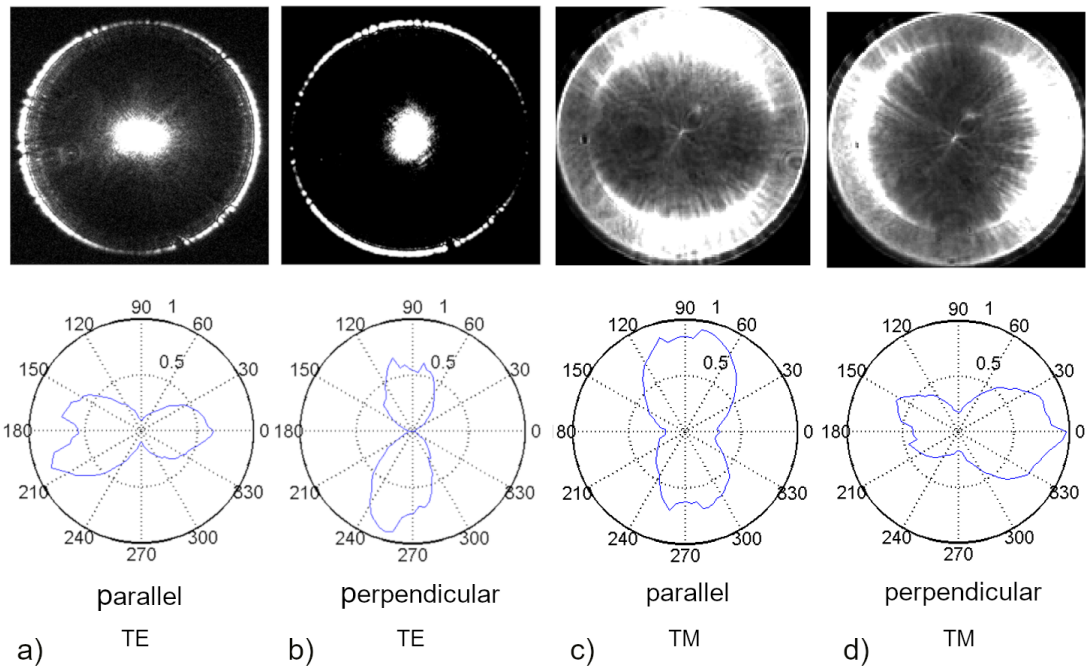

Figure 4.23: Antenna mediated QD emission in TiO_2 planar waveguide. a,b) Image plane for analyzer parallel (a) or perpendicular (b) to the rod axis. c,d) Back focal plane images for light scattered from the center. Bottom line: angular cross section of the light scattered at the microdisk edge (a,b) and in the Fourier plane (c,d).

As we mentioned in Sec.3.4.1, the setup is designed for switching between the image plane and back focal plane. In our primary result, the number of quantum dots is not controlled. In this case, we do not expect an efficient coupling between quantum dots and antenna. But we are able to study the coupling between quantum dots and TiO_2 waveguide. The real plane and back focal plane images are shown in Fig. 4.23. The perpendicular and parallel component are separately collected.

As schemed in Fig. 4.24, TM mode appears radially polarized in the Fourier plane but TE mode presents lobes perpendicular to the direction of propagation. Therefore, we can associate in the Fourier plane 4.23c,d to TM mode and image plane 4.23a,b to TE mode.

Image plane reveals that mainly TE modes are guided within TiO_2 film. Fig. 4.23.c,d presents the back focal plane when the edge is filtered out. We observe

that direct QD emission (uncoupled light) is mainly TM polarized.

4.4.1 TE and TM mode in planar waveguide

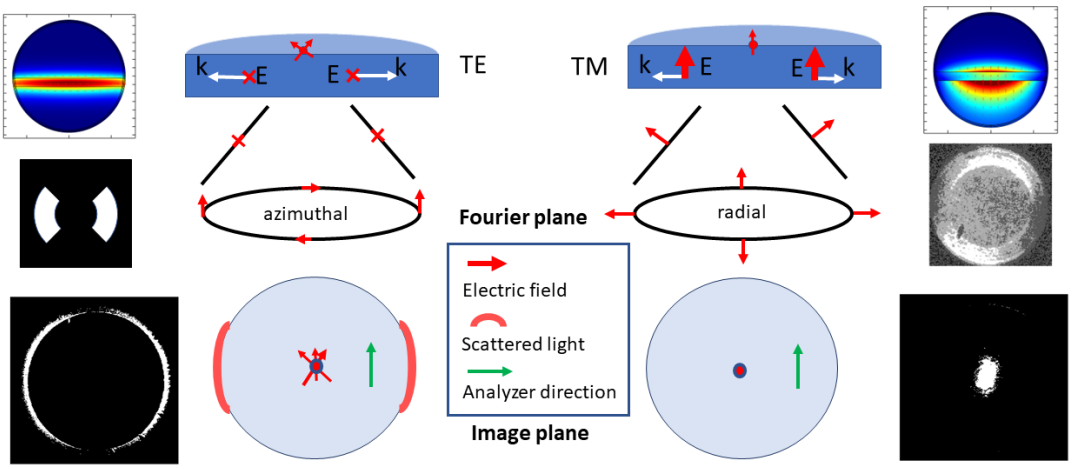

Figure 4.24: Diagram of dipole scattering in TE and TM modes. The TE/TM mode electric field are azimuthal/radial in Fourier plane. After the analyzer, the light on both sides(TE) or inline with the polarization direction(TM) is filtered out.

We calculated eigenmodes of 80 nm TiO_2 waveguide on glass substrate. The effective indices are:

$$n_{eff(TE0)} = 1.72,$$
$$n_{eff(TM0)} = 1.45.$$

The effective index of TM mode is below the optical index of glass substrate. It can therefore leak in to the glass substrate so that it can be observed in the back focal plane in Fig. 4.23.c,d. Fig. 4.25 shows the Poynting vector distribution of TE and TM mode. On the left figure, energy of TE mode is confined in the waveguide. While energy of TM mode extends more in the glass substrate. When the planar waveguide is very thin (80 nm), the waveguide only support single TE mode. TE mode light is confined in the waveguide and propagate to the edge. TM mode light leaks into glass.

4.4.2 Directional emission coupled to planar waveguide

Following previous result, we reduce the number of quantum dots. The back focal plane and image plane images are shown in Fig. 4.26 and 4.27 for a few

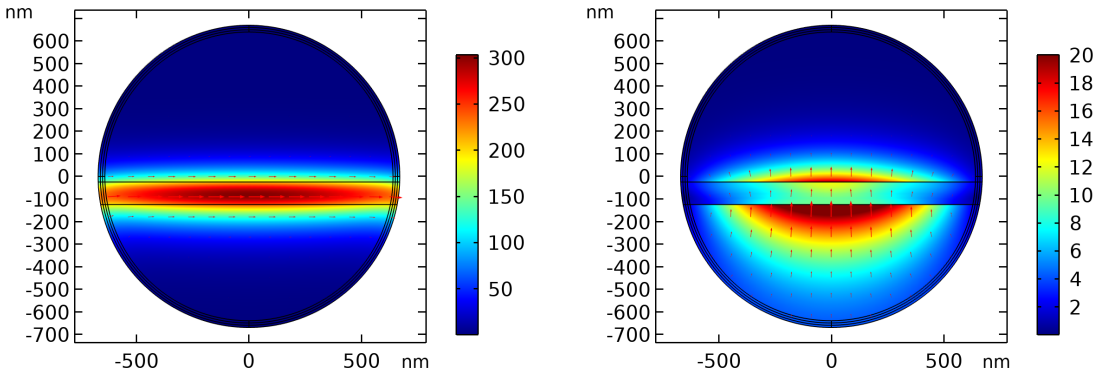

a) TE mode b) TM mode

Figure 4.25: 2D eigen mode analysis of TiO_2 waveguide on glass. Mode profile of a) TM_0 mode, b) TE_0 mode. Arrows refer to electric field. Color map represents the mode profile.

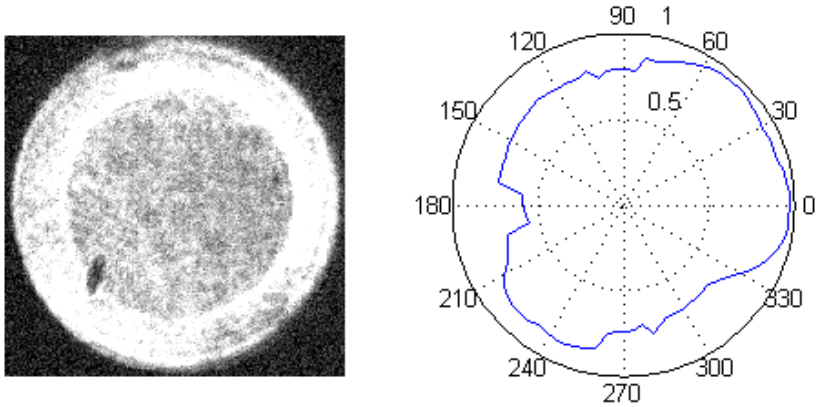

Figure 4.26: Back focal plane image of QD emission scattered by Yagi-Uda antenna into the substrate.

QD (≤ 5). The coupling efficiency can be estimated. We measure the scattered light around the ring and in the center. The coupling efficiency is estimated as $\eta = P_{ring}/(P_{ring}+P_{center}) = 39\%$. It is lower than the calculated $\eta(64\%)$, because of propagation losses into the TiO_2 waveguide and lower coupling efficiency depending on QD-feed distance. Numerical simulations considered a single dipole polarized along the rod axis so that it overestimate the coupling efficiency compared to experimental situation.

We observe directional scattering whose intensity on up (120°) and right (0°) side is more than those on the other two directions. In order to distinguish the

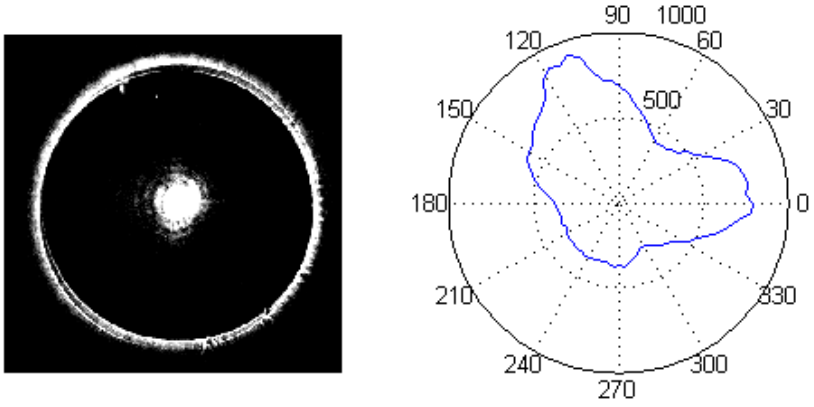

Figure 4.27: Image of scattering light of TiO_2 waveguide with Yagi-Uda antenna assisted QD emission. The inner spot is the light scattered by Yagi-Uda antenna. The outer ring is the light scattered from the edge of TiO_2 waveguide.

property on orthogonal directions, we put analyzers before camera and APDs. Along the orientation of Yagi-Uda antenna, we observe significant forward directivity with a front-to-back ratio F/B=1.5 (Fig. 4.28a).

Fig. 4.28.c,d presents the TM signal collected in the BFP that is attributed to the light emitted by uncoupled QDs. We attribute the small right/left directivity to reflection on the antenna.

However, in perpendicular direction, we also observe anisotropic distribution. In order to understand the result, we proposed two possible reasons: misalignment, off resonance. Misalignment means the position of deposited quantum dots are slightly shifted. Off resonance means the feed length is shorter or longer than its actual resonant length. We have realized numerical simulations for each assumption. The far field power of each polarization components are shown in Fig. 4.30. The misalignment case (Fig. 4.30a) has comparable far field components in the direction parallel (x) and perpendicular (y) to the nanorod. We can still observe the right/left antenna effect for x polarization. Moreover, the misalignment of QD induced also a dissymmetry perpendicularly to the nanorod for x polarized component, in fair agreement with our measured data. The off resonance case (Fig. 4.30b) does not reproduce the experiment. Therefore, the most possible reason is the misalignment of quantum dots. Since the accuracy of QD deposition is 50 nm, it is difficult to deposit QD exactly at the tip of the feed element under current experiment method. The lift-off process during the QD deposition can also shift the QD position. We expect better coupling with more precise deposition method.

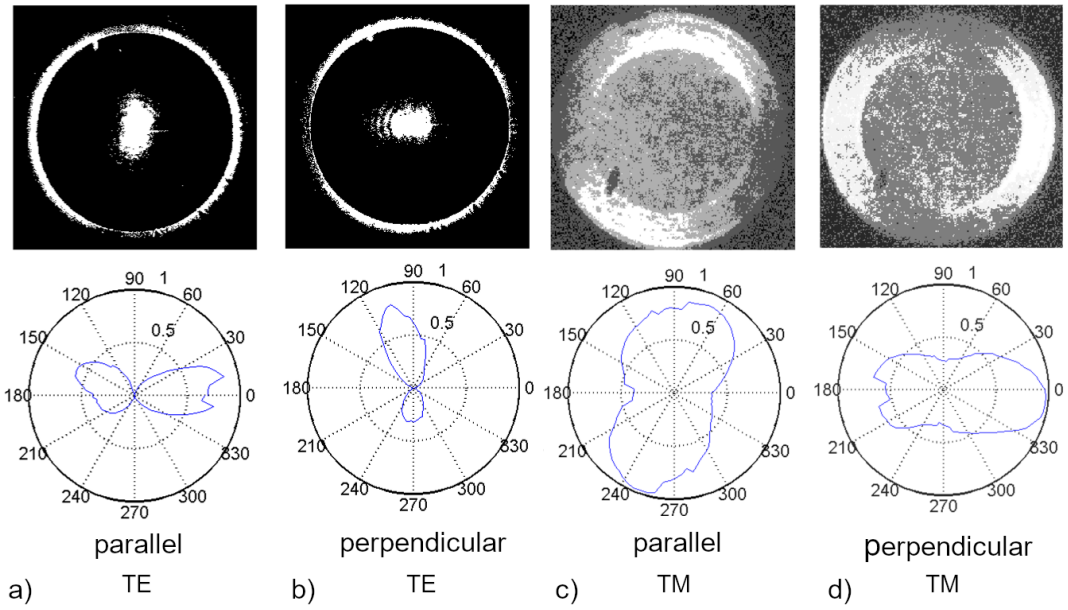

Figure 4.28: Antenna mediated QD emission in TiO_2 planar waveguide. a,b) Image plane for analyzer parallel (a) or perpendicular (b) to the rod axis. c,d) Back focal plane images for light scattered from the center. Bottom line: angular cross section of the light scattered at the microdisk edge.

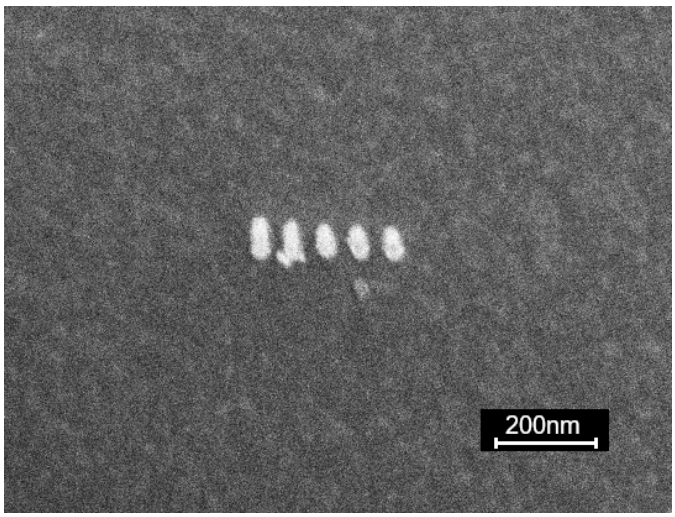

Figure 4.29: SEM image of Yagi-Uda antenna on TiO_2 microdisk.

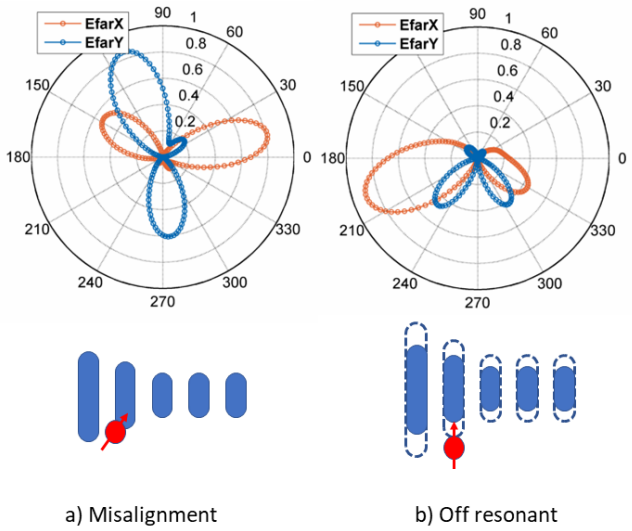

Figure 4.30: Simulated far field polar plots of possible coupling situations. a) misaligned coupling b) off resonant coupling.

4.4.3 Lifetime measurement

As we mentioned in Sec. 3.5.3, the lifetime of the emission can be used to characterize the enhancement of QD emission and the quality of the coupling. Besides, as is mentioned in [73], it is also interesting to observe the lifetime just at the photon source and at the edge of the planar waveguide. In order to keep the excitation in a consistent condition, the laser spot is kept in the same position and the pinhole and APD are adjusted to the position in the image plane accordingly.

The decay dynamics function is shown in Fig. 4.31. The data is fitted by the convolution between bi-exponential and the instrument response function (IRF). The fitting parameters are shown in Tab. 4.3.

Table 4.3: Lifetime fitting result of QDs close to Yagi-Uda antenna.

Fitting / Type	τ_X/ns	τ_{XX}/ns	A_X	A_{XX}
Center	8.1	1.36	19.5	47
Back edge	9.21	1.59	0.728	1.83

The lifetime at the edge of TiO_2 waveguide (after coupling to the guided mode) is overall longer than the lifetime in the center (for coupled and uncoupled QD). The differences is not significant but may be attributed to QD emission filtered by the guided mode (see [73]).

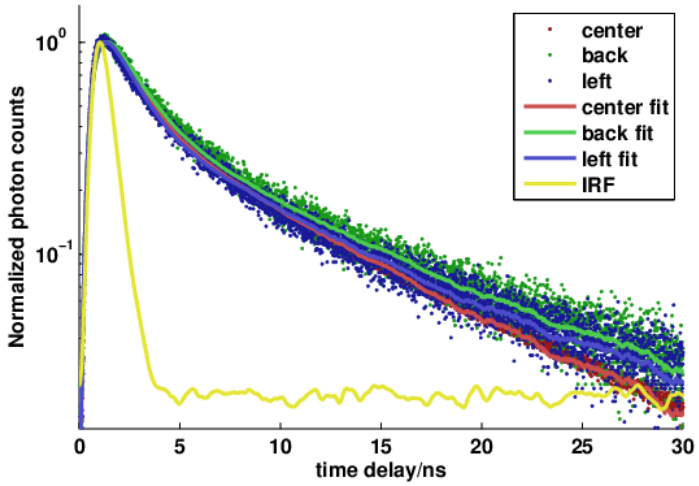

Figure 4.31: Lifetime measurement of scattered light at the center of photon source (red), at the back edge of TiO_2 waveguide (green) and on the left edge of TiO_2.

4.5 Conclusion

In this chapter, we tried to demonstrate the unidirectional coupling of quantum dot emission to TiO_2 waveguide. Each layers are fabricated separately and then combined. The QD - Yagi-Uda antenna coupling shows efficient unidirectional scattering. In the full integration experiment, we found the quantum dots fluorescence coupled to waveguide with 39% efficiency. The scattering pattern at the edge of waveguide show directional emission on two directions. The F/B power ratio of parallel polarized TE mode is 1.5. The misalignment of QD can explain the unexpected directional coupling in the perpendicular direction. More precise coupling requires the alignment error below 10 nm which needs to be improved in a future work.

Chapter 5

Conclusion and perspectives

The thesis work implements the QD-antenna coupling to TiO_2 waveguide step by step.

We theoretically analyzed the coupling between dipole and TiO_2 waveguide. We analyzed the guided mode profile to figured out the rough range of TiO_2 thickness. The mode analysis calculated the decay rate of dipole in different channels (TE, TM and their combination). 55% efficiency in TE mode without directivity is obtained in bare film.

As the first step, we prepared QD deposition technique and QD-antenna deposition on the glass substrate. The QD can be directly deposited in 100 nm hole. We achieved QD-antenna coupling system with F/B power ratio $F/B \sim 4$ and sixfold decay rate enhancement.

Finally we integrate QD, Yagi-Uda antenna and TiO_2 to demonstrate unidirectional coupling. The optical characterization shows antenna effect in the parallel polarization direction but we also observed directional scattering in perpendicular polarization direction. We proposed two probable reasons for the observation. Numerical simulation shows the most probable reason is the misalignment of QD. We need to further improve the QD deposition method ($\sim$ 10 nm) to achieve better directivity. We conclude that the unidirectional coupling is feasible but requires more precise QD deposition.

For our future work, we expect to introduce or implement new QD deposition method to improve the precision. Embedding the Yagi-Uda antenna into the waveguide would also improve the coupling efficiency to the guided mode but necessitate planarization of the slab that could be difficult to achieve. A precise Yagi-Uda antenna mediated QD emission coupling to TiO_2 can be an efficient unidirectional integrated photon source.

The well controlled source can be applied to integrated photonic circuits as an efficient local photon source. We can also improve the control of deposited QD numbers. The integrated single photon source can be used to implement functional

devices, such as CNOT gate[8], for quantum information.

From the long-term perspective, the efficient integrated single or indistinguishable photon source can be the core of the fully integrated quantum information device. The continuous improvement of integrated single or indistinguishable photon sources can finally promote the development of integrated quantum devices.

Bibliography

[1] Joshua W. Silverstone, Damien Bonneau, Jeremy L. O'Brien, and Mark G. Thompson. Silicon quantum photonics. *IEEE Journal of Selected Topics in Quantum Electronics*, 22(6):390–402, Nov 2016.

[2] Irene D'Amico, Dimitris G Angelakis, Félix Bussieres, Humeyra Caglayan, Christophe Couteau, Thomas Durt, Branko Kolaric, Patrick Maletinsky, Walter Pfeiffer, Peter Rabl, et al. Nanoscale quantum optics. *La Rivista del Nuovo Cimento*, 42(4):153–195, 2019.

[3] Ali W. Elshaari, Wolfram Pernice, Kartik Srinivasan, Oliver Benson, and Val Zwiller. Hybrid integrated quantum photonic circuits. *Nature Photonics*, 14(55):285–298, May 2020.

[4] Je-Hyung Kim, Shahriar Aghaeimeibodi, Jacques Carolan, Dirk Englund, and Edo Waks. Hybrid integration methods for on-chip quantum photonics. *Optica*, 7(4):291, Apr 2020.

[5] N. Somaschi, V. Giesz, L. De Santis, J. C. Loredo, M. P. Almeida, G. Hornecker, S. L. Portalupi, T. Grange, C. Antón, J. Demory, C. Gómez, I. Sagnes, N. D. Lanzillotti-Kimura, A. Lemaítre, A. Auffeves, A. G. White, L. Lanco, and P. Senellart. Near-optimal single-photon sources in the solid state. *Nature Photonics*, 10(5):340–345, May 2016.

[6] Bjoern Lekitsch, Sebastian Weidt, Austin G. Fowler, Klaus Mølmer, Simon J. Devitt, Christof Wunderlich, and Winfried K. Hensinger. Blueprint for a microwave trapped ion quantum computer. *Science Advances*, 3(2):e1601540, Feb 2017.

[7] Philip Sibson, Jake E. Kennard, Stasja Stanisic, Chris Erven, Jeremy L. O'Brien, and Mark G. Thompson. Integrated silicon photonics for high-speed quantum key distribution. *Optica*, 4(2):172–177, Feb 2017.

[8] Annemarie Holleczek, Oliver Barter, Allison Rubenok, Jerome Dilley, Peter B. R. Nisbet-Jones, Gunnar Langfahl-Klabes, Graham D. Marshall, Chris

Sparrow, Jeremy L. O'Brien, Konstantinos Poulios, Axel Kuhn, and Jonathan C. F. Matthews. Photonic quantum logic with narrowband light from single atoms. *Physical Review Letters*, 117(2):023602, Jul 2016. arXiv:1508.03266 [quant-ph].

[9] Charles Santori, David Fattal, Jelena Vučković, Glenn S. Solomon, and Yoshihisa Yamamoto. Indistinguishable photons from a single-photon device. *Nature*, 419(6907):594–597, Oct 2002.

[10] Kotni Santhosh, Ora Bitton, Lev Chuntonov, and Gilad Haran. Vacuum rabi splitting in a plasmonic cavity at the single quantum emitter limit. *Nature communications*, 7(1):1–5, 2016.

[11] Edward Mills Purcell. Spontaneous emission probabilities at radio frequencies. In *Confined Electrons and Photons*, pages 839–839. Springer, 1995.

[12] Thomas Grange, Gaston Hornecker, David Hunger, Jean-Philippe Poizat, Jean-Michel Gérard, Pascale Senellart, and Alexia Auffèves. Cavity-funneled generation of indistinguishable single photons from strongly dissipative quantum emitters. *Physical review letters*, 114(19):193601, 2015.

[13] G. Colas des Francs, J. Barthes, A. Bouhelier, J. C. Weeber, and A. Dereux. Plasmonic purcell factor and coupling efficiency to surface plasmons. implications for addressing and controlling optical nanosources. *Journal of Optics*, 18(9):094005, Sep 2016.

[14] Kerry J Vahala. Optical microcavities. *nature*, 424(6950):839–846, 2003.

[15] Mario Agio. Optical antennas as nanoscale resonators. *Nanoscale*, 4(3):692–706, 2012.

[16] Simeon I. Bogdanov, Mikhail Y. Shalaginov, Alexei S. Lagutchev, Chin-Cheng Chiang, Deesha Shah, Alexandr S. Baburin, Ilya A. Ryzhikov, Ilya A. Rodionov, Alexander V. Kildishev, Alexandra Boltasseva, and Vladimir M. Shalaev. Ultrabright room-temperature sub-nanosecond emission from single nitrogen-vacancy centers coupled to nanopatch antennas. *Nano Letters*, 18(8):4837–4844, Aug 2018.

[17] Cherif Belacel, Benjamin Habert, Florian Bigourdan, François Marquier, J-P Hugonin, S Michaelis de Vasconcellos, Xavier Lafosse, Laurent Coolen, Catherine Schwob, Clémentine Javaux, et al. Controlling spontaneous emission with plasmonic optical patch antennas. *Nano letters*, 13(4):1516–1521, 2013.

[18] M. Arcari, I. Söllner, A. Javadi, S. Lindskov Hansen, S. Mahmoodian, J. Liu, H. Thyrrestrup, E. H. Lee, J. D. Song, S. Stobbe, and P. Lodahl. Near-unity coupling efficiency of a quantum emitter to a photonic crystal waveguide. *Physical Review Letters*, 113(9):093603, Aug 2014.

[19] Hamidreza Siampour, Shailesh Kumar, and Sergey I. Bozhevolnyi. Nanofabrication of plasmonic circuits containing single photon sources. *ACS Photonics*, 4(8):1879–1884, Aug 2017.

[20] Thierry Grosjean, Mathieu Mivelle, Geoffrey W Burr, and Fadi Issam Baida. Optical horn antennas for efficiently transferring photons from a quantum emitter to a single-mode optical fiber. *Optics express*, 21(2):1762–1772, 2013.

[21] Mathieu Mivelle, Pierre Viktorovitch, Fadi I Baida, Ali El Eter, Zhihua Xie, Than-Phong Vo, Elie Atie, Geoffrey W Burr, Dusan Nedeljkovic, Jean-Yves Rauch, et al. Light funneling from a photonic crystal laser cavity to a nanoantenna: overcoming the diffraction limit in optical energy transfer down to the nanoscale. *Optics express*, 22(12):15075–15087, 2014.

[22] Heykel Aouani, Oussama Mahboub, Nicolas Bonod, Eloïse Devaux, Evgeny Popov, Hervé Rigneault, Thomas W. Ebbesen, and Jérôme Wenger. Bright unidirectional fluorescence emission of molecules in a nanoaperture with plasmonic corrugations. *Nano Letters*, 11(2):637–644, Feb 2011.

[23] Thi Phuong Lien Ung, Rabeb Jazi, Julien Laverdant, Remy Fulcrand, Gérard Colas des Francs, Jean-Pierre Hermier, Xavier Quélin, and Stéphanie Buil. Scanning the plasmonic properties of a nanohole array with a single nanocrystal near-field probe. *Nanophotonics*, 9(4):793–801, 2020.

[24] Alberto G. Curto, Giorgio Volpe, Tim H. Taminiau, Mark P. Kreuzer, Romain Quidant, and Niek F. van Hulst. Unidirectional emission of a quantum dot coupled to a nanoantenna. *Science*, 329(5994):930–933, Aug 2010.

[25] Manon Lamy, Kamal Hammani, Juan Arocas, Christophe Finot, and Jean-Claude Weeber. Broadband etching-free metal grating couplers embedded in titanium dioxide waveguides. *Optics Letters*, 42(14):2778–2781, Jul 2017.

[26] T. Lund-Hansen, S. Stobbe, B. Julsgaard, H. Thyrrestrup, T. Sünner, M. Kamp, A. Forchel, and P. Lodahl. Experimental realization of highly efficient broadband coupling of single quantum dots to a photonic crystal waveguide. *Physical Review Letters*, 101(11):113903, Sep 2008.

[27] Guillaume Blanquer, Vivien Loo, Nancy Rahbany, Christophe Couteau, Sylvain Blaize, Rafael Salas-Montiel, Yannick De Wilde, and Valentina Krachmalnicoff. Waveguide efficient directional coupling and decoupling via an integrated plasmonic nanoantenna. *Optics Express*, 29(18):29034–29043, 2021.

[28] Thi Huong Au, Stéphanie Buil, Xavier Quélin, Jean-Pierre Hermier, and Ngoc Diep Lai. High directional radiation of single photon emission in a dielectric antenna. *ACS photonics*, 6(11):3024–3031, 2019.

[29] Shailesh Kumar and Sergey I. Bozhevolnyi. Single photon emitters coupled to plasmonic waveguides: A review. *Advanced Quantum Technologies*, 4(10):2100057, Oct 2021.

[30] Jean-Claude Weeber, Kamal Hammani, Gerard Colas-des Francs, Alexandre Bouhelier, Juan Arocas, Arunandan Kumar, Fabien Eloi, Stephanie Buil, Xavier Quelin, Jean-Pierre Hermier, et al. Colloidal quantum dot integrated light sources for plasmon mediated photonic waveguide excitation. *ACS Photonics*, 3(5):844–852, 2016.

[31] Tim H Taminiau, Fernando D Stefani, and Niek F van Hulst. Enhanced directional excitation and emission of single emitters by a nano-optical yagiuda antenna. *Optics express*, 16(14):10858–10866, 2008.

[32] Felipe Bernal Arango, Andrej Kwadrin, and A. Femius Koenderink. Plasmonic antennas hybridized with dielectric waveguides. *ACS Nano*, 6(11):10156–10167, Nov 2012.

[33] A. Femius Koenderink. Plasmon nanoparticle array waveguides for single photon and single plasmon sources. *Nano Letters*, 9(12):4228–4233, Dec 2009.

[34] Lukas Novotny. Effective wavelength scaling for optical antennas. *Physical review letters*, 98(26):266802, 2007.

[35] Na Liu, Hongcang Guo, Liwei Fu, Stefan Kaiser, Heinz Schweizer, and Harald Giessen. Three-dimensional photonic metamaterials at optical frequencies. *Nature Materials*, 7(11):31–37, Jan 2008.

[36] Emilie Wientjes, Jan Renger, Alberto G. Curto, Richard Cogdell, and Niek F. van Hulst. Strong antenna-enhanced fluorescence of a single light-harvesting complex shows photon antibunching. *Nature Communications*, 5(1):4236, Sep 2014.

[37] Mohammad Ramezani, Alberto Casadei, Grzegorz Grzela, Federico Matteini, Gözde Tütüncüoglu, Daniel Rüffer, Anna Fontcuberta i Morral, and Jaime

Gómez Rivas. Hybrid semiconductor nanowire–metallic yagi-uda antennas. *Nano Letters*, 15(8):4889–4895, Aug 2015.

[38] Dietrich Marcuse. *Theory of dielectric optical waveguides*. Elsevier, 2013.

[39] H Kogelnik and V Ramaswamy. Scaling rules for thin-film optical waveguides. *Applied Optics*, 13(8):1857–1862, 1974.

[40] Gilbert Grynberg, Alain Aspect, and Claude Fabre. *Introduction to quantum optics: from the semi-classical approach to quantized light*. Cambridge university press, 2010.

[41] Lukas Novotny and Bert Hecht. *Principles of nano-optics*. Cambridge university press, 2012.

[42] Ludwig Knöll, S Scheel, and DG Welsch. Coherence and statistics of photons and atoms, 2001.

[43] Pedro De Vries, David V Van Coevorden, and Ad Lagendijk. Point scatterers for classical waves. *Reviews of modern physics*, 70(2):447, 1998.

[44] RR Chance, A Prock, and R Silbey. Comments on the classical theory of energy transfer. *The Journal of Chemical Physics*, 62(6):2245–2253, 1975.

[45] WL Barnes. Fluorescence near interfaces: the role of photonic mode density. *journal of modern optics*, 45(4):661–699, 1998.

[46] Yoshihiko Kuwahara. Multiobjective optimization design of yagi-uda antenna. *IEEE Transactions on Antennas and Propagation*, 53(6):1984–1992, 2005.

[47] Constantine A Balanis. *Antenna theory: analysis and design*. John wiley & sons, 2015.

[48] Nicolas Bonod, Alexis Devilez, Brice Rolly, Sebastien Bidault, and Brian Stout. Ultracompact and unidirectional metallic antennas. *Physical Review B*, 82(11):115429, 2010.

[49] Holger F Hofmann, Terukazu Kosako, and Yutaka Kadoya. Design parameters for a nano-optical yagi–uda antenna. *New journal of physics*, 9(7):217, 2007.

[50] Y Ould Agha, Olivier Demichel, Christian Girard, Alexandre Bouhelier, and G Colas des Francs. Near-field properties of plasmonic nanostructures with high aspect ratio. *arXiv preprint arXiv:1509.07103*, 2015.

[51] Peter B Johnson and R-WJPrB Christy. Optical constants of the noble metals. *Physical review B*, 6(12):4370, 1972.

[52] Lukas Novotny and Niek Van Hulst. Antennas for light. *Nature photonics*, 5(2):83–90, 2011.

[53] Jian-Ming Jin. *The finite element method in electromagnetics*. John Wiley & Sons, 2015.

[54] COMSOL Inc. Comsol multiphysics®. `https://www.comsol.com/`, date unknown. Accessed: 2021-10-20.

[55] Steven H Schot. Eighty years of sommerfeld's radiation condition. *Historia mathematica*, 19(4):385–401, 1992.

[56] Alberto G Curto, Tim H Taminiau, Giorgio Volpe, Mark P Kreuzer, Romain Quidant, and Niek F Van Hulst. Multipolar radiation of quantum emitters with nanowire optical antennas. *Nature communications*, 4(1):1–7, 2013.

[57] Dandan Ge, Sylvie Marguet, Ali Issa, Safi Jradi, Tien Hoa Nguyen, Mackrine Nahra, Jéremie Béal, Régis Deturche, Hongshi Chen, Sylvain Blaize, Jérôme Plain, Céline Fiorini, Ludovic Douillard, Olivier Soppera, Xuan Quyen Dinh, Cuong Dang, Xuyong Yang, Tao Xu, Bin Wei, Xiao Wei Sun, Christophe Couteau, and Renaud Bachelot. Hybrid plasmonic nano-emitters with controlled single quantum emitter positioning on the local excitation field. *Nature Communications*, 11(11):3414, Jul 2020.

[58] Yi Cui, Mikael T Björk, J Alexander Liddle, Carsten Sönnichsen, Benjamin Boussert, and A Paul Alivisatos. Integration of colloidal nanocrystals into lithographically patterned devices. *Nano letters*, 4(6):1093–1098, 2004.

[59] O Lecarme, T Pinedo Rivera, L Arbez, T Honegger, K Berton, and D Peyrade. Colloidal optical waveguides with integrated local light sources built by capillary force assembly. *Journal of Vacuum Science & Technology B, Nanotechnology and Microelectronics: Materials, Processing, Measurement, and Phenomena*, 28(6):C6O11–C6O15, 2010.

[60] Jean-Claude Weeber, Gérard Colas-des Francs, Alexandre Bouhelier, Aymeric Leray, Kirill Vasilev, Xiao Yu, Kamal Hammani, Juan-Miguel Arocas, Gregory Gadret, Laurent Markey, and Benoit Dubertret. Colloidal quantum dots decorated micro-ring resonators for efficient integrated waveguides excitation. *Nanophotonics*, 9(6):1411–1423, Jun 2020.

[61] J Michaelis, Ci Hettich, Jürgen Mlynek, and Vahid Sandoghdar. Optical microscopy using a single-molecule light source. *Nature*, 405(6784):325–328, 2000.

[62] Aurélien Cuche, Aurélien Drezet, Yannick Sonnefraud, Orestis Faklaris, François Treussart, Jean-François Roch, and Serge Huant. Near-field optical microscopy with a nanodiamond-based single-photon tip. *Optics express*, 17(22):19969–19980, 2009.

[63] A Dousse, L Lanco, J Suffczyński, E Semenova, A Miard, A Lemaître, I Sagnes, C Roblin, Jacqueline Bloch, and P Senellart. Controlled light-matter coupling for a single quantum dot embedded in a pillar microcavity using far-field optical lithography. *Physical review letters*, 101(26):267404, 2008.

[64] M Humbert, Y Hallez, V Larrey, F Fournel, E Palleau, V Paillard, A Cuche, and L Ressier. Versatile, rapid and robust nano-positioning of single-photon emitters by AFM-nanoxerography. *Nanotechnology*, 33(21):215301, feb 2022.

[65] Sviatlana Viarbitskaya, Olivier Demichel, Benoit Cluzel, Gérard Colas des Francs, and Alexandre Bouhelier. Delocalization of nonlinear optical responses in plasmonic nanoantennas. *Physical Review Letters*, 115(19):197401, 2015.

[66] Amit R Dhawan, Michel Nasilowski, Zhiming Wang, Benoît Dubertret, and Agnès Maître. Fabrication of efficient single-emitter plasmonic patch antennas by deterministic in situ optical lithography using spatially modulated light. *Advanced Materials*, 34(11):2108120, 2022.

[67] Alexander L. Efros and David J. Nesbitt. Origin and control of blinking in quantum dots. *Nature Nanotechnology*, 11(8):661–671, Aug 2016.

[68] Praket P. Jha and Philippe Guyot-Sionnest. Trion decay in colloidal quantum dots. *ACS Nano*, 3(4):1011–1015, Apr 2009.

[69] H. Y. Ramirez, C. H. Lin, C. C. Chao, Y. Hsu, W. T. You, S. Y. Huang, Y. T. Chen, H. C. Tseng, W. H. Chang, S. D. Lin, and S. J. Cheng. Optical fine structures of highly quantized ingaas/gaas self-assembled quantum dots. *Physical Review B*, 81(24):245324, Jun 2010.

[70] Kenneth D. Weston, Martina Dyck, Philip Tinnefeld, Christian Müller, Dirk P. Herten, and Markus Sauer. Measuring the number of independent emitters in single-molecule fluorescence images and trajectories using coincident photons. *Analytical Chemistry*, 74(20):5342–5349, Oct 2002.

[71] Tian Ming, Lei Zhao, Huanjun Chen, Kat Choi Woo, Jianfang Wang, and Hai-Qing Lin. Experimental evidence of plasmophores: Plasmon-directed polarized emission from gold nanorod–fluorophore hybrid nanostructures. *Nano Letters*, 11(6):2296–2303, Jun 2011.

[72] Kamal Hammani, Laurent Markey, Manon Lamy, Bertrand Kibler, Juan Arocas, Julien Fatome, Alain Dereux, Jean-Claude Weeber, and Christophe Finot. Octave spanning supercontinuum in titanium dioxide waveguides. *Applied Sciences*, 8(4):543, 2018.

[73] Mélodie Humbert, Peter R. Wiecha, Gérard Colas des Francs, Xiao Yu, Nicolas Mallet, Aurélie Lecestre, Guilhem Larrieu, Vincent Larrey, Frank Fournel, Laurence Ressier, Christian Girard, Vincent Paillard, and Aurélien Cuche. Tailoring wavelength- and emitter-orientation-dependent propagation of single photons in silicon nanowires. *Physical Review Applied*, 17(1):014008, Jan 2022.